OCS Study
BOEMRE 2010-044

Full-Water Column Current Observations in the Western Gulf of Mexico

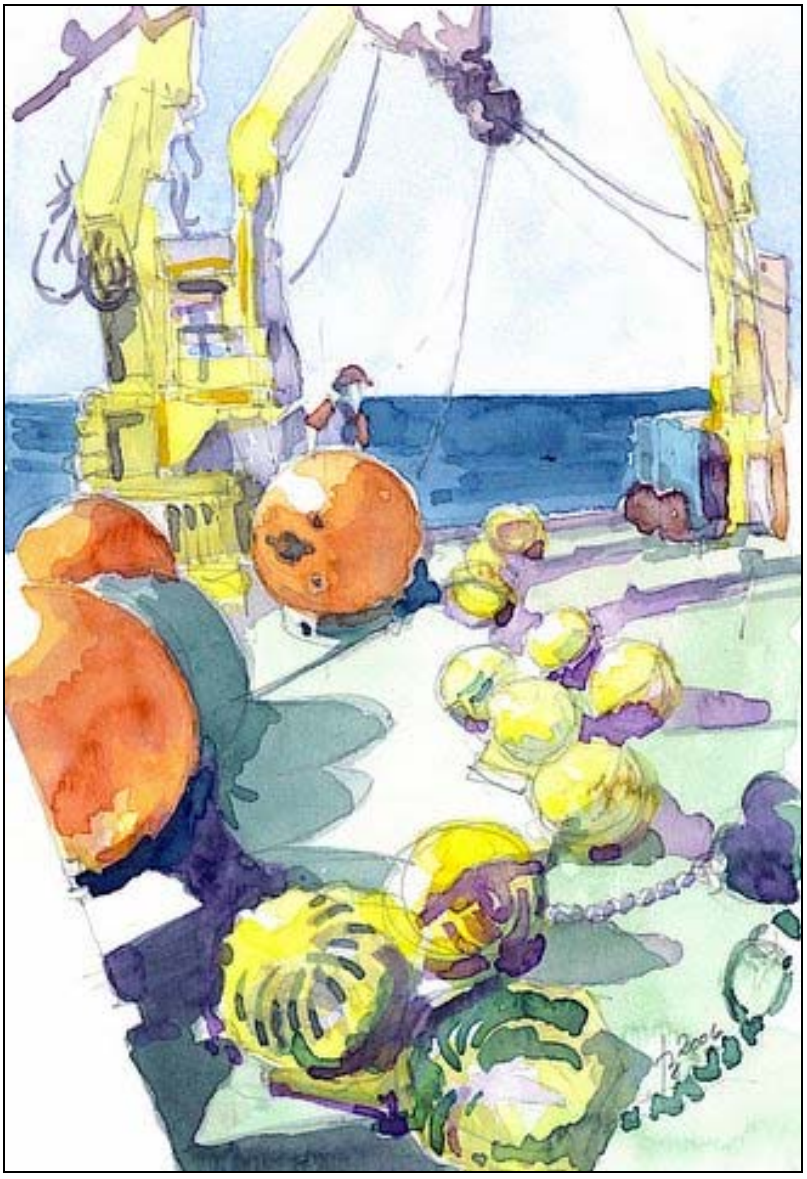

U.S. Department of the Interior
Bureau of Ocean Energy Management, Regulation and Enforcement
Gulf of Mexico OCS Region

OCS Study
BOEMRE 2010-044

Full-Water Column Current Observations in the Western Gulf of Mexico

Authors

J. Sheinbaum
J. Ochoa
J. Candela
A. Badan

Prepared under BOEMRE Contract
M04PC00019 (1435-01-04-CT-32916)
by
Centro de Investigación Científica
y Educación Superior de Ensenada
Ensenada, Mexico

Published by

U.S. Department of the Interior
Bureau of Ocean Energy Management,
Regulation and Enforcement
Gulf of Mexico OCS Region

New Orleans
December 2010

DISCLAIMER

This report was prepared under contract between the Bureau of Ocean Energy Management, Regulation and Enforcement (BOEMRE) and the Centro de Investigación Científica y de Educación Superior de Ensenada (CICESE). This report has been technically reviewed by the BOEMRE, and it has been approved for publication. Approval does not signify that the contents necessarily reflect the views and policies of the BOEMRE, nor does mention of trade names or commercial products constitute endorsement or recommendation for use. It is, however, exempt from review and compliance with the BOEMRE editorial standards.

REPORT AVAILABILITY

This report is available only in compact disc format from the Bureau of Ocean Energy Management, Regulation, and Enforcement, Gulf of Mexico OCS Region, at a charge of $15.00, by referencing OCS Study BOEMRE 2010-044. The report may be downloaded from the BOEMRE website through the Environmental Studies Program Information System (ESPIS). You will be able to obtain this report also from the National Technical Information Service in the near future. Here are the addresses. You may also inspect copies at selected Federal Depository Libraries.

U.S. Department of the Interior
Bureau of Ocean Energy Management,
Regulation and Enforcement
Gulf of Mexico OCS Region
Public Information Office (MS 5034)
1201 Elmwood Park Boulevard
New Orleans, Louisiana 70123-2394
Telephone requests may be placed at
(504) 736-2519, 1-800-200-GULF, or
Rush Orders: 1-800-553-6847
Fax: (504) 736-2620

U.S. Department of Commerce
National Technical Information Service
5285 Port Royal Road
Springfield, Virginia 22161
Phone: (703) 605-6040
Fax: (703) 605-6900
Email: bookstore@ntis.gov

CITATION

Sheinbaum J., J. Ochoa, J. Candela, and A. Badan. 2010. Full-water column current observations in the western Gulf of Mexico: Final report. U.S. Dept. of the Interior, Bureau of Ocean Energy Management, Regulation, and Enforcement, Gulf of Mexico OCS Region, New Orleans, LA. OCS Study BOEMRE 2010-044.

ABOUT THE COVER

Mooring on the deck of UNAM's R/V *Justo Sierra*. Watercolor by A. Badan. Used by permission.

ACKNOWLEDGMENT

Thanks are due to Drs. Alexis Lugo-Fernandez, BOEMRE; H. Maske, CICESE; and all the people at SAIC, for their generous support throughout the development of the study. We would also like to thank Captain Leobardo Ríos and the crew of R/V *Justo Sierra* for their enthusiastic support at sea. This work would not have been possible without the ample participation of CICESE's technical staff and students, in particular J.I. González, A. Ledo, M. Ojeda, B. Pérez, J. García, C. Flores, and T. Agüero.

J. Sheinbaum
J. Ochoa
J. Candela
A. Badan

TABLE OF CONTENTS

Page

LIST OF FIGURES

LIST OF TABLES

ABBREVIATIONS AND ACRONYMS

ADCP	Acoustic Doppler Current Profiler
AVISO	Archiving, Validation and Interpretation of Satellite Oceanographic data
BOEM	Bureau of Ocean Energy Management, Regulation, and Enforcement
CE	Cyclonic Eddy
CEOF	Complex EOF
CERSAT	Centre ERS d'Archivage et de Traitement
CICESE	Centro de Investigación Científica y de Educación Superior de Ensenada
CNES	Centre National d'Etudes Spatiales, France
CPD	Cycles per Day
CTD	(or C/T/D) Conductivity/Temperature/Depth
DOF	Degrees of Freedom
EEZ	Exclusive Economic Zone
EKE	Eddy Kinetic Energy
EOF	Empirical Orthogonal Function
ERS-2	Earth Resources Satellite - 2
GDR	Geophysical Data Record
GEOSAT	Geodetic Satellite
GFO	Geosat Follow-On
GMT	Greenwich Mean Time or UTC
GoM	Gulf of Mexico
KE	Kinetic Energy
LC	Loop Current
LCE	Loop Current Eddy
NDBC	National Data Buoy Center
NOAA	National Oceanic and Atmospheric Administration
PI	Principal Investigator
PIES	Inverted Echo Sounder with Pressure
RMS	Route Mean Square
SAIC	Science Applications International Corporation
SNR	Signal-to-Noise Ratio
SSH	Sea Surface Height
SSHA	Sea Surface Height Anomaly
SST	Sea Surface Temperature
SUW	Subtropical Underwater
T	Temperature

ABSTRACT

Fourteen months of direct surface to bottom current measurements off the coast of Tamaulipas, Mexico, in the NW Gulf of Mexico during 2004 and 2005 capture the evolution of currents as several oncoming warm Loop Current eddies and cyclonic eddies reach the mooring array. Results show that current variability is mostly associated with these eddies as well as strong wind events (e.g. Hurricane Emily and Northern winds). In all five moorings, current standard deviations are larger than the mean. Interestingly, the most intense surface currents are found on the southernmost mooring (MMS5) at 2000 m depth and not at the shelf break. In general, current fluctuations are typically 20-40 cm/s at the surface and decrease with depth. In the upper layers, energy increases offshore, with a clear influence from eddies, to a depth of about 800 m. Further at depth, a weaker but steady southward flow appears to be locked near the slope in the form of a persistent current over the 2000 m isobath. Although low frequency fluctuations (periods > 3 days) are, as could be expected, more energetic than high frequency fluctuations, near-inertial and supra-inertial fluctuations are ubiquitous in all moorings and at all depths. In fact, it is found that at depths close to 1200 m there is a relative maxima in the high frequency contribution to total fluctuating energy. Whether this feature is produced by eddies focusing wind generated near surface inertial oscillations or it is produced by some sort of wave activity related to eddy instabilities or eddy-topography interactions processes is still to be resolved.

In contrast to other studies, observations do not show a clear and coherent intensification of current variability near the bottom suggestive of topographic Rossby waves. We do find however coherent fluctuations at about 800-1200 m of periods near 20 days along the moorings located on the 2000 m isobath which may be related to baroclinic Kelvin waves.

These observations were complemented with satellite altimetry. Two warm eddies released from the Loop Current (Titanic and Ulysses) entered the study area during the period of observations. A third one, Vortex, approached the region just prior to the retrieval of the instruments. The centroid of the eddies always remained in waters deeper than 2000 m, dissipating finally in a region between 21.25ºN – 25.25ºN latitude and 94ºW – 97ºW longitude, off the coast of Tamaulipas, Mexico. Besides these warm eddies, intense current events associated with cyclonic eddies in the area are captured by the array. High and low sea level values are clearly correlated with warm and cold temperature anomalies as deep as 1200-1500 m.

A separate issue, given the measurement of the vertical motion of zooplankton by ADCPs, is the determination of the mean diel cycle, from near the surface up to 1200 m deep. The deep cycle is, as the well known behavior from 500 m up to the surface, phase locked with the sunlight cycle. The downward peak velocity occurs earlier closer to the surface; at 220 m it reaches a maximum of 150 m/h half an hour before sunrise, while at 900 m it peaks at only 30 m/h one hour and a half after sunrise. The cycle is nearly symmetric to solar noon, with upward peak velocities happening earlier at depth, a pattern expected if the vertical migration was triggered by critical light level that reached the greater depth closer to noon. Consequently with such differences in timing, in the mean, at greater depth the nightly shallower stay is longer for the deeper migrating biota. The peak vertical migration velocities showed relative maxima at 250 and 1100 m depth, a sign of increased biological activity.

1. INTRODUCTION

The Loop Current in the Gulf of Mexico extends periodically from the Yucatan Channel to the coast of Louisiana and, as it begins to retract, it usually pinches off and spins off a large anticyclonic eddy. The release of warm blobs is many times followed by a reattachment. The causes for the ultimate eddy release remains unclear. The release of eddies is at irregular intervals from six to 11 months (Sturges and Leben, 2000; Leben, 2005), and the eddies then drift in a general southwestern direction under the influence of the rotational beta effect, carrying with them some of the warmer, saltier, but less dense, Caribbean water into the western Gulf of Mexico. This translation takes from months to a year, during which the eddies shed and entrain some mass, but remain somehow identifiable, until they meet the shelf break off the Texas-Mexico coast, in the general vicinity of which they dissipate. The identification of one eddy is fuzzy; the breakup and merge of eddies is the rule. Any map of surface eddy kinetic energy shows clearly that eddies are of enormous importance in driving the circulation of the northwestern Gulf of Mexico.

Additional factors that affect the circulation in the western Gulf are the seasonally varying winds that drive a southerly coastal current during Fall and Winter, but becomes a northerly flow during the summer as the winds blow from the south (Morey *et al.*, 2005). In addition, there are semi-permanent current patterns of cyclonic circulation over the Texas and Louisiana shelves, and over the Campeche Bank (DiMarco *et al.*, 2005).

Equally important to the eddy release mechanism, and as poorly known, are the processes that accompany the dissipation of these eddies as they approach and interact with the shelf and slope off Texas and Mexico. It was widely believed that the eddies should dissipate in the 'eddy graveyard', the northwestern corner shelf of the Gulf of Mexico, in a series of interactions of the eddies with the shelf and slope topography, in the process shedding mass and redistributing vorticity, driving coastal jets and other forms of coastal motions in the process. The desire to better understand this evidently fundamental aspect of the gulf's circulation is the main reason for the measurements in this project. The project consisted of a large number of current meter moorings deployed for over one year over the Texas shelf and slope and, through our component of the experiment, extending southwards into Mexican waters. As it turns out, the three eddies existing during the experiment entered and dissipated within our observation area in Mexican waters and therefore, were best recorded by the moorings here analyzed and reported.

The data recovered document a wide spectrum of motions. The present report describes the subinertial currents recorded in the upper layers of the region of interest, which are related mostly to the presence of eddies, interacting among them and with the topography and decaying. Additionally, the transient intensification of inertial motions is also analyzed and described. There are several other motions of interest, such as isolated high-speed near-surface jets, which are not part of the analysis. All these forms of motion are of keen interest to the intense efforts by the oil industry in the region, as they impact directly the positioning and other operations of the platforms.

A section of this report is devoted to the analysis of the vertical velocity and echo signal measured by ADCPs in relation to zooplankton vertical daily migrations.

1.1. BACKGROUND

Eddies are a conspicuous feature of the circulation in many regions of the world, and have therefore motivated numerous observational and theoretical studies, especially in the Gulf of

Mexico, where the life cycle of eddies is complicated by their interaction and dissipation near the coast.

Elliott (1982) initially suggested from hydrographic studies that the eddies released from the Loop Current are an integral part of the gulf's circulation. The eddies detached from the Loop Current (LCE) are warm, anticyclonic, surface intensified eddies, shaped with a positive bulge in the sea surface elevation, and a depression of the thermocline beneath, and carry the Caribbean water trapped in them along their path to the western gulf, where they stir and mix their last fractions with the gulf's waters. LCEs diameters range from 100 to 400 km, with typical ones close to 200 km (Elliott, 1982), with their influence often reaching 800 m depth (Vukovich and Crissman, 1986), with tangential velocities from 50-70 cm/s at a distance of 50 to 80 km from the center of the eddy (Lewis *et al.*, 1989). After detaching from the Loop Current, they travel to the west-southwest of the gulf (Ichiye, 1962; Elliott, 1982, Vukovich, 2007) with speeds of O(5 km/day). The westward propagation of LCEs is in agreement with the influence of the beta effect (Cushman-Roisin *et al.*, 1990), but they also interact with a variety of surrounding eddies, either cyclones or anticyclones. In one case, Vukovich and Crissman (1986) observed that at 150 days from release, the LCE maintained 45 percent of its original diameter, and at 300 days, it was down to 30 percent of the original size. Some authors (Vukovich and Crissman, 1986, Vukovich, 2007) have described how LCEs, as they travel, exchange mass and other properties with their surroundings, and argue that they typically reach western continental margin of the gulf having about 30-50 percent of their original size, where they rapidly dissipate. The descriptions in this analysis show more complex processes because of the persistent merge and breakup of either cyclonic or anticyclonic eddies. Vukovich and Waddell (1991) followed the evolution of two eddies from the time they detached from the Loop Current to the time when they intersected the coast of the western gulf, showing that when the eddies reach the coast, they become elliptical, a much smaller, O(100 km) cyclonic structure develops next to the large eddy, and that as the eddy moves onto the slope, a jet of warmer water is driven between the eddy and the coast.

The dissipation processes are fundamental, because they are accompanied with a redistribution of momentum, vorticity, and other properties. From a practical aspect, the traveling eddies can cause several disruptions to the operations of oil and gas industry.

Theoretical studies include that of Zavala-Sanson *et al*. (1998) who examine, in a reduced gravity model, the collision of an anticyclonic eddy of non-zero potential vorticity with a meridional wall. They show that, under such model, the eddy slightly deforms when reaching the wall but most importantly expels mass in a southward jet adjacent to the boundary, which causes the eddy to move north, as a 'rocket effects'. In this model the eddy's translation that causes the approach and collision against the western boundary is purely a planetary beta effect. Even in a model in the f-plane (*i.e.* without the planetary beta effect), Nof (1999) reached similar conclusions with an eddy of vanishing potential vorticity. Nof's (1999) model suddenly imposes a vertical wall, cutting a western sector of a uniform, steady rotating eddy. This condition implied the generation of the southward jet adjacent to the wall, and the corresponding northward motion of the remaining rotating blob. In both models the southward jet has a Kelvin-like balance; an edge of water bulging against the wall, and flowing in geostrophic balance. The study of Csanady (1979) in a two-layer model argues that the decay time-scale of a warm eddy depends more on the lateral friction between the rotating water within the eddy and the surrounding waters, rather than from the loss of mass. In Zavala-Sanson *et al*., (1998) model, analytical approximations allow estimating the meridional motion of the eddy. This depends on the parameter $r = \varepsilon / \beta$, where $\beta = \beta_O R / f_O$, $\varepsilon = \omega / f_O$, R is the radius of the eddy, ω its

angular frequency, f_O and β_O are the Coriolis parameter and its latitudinal gradient. If $r > 1$, the motion of the eddy is to the south, consistent with the analytical solution, which balances the motion of the eddy with the force from the wall (*i.e.* a Kelvin-like balance with the eddy itself). If $r < 1$, the eddy travels to the north until it looses enough mass then reverses to the south, since the motion of the eddy depends on the mass distribution along the wall. The amount of numerical models dealing specifically with the Loop Current Eddies, starting with the study by Hurlburt and Thompson (1980), is large, here we mention some that are relevant to the collision against topography. Itoh and Sugimoto (2001) used a primitive equation model in sigma coordinates to study the effect of a warm eddy approaching a western boundary. They found that for a situation similar to that of the western Gulf of Mexico, the eddy initially should move to the southwest for a few days, and then to the north. Even though the slope is small, it causes a similar effect as in models with a vertical wall. Hyun and Hogan (2008) make an analysis of historical altimetry data and the use of the Hybrid Coordinate Ocean Model (HYCOM) to asses the evolution of LCE reiterating the importance of the cyclone formation south of the collision location and the jet-like current along the shelf. Their numerical examples cover the three predominant paths described by Vukovich and Crissman (1986) and other trajectories that have not been documented; entering Campeche Bay. Hyun and Hogan's (2008) model includes realistic topography but sets a single LCE per run as initial condition, without the surrounding plethora of common structures in the gulf. The three predominant trajectories are either along the northern slope, a southerly trajectory, or an intermediate path through the center of the gulf, which is direct to the area of the measurements here reported. Hyun and Hogan (2008) estimates show the varying reflection strength depending on the collision angle with the bottom gradient; maximum when normal to a steep slope. The LCE reflects, moving eastward after the first collision, then reacquires westward motion colliding again, a process observed in this set of measurements and described by others like Vidal *et al* (1994) and Vukovich (2007) . The cyclones produced during the collision process play an essential role in the reflection and subsequent return to westward motion of the LCEs (Zavala-Sanson *et al*, 1998, Hyun and Hogan, 2008). It seems then that the LCE 'bouncing' trajectory is largely dependent on the surrounding eddy field at the collision time, but the ultimate dissipation is against the western boundary.

2. SETTING AND DATA CHARACTERISTICS

A set of 5 moorings were deployed in the western Gulf of Mexico (Figure 1) to complement measurements being done over the Texas and Louisiana shelf and slope. The deployment lasted for over 14 months from August 2004 to November 2005. The 5 moorings were designed to adequately sample the distribution of currents from the surface to the bottom at each of their locations which were around 500 m for mooring MMS1, 2000 m for moorings MMS2, MMS4 and MMS5 and 3500 m for mooring MMS3. The northwest corner of the Gulf of Mexico consists of a 100 km-wide shelf that extends off the Texas coast to about 27°N and then stretches southwards, narrowing progressively along the Mexican coast, so that the shore is oriented north-south, but the edge of the shelf and slope are oriented north-north-east. The slope is about 100 km wide, with irregular topography joining the slope to the abyss at 3500 m depth (see Figure 2). Moorings 1, 2 and 3 sample this section, whereas moorings 4 and 5 (together with mooring 2) sample the along slope flow (Figure 1). Diagrams of the 5 moorings are shown in Figure 3. The instruments were located on the moorings in a way to efficiently monitor the currents throughout the water column, with a 75 kHz Long Ranger Acoustic Doppler Current Profiler (ADCP) from RDTeledyne looking up from 450 m depth to record currents in 8 m bins from the surface layer, a second Long Ranger at 1200 m depth recording in the same fashion from there to about 800 m depth, and a third, 300 kHz ADCP recording currents from 10 m off the bottom up into the bottom boundary layer (BBL) in 4 m bins. Intermediate depths not sampled by the ADCP's were monitored with Aanderaa RCM11 current meters at intervals of 500 m, as shown in Fig. 3. In this way, mooring MMS1, being in 500 m of water, consisted of a single 75 kHz Long Ranger, moorings MMS2, MMS4, and MMS5, in 2000 m of water, included the three ADCP's as described, plus Aanderaas at 750 and 1500 m. mooring MMS3, in 3500 m of water, included the three ADCP's, plus Aanderaas at 750, 1500, 2000, 2500, and 3000 m. Most of the instruments worked as expected except for some mishaps. There was an unexpected pre-release of mooring MMS1, 24 hours after deployment, due to a mistakenly factory programmed release that was set to release 24 hours after being deployed. The factory Benthos Inc. did not informed about the state of the instrument upon delivery and without this information the release was used as expected. Therefore, the mooring was set adrift and, on top, the Argos beacon malfunctioned so no warning was obtained about the situation. Fortunately the mooring was rescued by a shrimp fisherman and taken to the Port of Brownsville. This mooring was then redeployed in December 2004, with the aid of the same shrimp fisherman that had rescued it, and lasted until the middle of October 2005 when the batteries on the LR ADCP were exhausted. The two other important failures were two LR ADCP instruments, one on the top (~500 m) of mooring MMS3 and the other deployed at a depth of 1260 m on mooring MMS4 (Figure 3). Both of these instruments, also factory delivered before deployment, had problems related to faulty seals around the transducer heads that lead to partial water leakages into the instruments' electronics shortly after deployment, with the consequence of complete data lose. Three other minor mishaps consisted in battery failure before recovery on the Aanderaa current-meters deployed at 820 and 2556 m on mooring MMS3 and 763 m on mooring MMS5. These resulted in measurement time series less than 14 months at these locations (Figure 4).

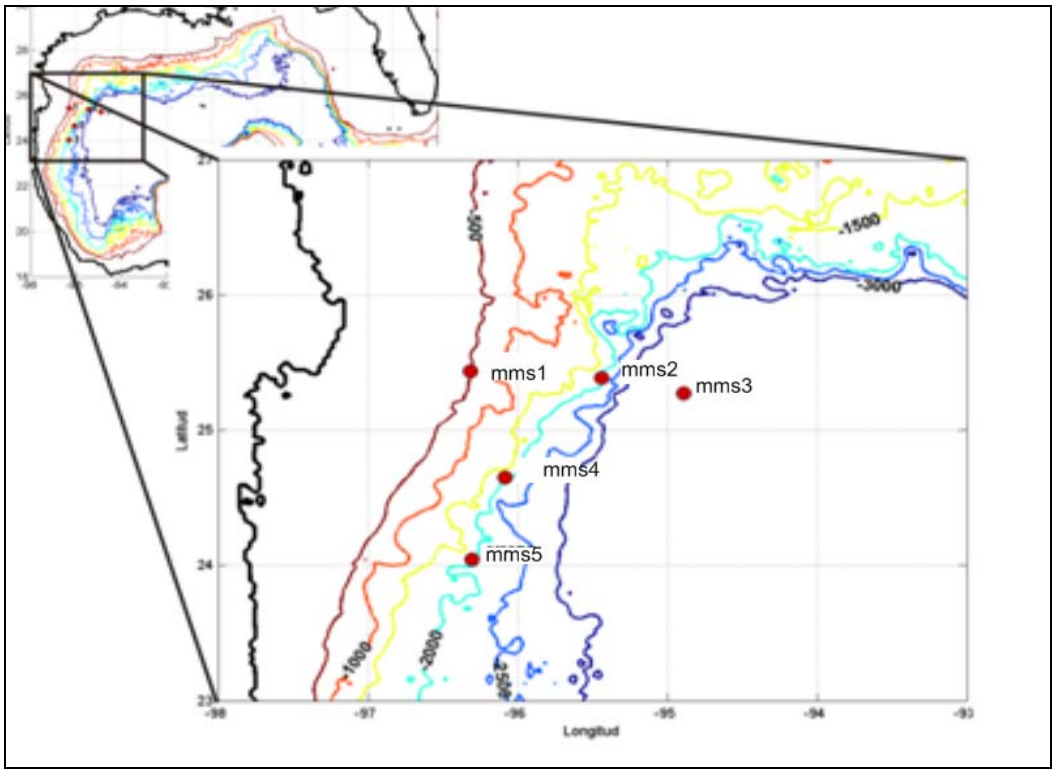

Figure 1. Location of the WG moorings on the slope off the Mexican coast of the NW Gulf of Mexico. Depth contours in meters.

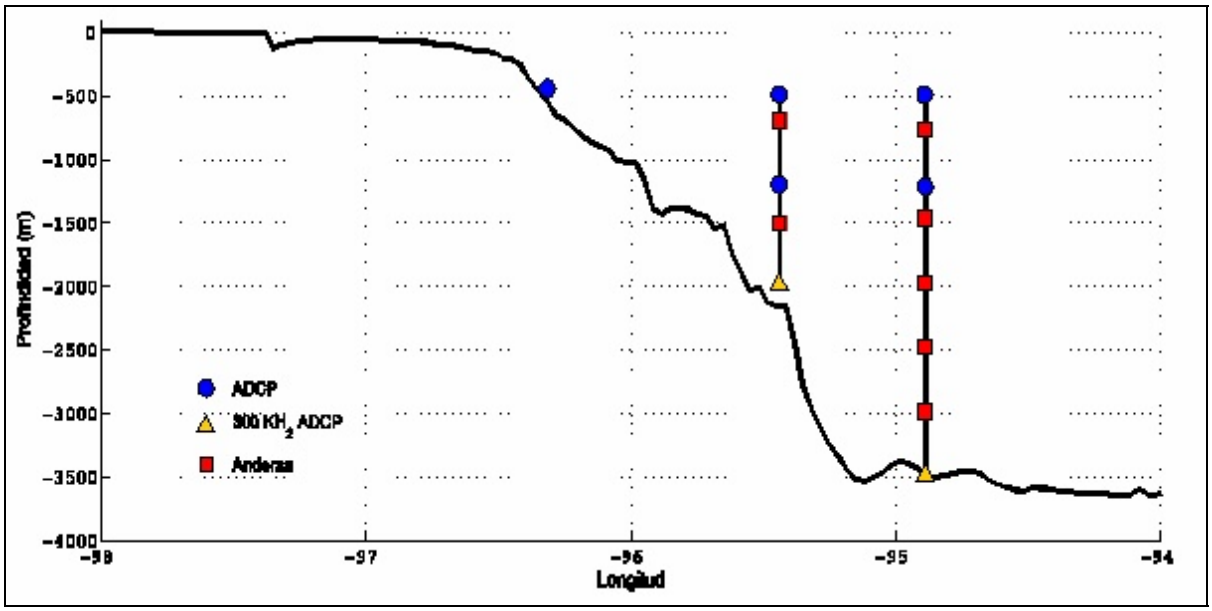

Figure 2. Longitude-depth section showing Moorings 1, 2, and 3.

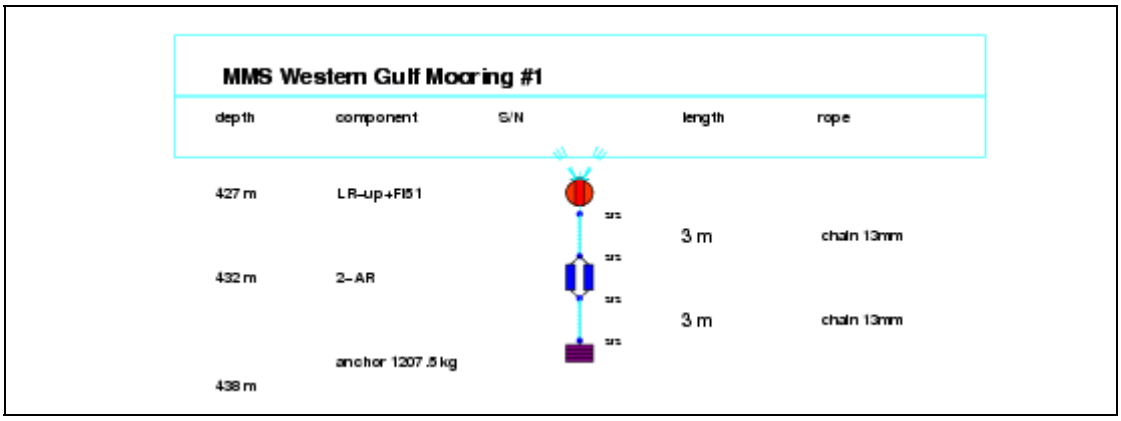

Figure 3. Vertical distribution of instruments on the five moorings.

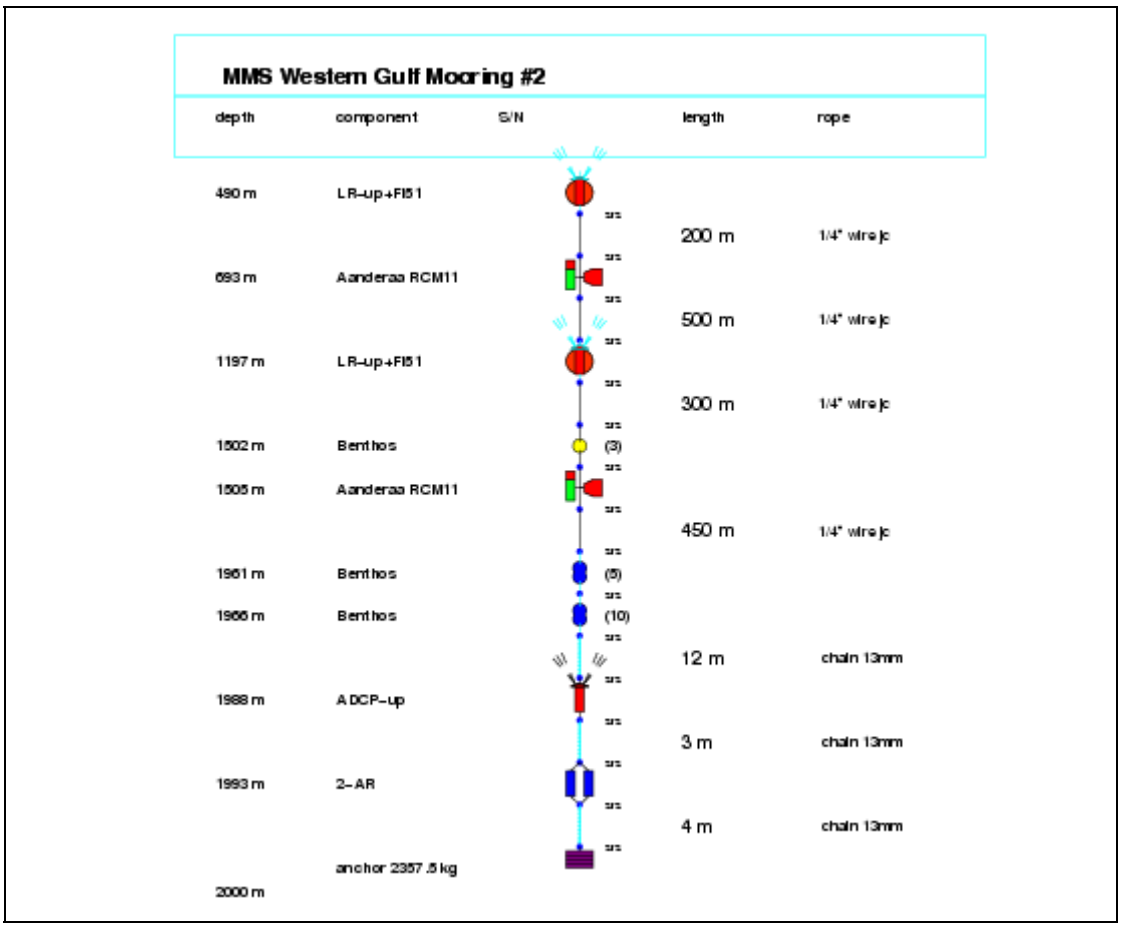

Figure 3. Vertical distribution of instruments on the five moorings (continued).

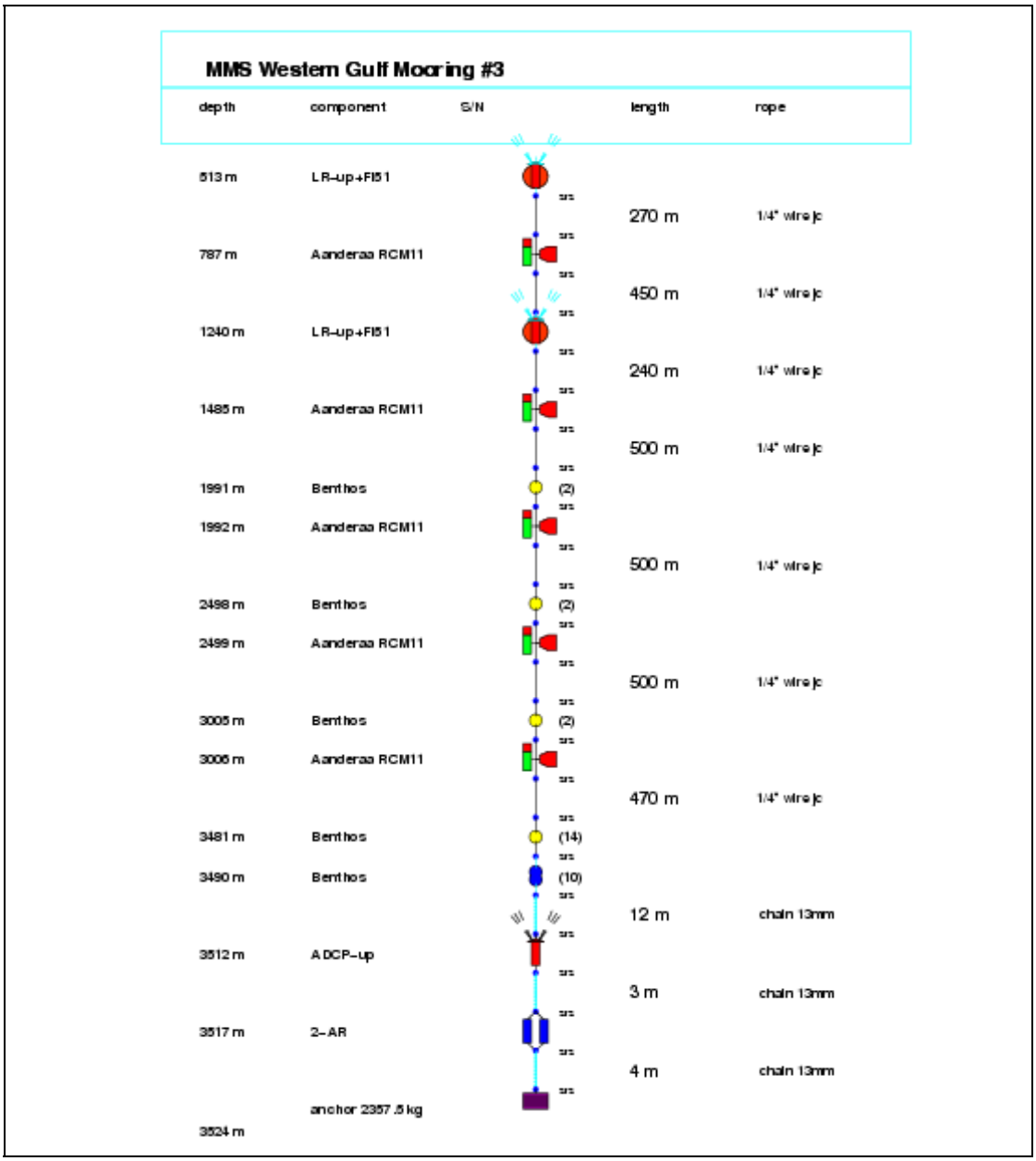

Figure 3. Vertical distribution of instruments on the five moorings (continued).

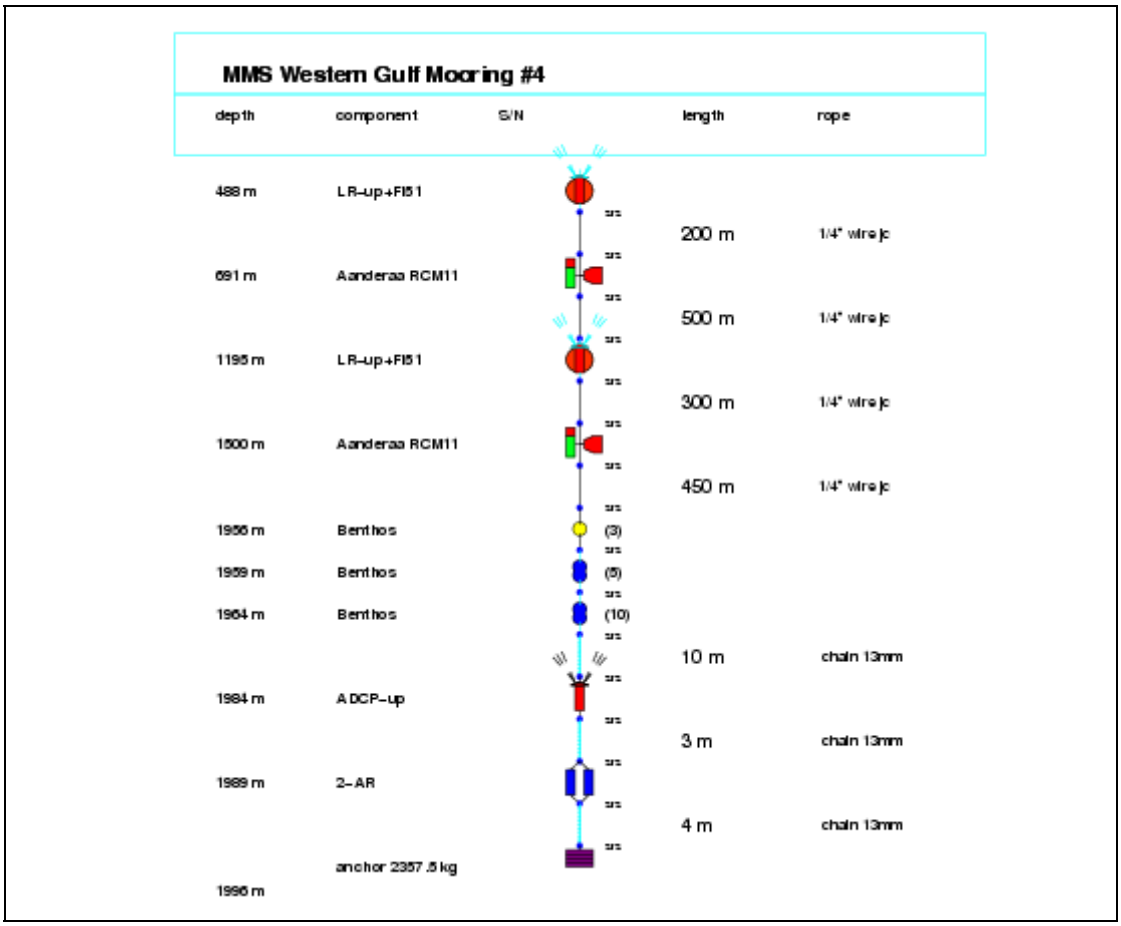

Figure 3. Vertical distribution of instruments on the five moorings (continued).

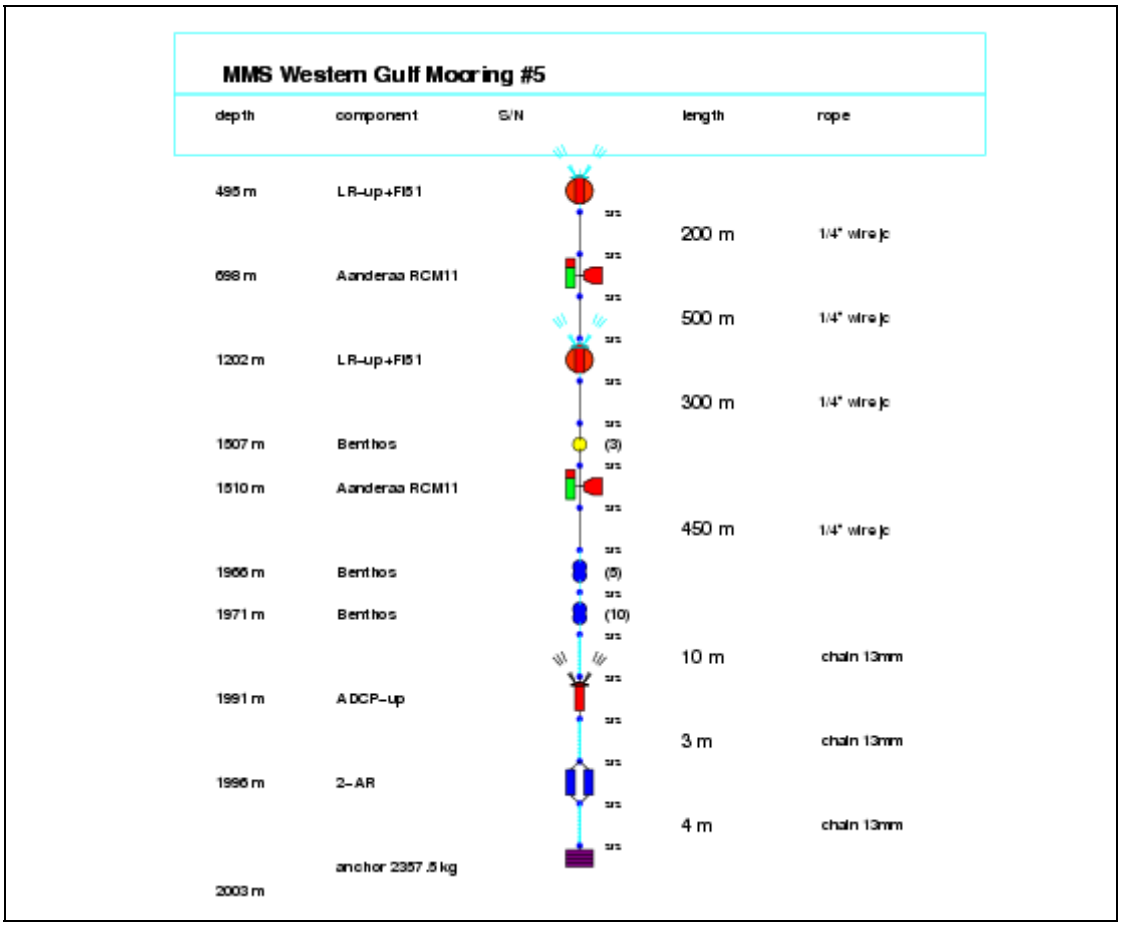

Figure 3. Vertical distribution of instruments on the five moorings (continued).

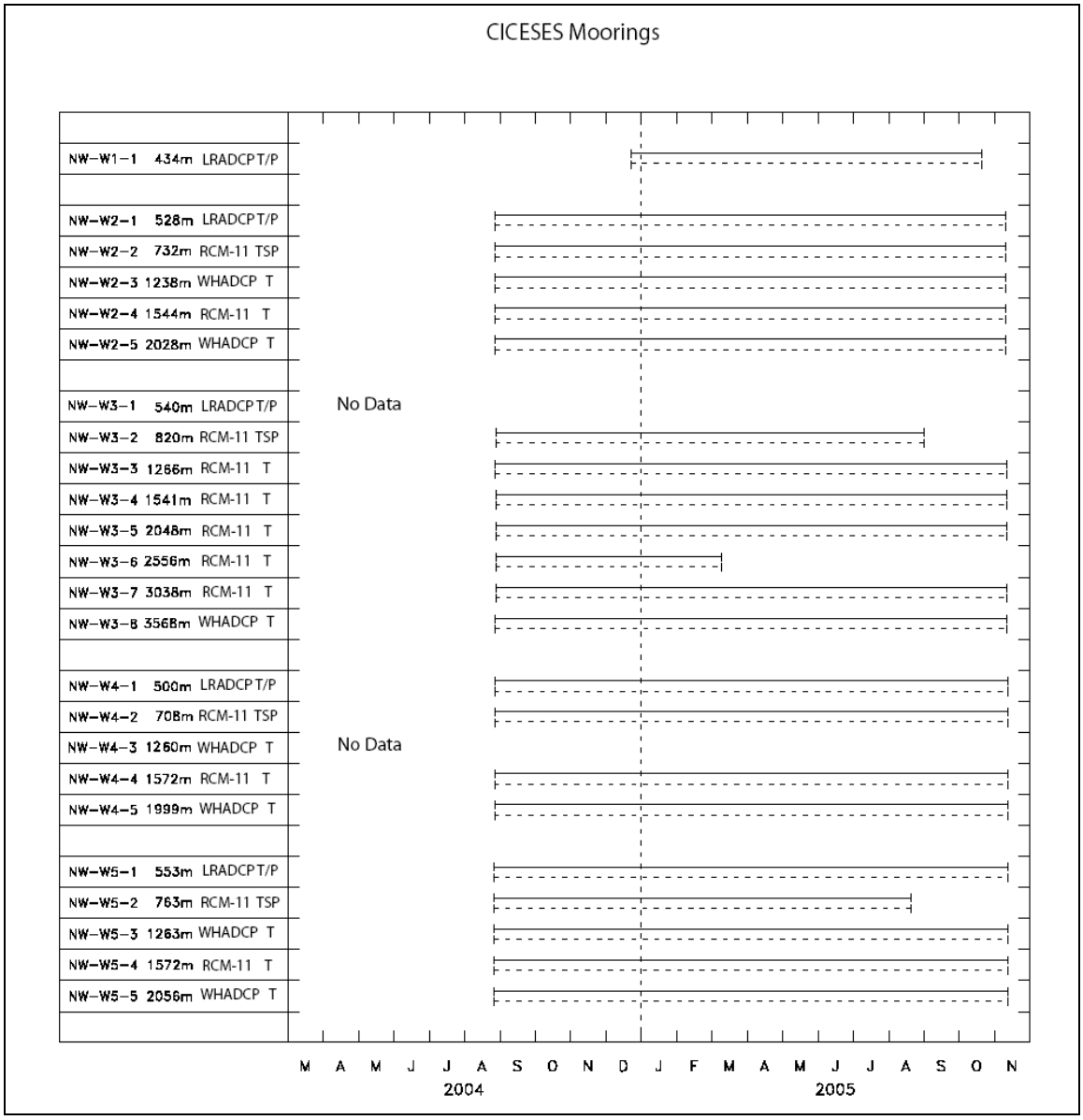

Figure 4. Data records obtained by the instruments in each mooring.

The pressure sensors on some instruments showed remarkably small vertical excursions of the moorings, with a maximum down-draft of 5.4 m for the moorings over the shelf and slope, and only one event in which the deeper 3500 m mooring dipped down by 71 m in mid-March 2005, with a corresponding change in temperature of 0.12C, compared to the standard deviation of temperature of 0.55C, showing that the temperature correction for the vertical motion of the moorings was negligible (Hogg, 1991).

Table 1 shows the location (longitude, latitude) and deployment depth of the moorings.

Table 1

Location and Deployment Depth of the 5 Moorings.

Mooring	Longitude W (°)	Latitude N (°)	Depth (m)
MMS1	96.31	25.43	500
MMS2	95.43	25.38	2000
MMS3	94.88	25.27	3500
MMS4	96.08	24.65	2000
MMS5	96.30	24.04	2000

Figure 5 shows positions of hydrographic stations from NODC data base. One can clearly see that there are only 4 or 5 useful hydrographic stations near the study area. Unfortunately, time limitations during deployment did not allow us to carry out CTD casts. Such conditions make estimation of full depth temperature profiles based on point observations from the moored instruments not clearly valid.

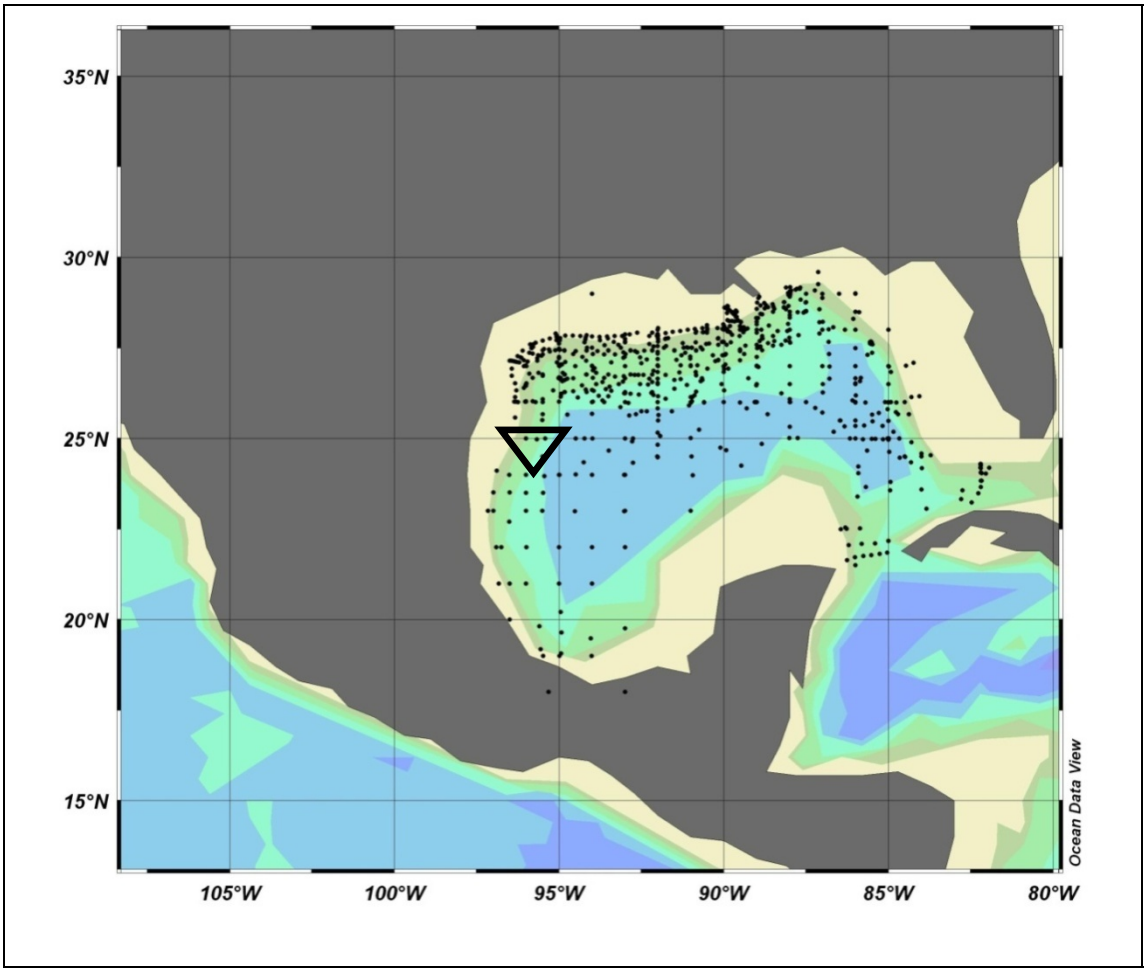

Figure 5. NODC hydrographic stations. Notice the lack of measurements near the mooring locations indicated by a triangle.

3. DATA ANALYSIS

3.1. MEAN CURRENT PROFILES AND BASIC STATISTICS

Figure 6 shows vertical profiles of mean current speed (left panel), standard deviation (middle panel) and the ratio of sub-inertial velocity variance to total variance. The magnitude of the mean currents are largest at the surface, as might be expected, however it is interesting to find that the largest mean current in the surface layer is observed in mooring MMS5 located in waters 2000 meters deep, while the largest variability in the surface layer is observed at the location of mooring MMS2, also installed in a location 2000 m deep (Figures 1 and 2).

It is found that the mean current below 500 m have less than 5 cm/s magnitude and the root mean square deviations at those depths are less than 10 cm/s in all locations, however, moorings MMS2 and MMS5 show a relative increase of mean current magnitude near the bottom while mooring MMS4 has a relative mean current maximum at around 1500 m depth. Figure 7 shows that the mean currents near the bottom are toward the south west in all three 2000 m moorings, while the mean currents increase significantly towards the surface and are directed towards the north east on moorings MMS1, MMS4 and MMS5. At mooring MMS2 the surface current is the smallest of all and southeastward. Recall that unfortunately there are no near surface measurements for mooring MMS3. Looking at the deep currents we find that on mooring MMS2 the mean current below 500 m, although small, increases toward the bottom while at mooring MMS4 there is a relative maximum at 1500 m. Moorings MMS3 and MMS5 both show a fairly uniform and small current from 1000 m down to the bottom.

The sub-inertial currents dominate the observed variability representing more than 60 % of the total variance at all depths except for a mid-water interval on mooring MMS5 between 1000 and 1300 meters depths where the ratio of sub-inertial to total variance gets as low as 47%. Worth noticing also is the fact that in the deep moorings (>2000 meters), there is a general tendency for the relative proportion of supra-inertial to sub-inertial motions to grow towards the middle of the water column at depths around 1200 meters being larger there than towards the surface or the bottom (right hand panels Figure 6).

The mean and (low pass) fluctuating currents denote three possible flow regimes in our study area. Mean currents were surprisingly small everywhere, flowing to the north and northeast only at about 10 to 20 cm/s near the surface over the edge of the shelf and slope (Figure 7), probably as an expression of the large anticyclonic gyre of the northwestern Gulf of Mexico (Nowlin and McLellan, 1967; Sturges and Blaha, 1976; DiMarco *et al*, 2005). Unfortunately, we lacked near surface data at the offshore mooring to confirm the offshore extension of the western boundary flow. From there, mean currents diminish quickly with depth, rotating clockwise over the shelf, so that by 400 m depth, the current is flowing to the south over the shelf's edge, but still flowing offshore over the slope. Figure 8 shows variability ellipses at different depths and also depict the mean current vectors. The current fluctuations are larger than the mean close to 40 cm/s near the surface, and diminishing rapidly to about 10 cm/s close to 400-500 m, the bottom over the shelf, and offshore over the slope (Figure 8). The current fluctuations are prevalently along the topography over the shelf, but without a preferred direction at those depths (400-500 m) over the slope, going from parallel (mooring 2) to almost perpendicular (mooring 5) to the slope.

Further at depth, below the shelf edge over the slope and the deep Gulf of Mexico, the topography separates two distinct regimes (Figure 8). Over the slope, current fluctuations are only about 10 cm/s, and oriented along the topography. Mean currents are even smaller, only a

few cm/s over most of the water column, but slightly intensify near the bottom forming a southerly jet trapped to the slope, suggestive of the deep flow posed by Welsh and Inoue (2000) and DeHaan and Sturges (2005). Over the 2000 m isobath (Moorings 2, 4 and 5, Figure 6) mean flow is a bit larger than the rms fluctuations just above the bottom, the only portion of our study area where the mean flow becomes larger than the fluctuations. Farther offshore (Mooring 3), in the very deep Gulf of Mexico, the mean is insignificantly small, but the fluctuations are close to 10 cm/s and in a predominant north-northeast direction throughout the water column. Such a barotropic distribution of the currents is to some extent similar to the current variability found in the deep central Gulf of Mexico (Rivas, *et al*, 2005, 2008) below the surface layers under the influence of eddies. However, in contrast to that study, we only find some intensification of the variability toward the bottom on mooring 3, but not in the moorings along the slope. This intensification is one of the signatures of topographic Rossby waves (Hamilton, 1990, 2007).

A more thorough analysis of the current variability is carried out below (Sections 5 and 6) using rotary spectral analysis and complex empirical functions. But before we do that, it is necessary to look in more detail at the actual time series which feature a series of events related to the presence of eddies and/or strong wind forcing in the area.

For completeness and reference, a set of 5 tables containing the basic statistics (mean, standard deviation, maxima, minima) of the horizontal velocity components is included in Appendix A.

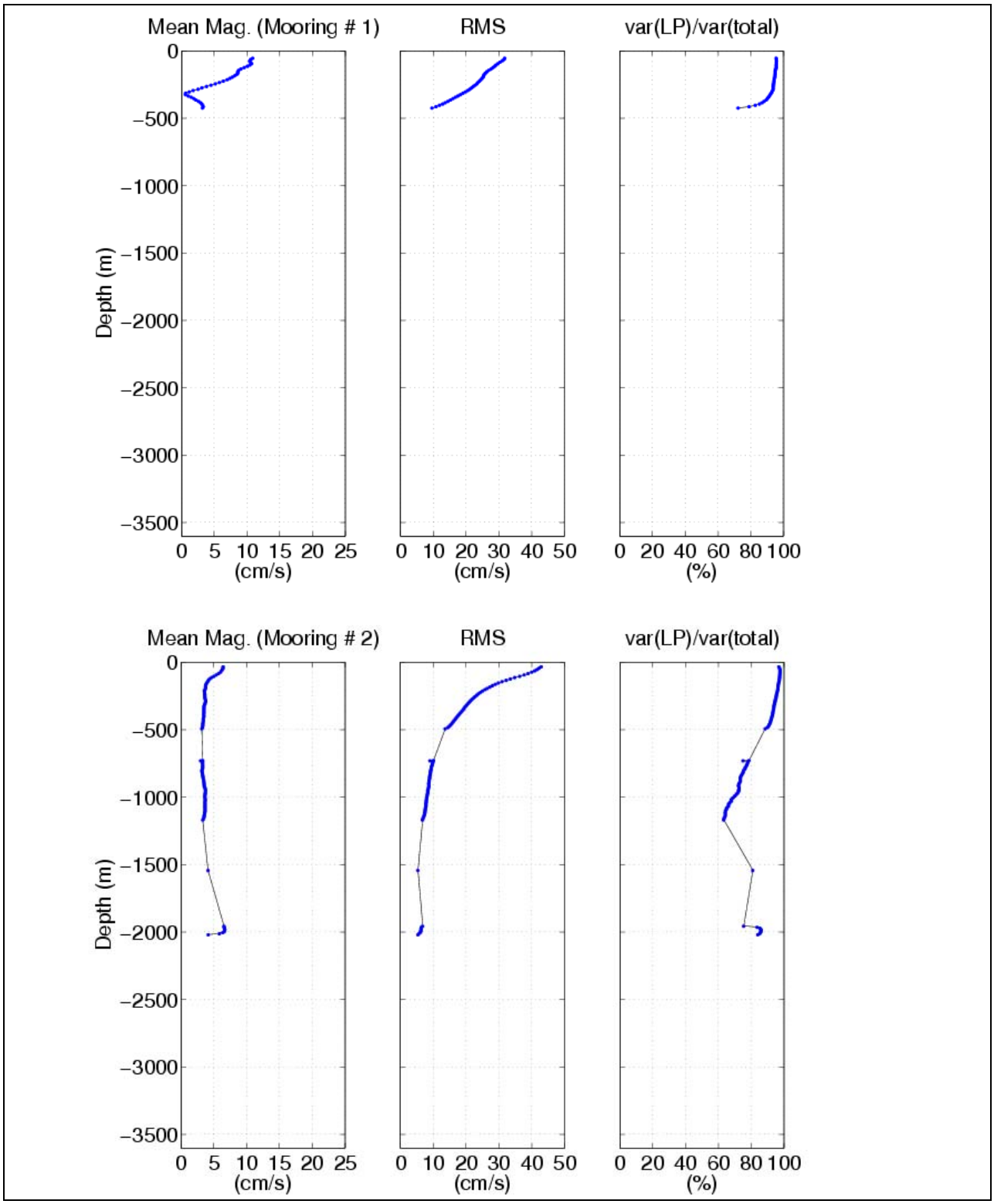

Figure 6. Profiles of mean current magnitude, root mean square (RMS), and ratio of subinertial to total current variance measured by the instruments on each mooring. Points at about the same depth but with slight different values correspond to overlapping measurements by an Aanderaa current meter and an ADCP.

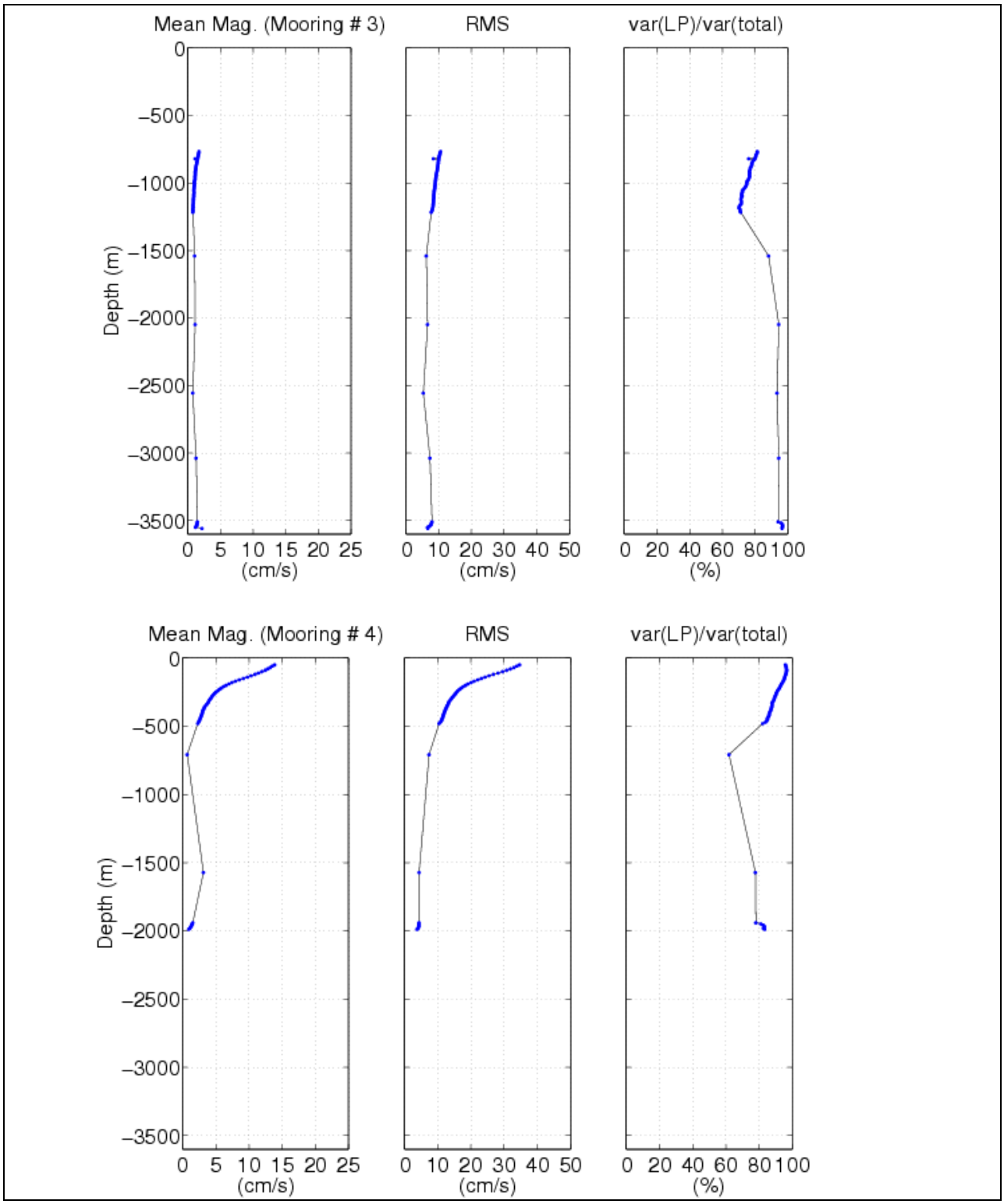

Figure 6. Profiles of mean current magnitude, root mean square (RMS), and ratio of subinertial to total current variance measured by the instruments on each mooring. Points at about the same depth but with slight different values correspond to overlapping measurements by an Aanderaa current meter and an ADCP (continued).

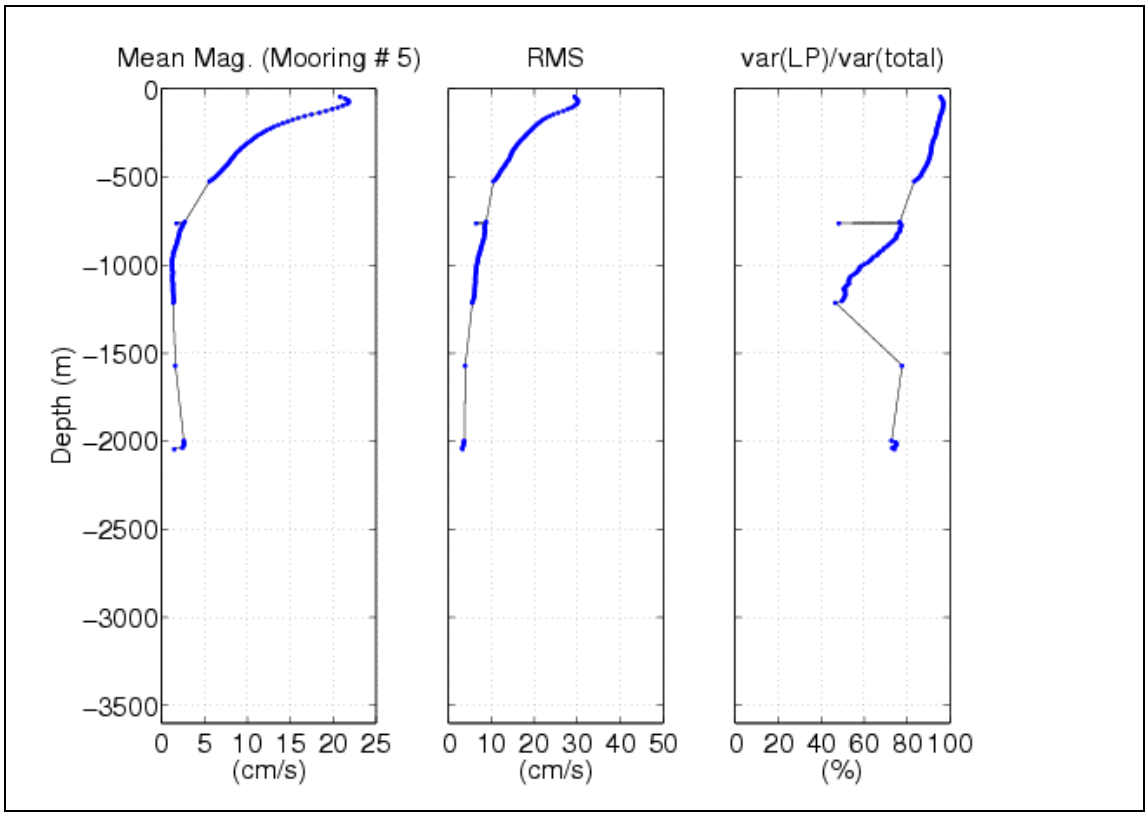

Figure 6. Profiles of mean current magnitude, root mean square (RMS), and ratio of subinertial to total current variance measured by the instruments on each mooring. Points at about the same depth but with slight different values correspond to overlapping measurements by an Aanderaa current meter and an ADCP (continued).

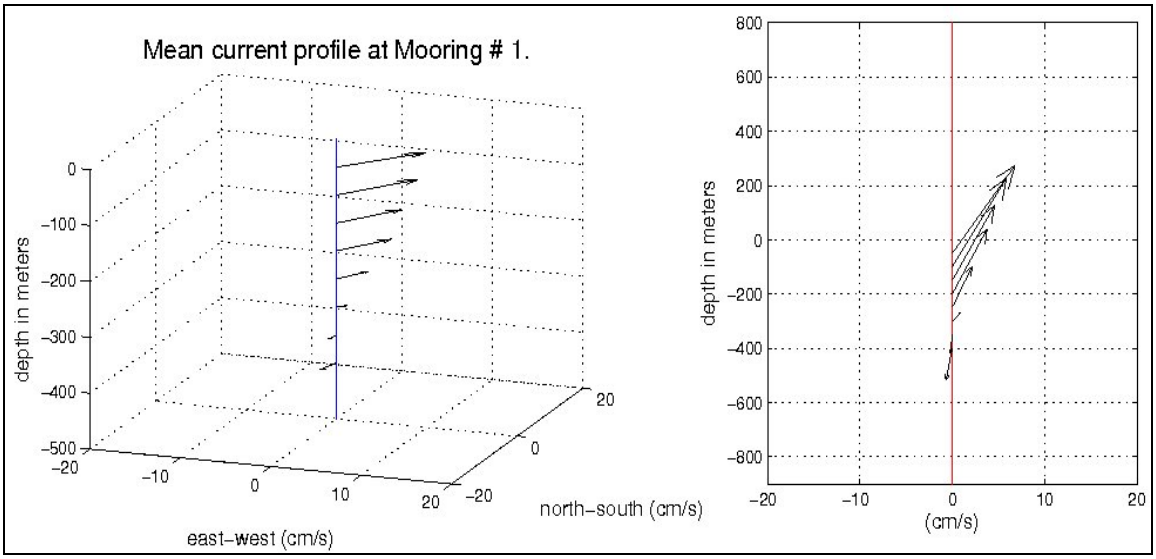

Figure 7. Mean current profile observed at each of the five moorings. The two panels show the profile in two equivalent representations, on the left, vectors in 3-D space, and on the right, vectors in 2-D with the north-south/east-west component in the abscissa/ordinate directions and each vector starting at its corresponding depth.

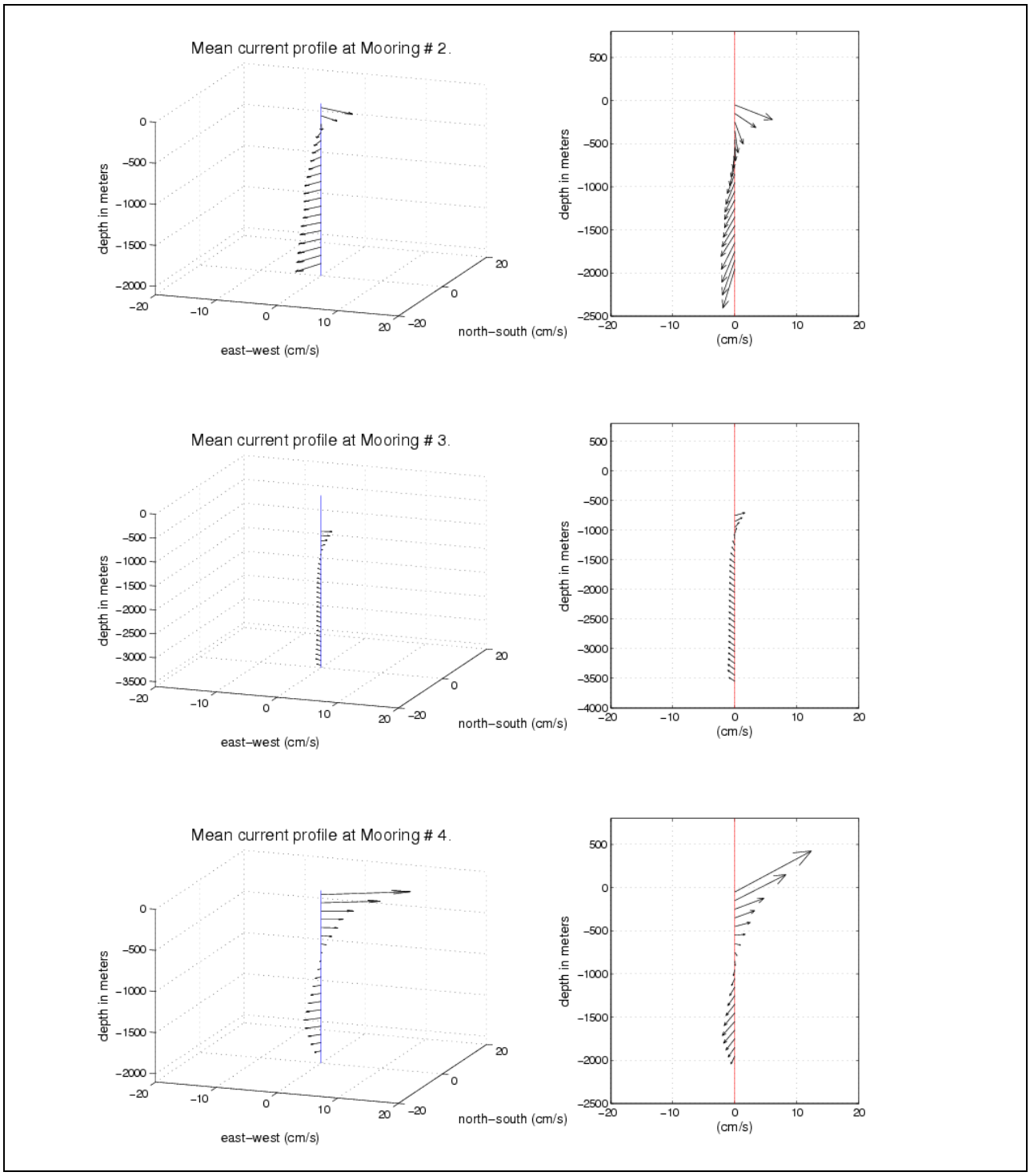

Figure 7. Mean current profile observed at each of the five moorings. The two panels show the profile in two equivalent representations, on the left, vectors in 3-D space, and on the right, vectors in 2-D with the north-south/east-west component in the abscissa/ordinate directions and each vector starting at its corresponding depth (continued).

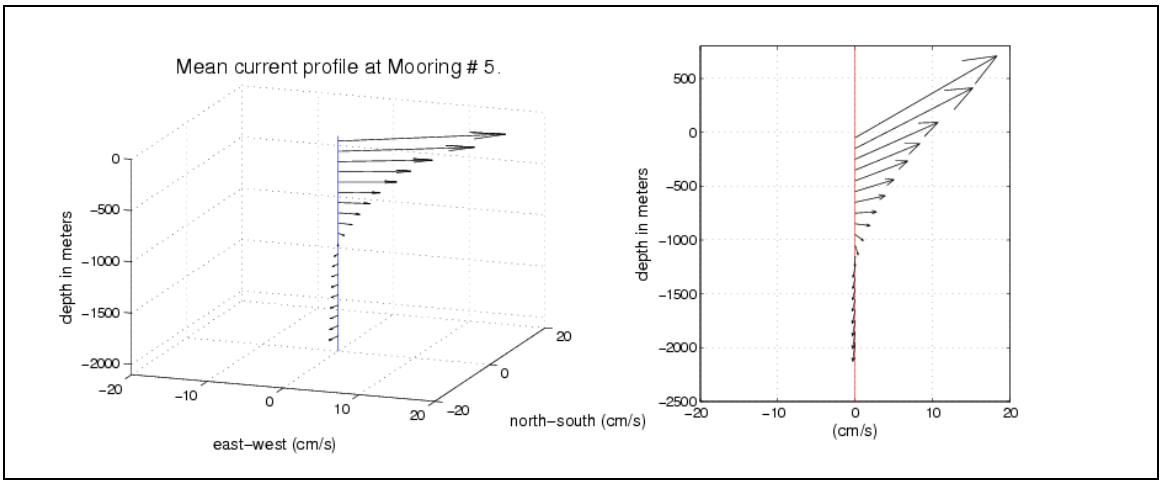

Figure 7. Mean current profile observed at each of the five moorings. The two panels show the profile in two equivalent representations, on the left, vectors in 3-D space, and on the right, vectors in 2-D with the north-south/east-west component in the abscissa/ordinate directions and each vector starting at its corresponding depth (continued).

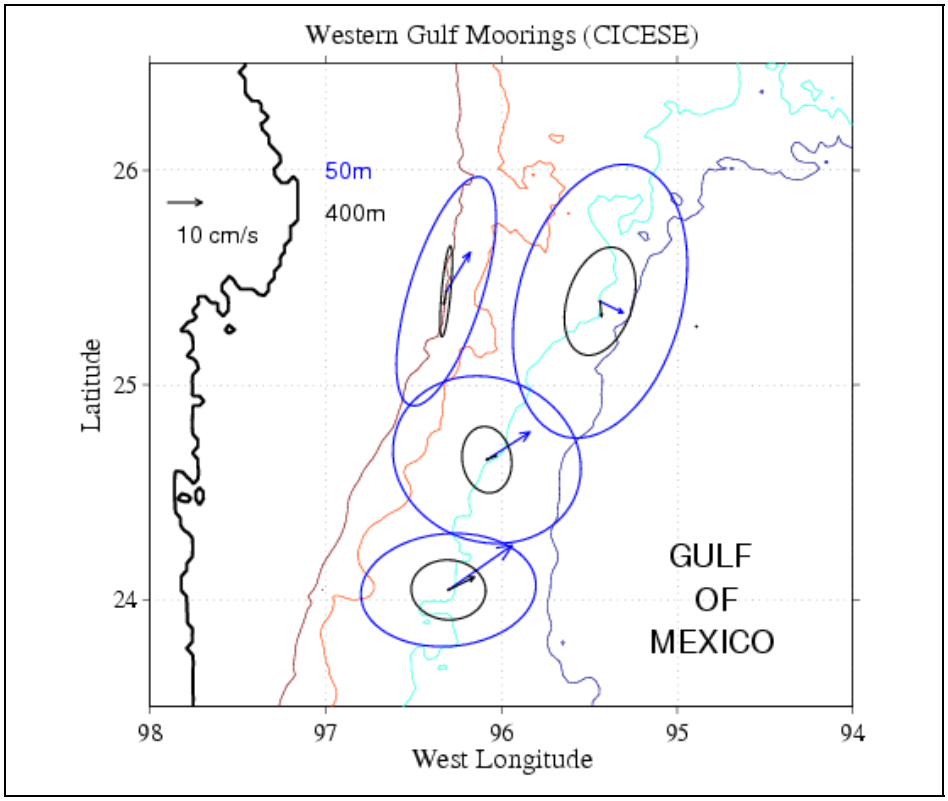

Figure 8. Mean and low-pass variability ellipses of the measured currents at the indicated depths. Note the different scales in each panel.

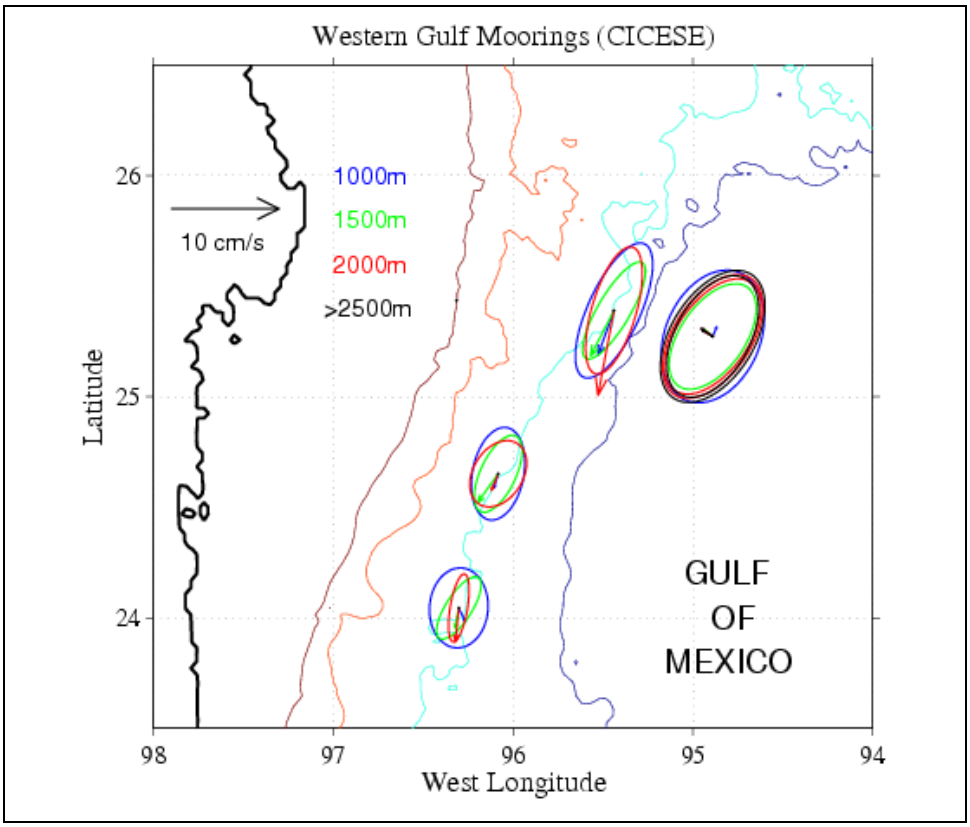

Figure 8. Mean and low-pass variability ellipses of the measured currents at the indicated depths. Note the different scales in each panel (continued).

4. DESCRIPTION OF THE VARIABILITY

4.1. EDDY FIELD FROM ALTIMETRY DATA

Since, as will be shown in the next sections, most of the observed variability is related to the presence of eddies in the area, before describing the mooring observations we carry out a thorough analysis of altimetry data. The processes involved are very complicated and include eddy-eddy, eddy-topography interactions and strong wind forcing events. One may think there might be different interpretations of the altimetry data, but the figures leave little room to maneuver and clearly show what is happening.

The Loop Current pinches off over itself sporadically and sheds a large warm, anticyclonic eddy that extends several hundred meters in depth and propagates in a west-southwest direction across the Gulf of Mexico until it intersects the coastal features of the western gulf. Given the breadth and depth of most eddies, this really happens rather far away from the shore itself, as the eddy begins to perceive the shoaling of the bottom over the slope and at the shelf's edge. The path each eddy follows from its region of generation can vary somewhat, from a southerly trajectory through the middle of the gulf, to a more northerly one south of the northern escarpment. Although it has been suggested that eddies follow either of three distinct paths, they probably can travel through a range of directions between the two aforementioned extremes. What is clear is that eddies usually remain in water deeper than the shelf's edge, and very few actually travel into the 'eddy graveyard' region in the extreme northwestern gulf.

Eddies are conveniently detected through satellite altimetry, for which we use the sea surface elevation anomaly combined from the Topex-Poseidon, Jason-1, and GFO satellites, as offered by the AVISO website[1] (the altimeter products are produced by Ssalto/Duacs and distributed by AVISO, with support from Cnes). This information has a 1/3 of a degree spatial resolution, and 3.5 days temporal resolution. From these data, three LC eddies were present or appeared at various phases of their development during the times our instruments were deployed and serve to illustrate the behavior of the eddies as they separate from the Loop Current, travel to the west, approach the coast and disappear. The current meter records then serve to document the effect of the eddies on the currents in the region of our observations. It is a pleasant surprise that even though use is made of interpolated altimetry data, the size and behavior of the eddy structures we identify in it, even its form and size, appear to be consistent with the mooring data.

As the moorings were being deployed, eddy Titanic (eddies are named alphabetically in chronological order in the fashion of hurricanes by Eddy Watch, (a service of Horizon Marine, Inc.), which had formed on December 31, 2003, and traveled along a southern trajectory, was present on August 28 of the following year at 21.53ºN; 95.64ºW, when its center was in about 2000 m of water off the coast of Veracruz (see Figure 9). It then traveled to the north, with its center remaining close to the 2000 m isobath, reaching 24.5ºN; 96.25ºW on September 15, becoming more elongated and weaker and difficult to identify by early October 2004. At about the same time on early October, a cyclone to the east of the now almost invisible Titanic and centered at 25.5ºN; 95.5ºW intensified. SSH anomalies (not shown) and the ssh field for early September suggest this cyclone is part of an anticyclone-cyclone pair, rotating clockwise on its axis. Whilst the anticyclone in this structure disappeared by the middle of October, the cyclone first intensified, then weakened (late October early November) and re-intensified through merging with other cyclonic anomalies particularly one to the east, related to eddy Ulysses (see

1 http://las.aviso.oceanobs.com/las/servlets/dataset

Figure 9). This intense cyclonic anomaly, labeled C1 for its importance, remained over the continental slope covering most of the mooring array (Moorings 1-4) until January 2005, when it started to elongate and weaken for a while, regaining strength and splitting in two, later in February (see Figure 10).

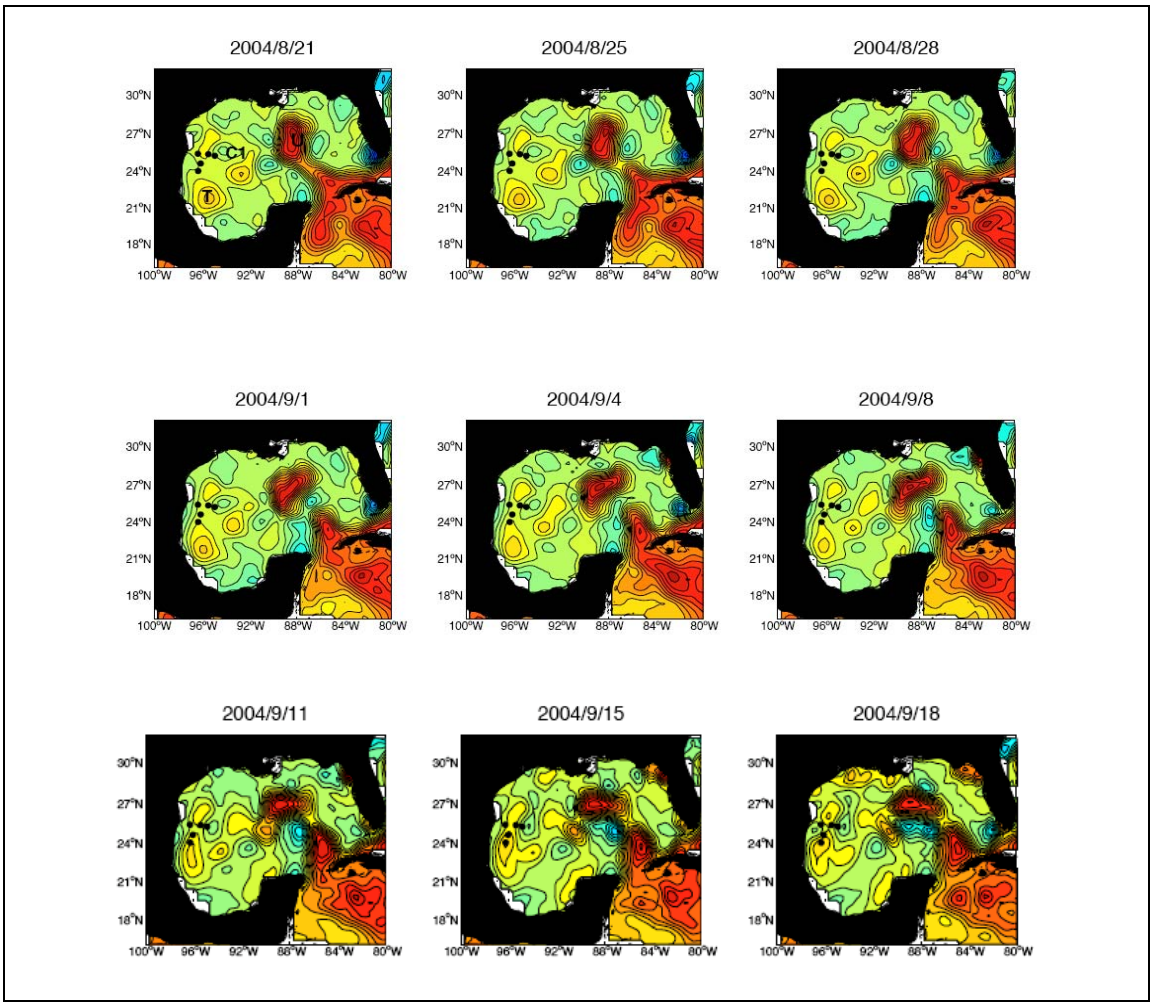

Figure 9. Snapshots of absolute sea surface height from the AVISO product showing the evolution of one of the remnants of LC eddy Titanic, the intensification of cyclone C1 over the mooring area through merging with cyclonic structure C2, which accompanies LC Ulysses. Ulysses is blocked by cyclone C1 and plays an important role in its subsequent splitting.

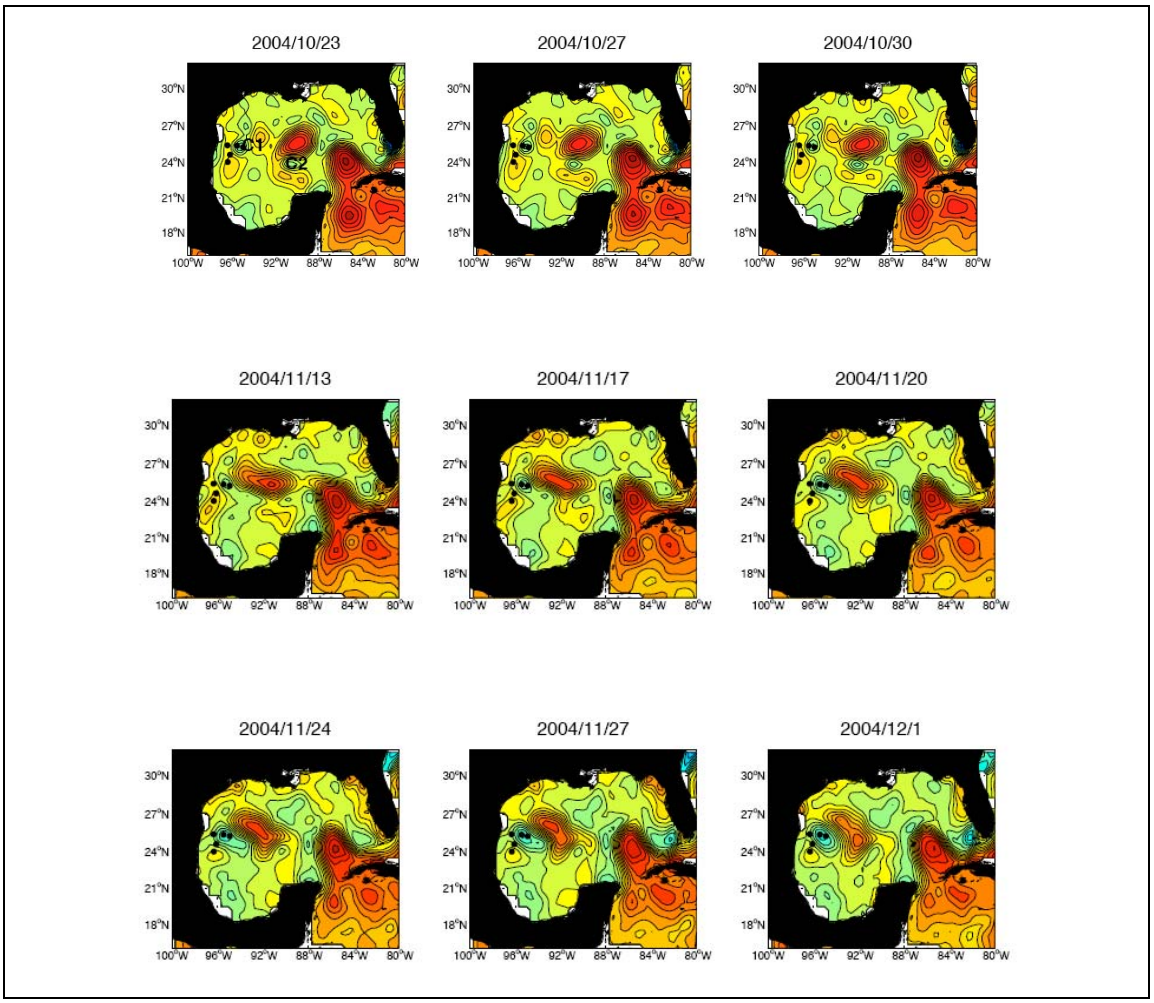

Figure 9. Snapshots of absolute sea surface height from the AVISO product showing the evolution of one of the remnants of LC eddy Titanic, the intensification of cyclone C1 over the mooring area through merging with cyclonic structure C2, which accompanies LC Ulysses. Ulysses is blocked by cyclone C1 and plays an important role in its subsequent splitting (continued).

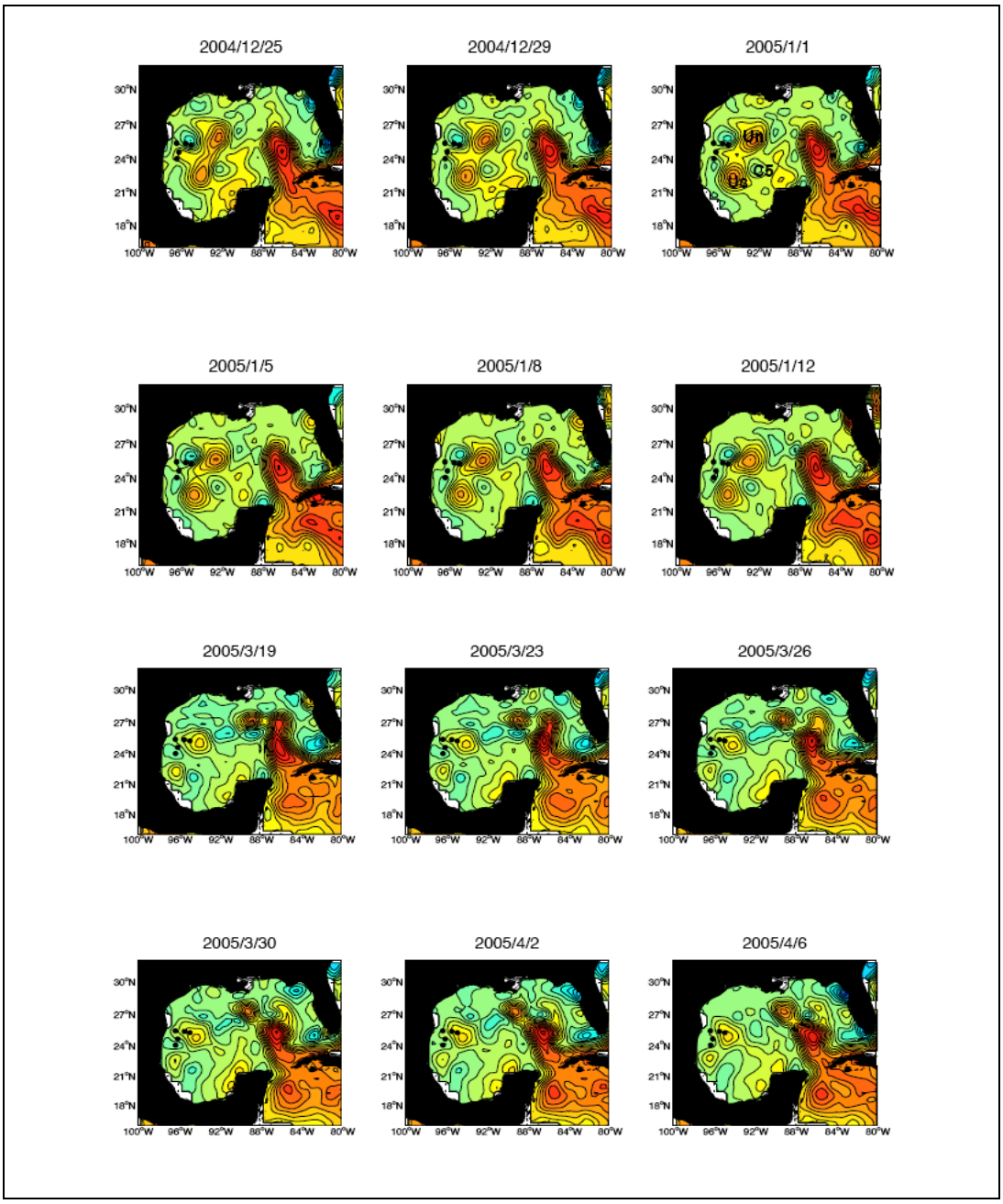

Figure 10. Snapshots of absolute sea surface height from the AVISO product showing first the splitting (top 6 panels) of eddy Ulysses, the northward along-slope movement of its southern byproduct UlyssesS (middle 6 panels), and its later merger with UlyssesN, forming a single anticyclone that covers the mooring array during April and part of May (bottom 6 panels).

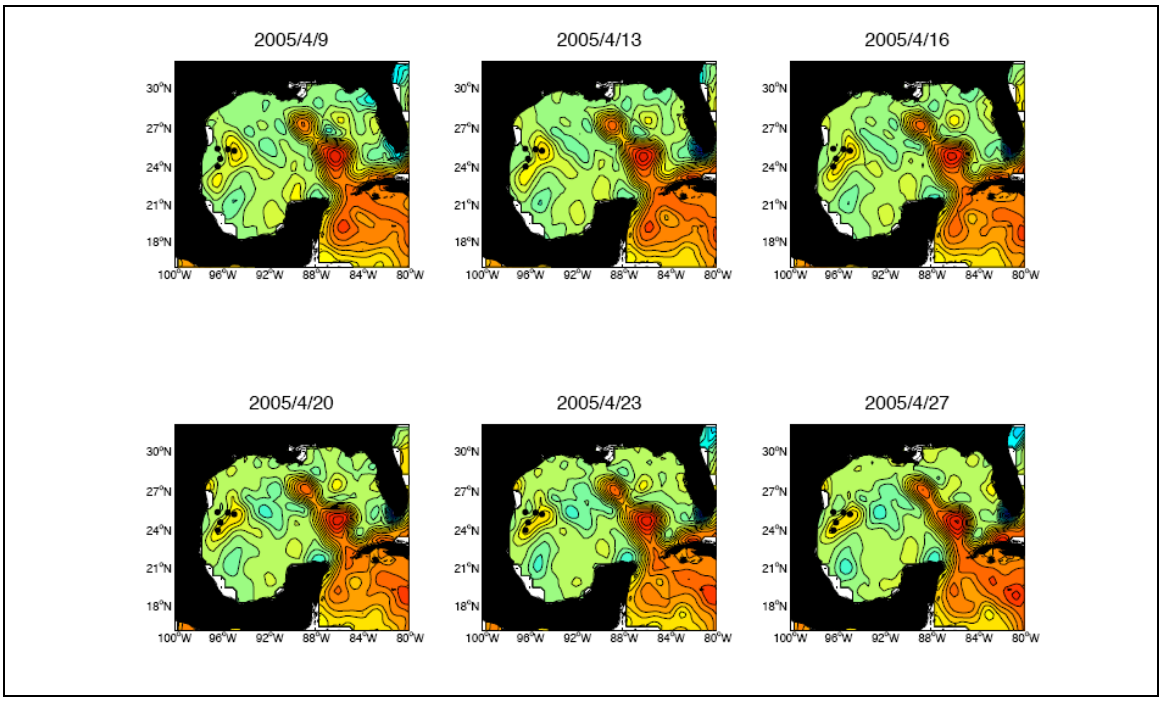

Figure 10. Snapshots of absolute sea surface height from the AVISO product showing first the splitting (top 6 panels) of eddy Ulysses, the northward along-slope movement of its southern byproduct UlyssesS (middle 6 panels), and its later merger with UlyssesN, forming a single anticyclone that covers the mooring array during April and part of May (bottom 6 panels) (continued).

On September 15, 2004, eddy Ulysses, one of the largest ever, detached from the Loop Current and proceeded directly to the west, accompanied by a much weaker cyclonic elongated structure (C2) to the south of it. On late November, the eddy pair collided with the cold structure C1, which merged with C2 to form a cyclonic structure that blocks Ulysses from reaching the continental margin (25.25ºN; 95.5ºW). On early December, with both cyclones fully merged, Ulysses began to stretch in two branches, with the northern half remaining close to where it was, but with the southern half (UlyssesS) traveling towards a southwesterly destination near 22ºN; 96ºW, where it would remain from February to March 2005. The splitting process involved the intensification of a trailing cyclonic structure (C5) and cyclone C1 in a process resembling the formation of a LCE by a Tortugas and Campeche Bank cyclones strangling the LC. Ulysses clearly split in two at the very end of December, with C5 attached nearly in a stationary position to the northeast of UlyssesS while it remained at that southerly position. In early March 2005, UlyssesS started traveling to the north and Ulysses N began stretching to the west while C5 apparently rotated to the south and grew in size weakening in that process. At the same time, around the middle of April, the two halves of Ulysses merged again to form a single large anticyclonic eddy. It seems the array capture its rim, since very high velocities are observed during April at several moorings (see Figures 10 and 11).

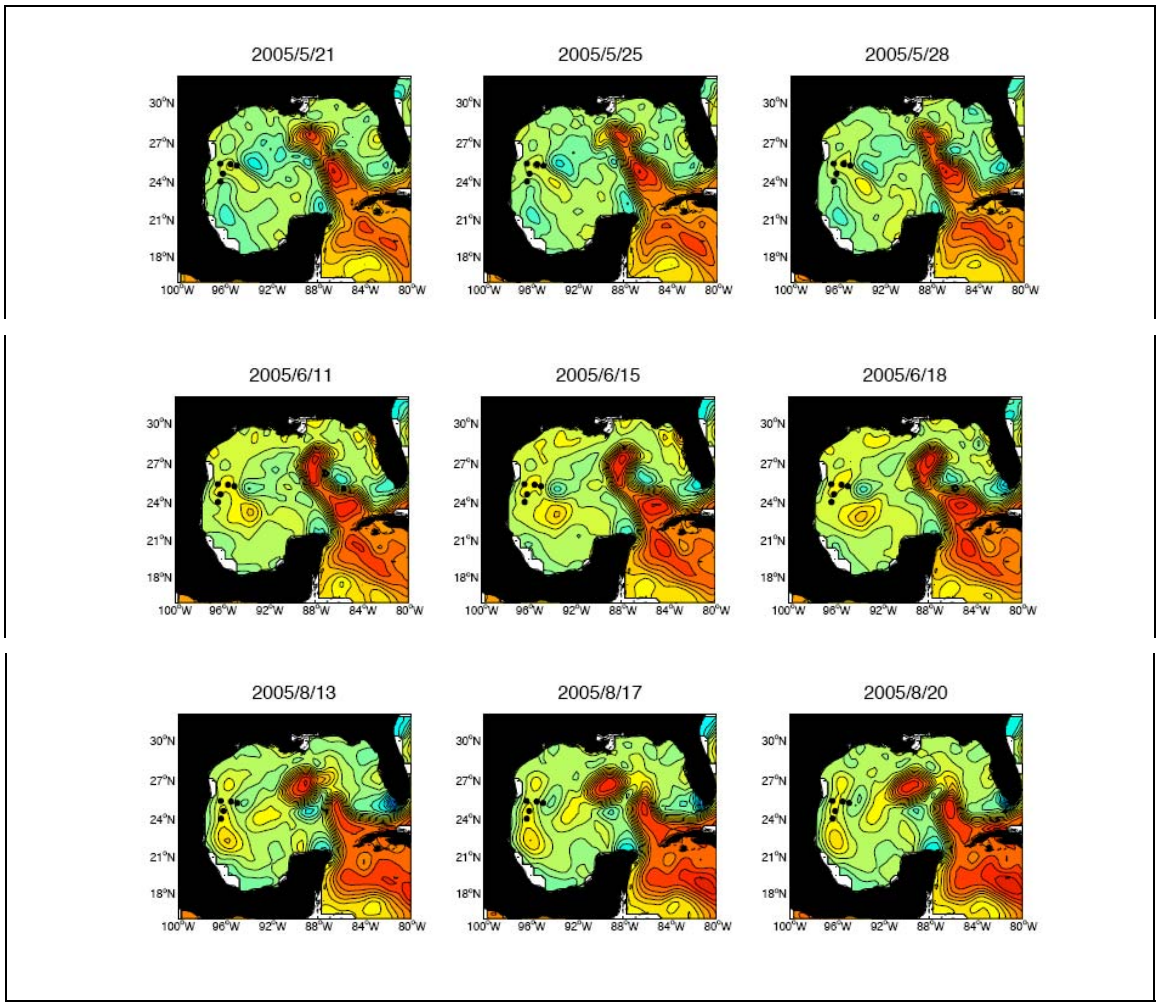

Figure 11. Snapshots of absolute sea surface height from the AVISO product showing the southeastward movement, splitting, and reattachment of "merged" eddy Ulysses, which formed in late March and April 2005 (see Figure 10).

As these displacements were taking place, the fused cyclones (C1-C2) were pushed to the north over the shelf, where they became undetectable by late March when UlyssesN moves over the mooring array before merging with UlyssesS. The ssh data suggests that during May 2005, Ulysses begins to stretch and move on a clockwise path down to 22ºN, strengthening at its southeastern end, moving back west and splitting in two one more time (June 2005). Thereafter, while moving along the shelf back north, it merges once again with its weaker northern part forming a large stretched anticyclone along the western slope (August-September 2005). This stretched anticyclone remains detectable until middle October (see Figures 11 and 12).

A few other cold structures had an impact on our measurements. Although their origin and time history is rather more fuzzy than the others mentioned before, we labeled them C4 basically because they do impact mooring observations in the last part of the observing period. Starting in early February, 2005, one notices that the northern split product of the merged cyclone C1-C2 is rotating clockwise on the rim of UlyssesN. This cyclone merges with other anomalies to the east of UlyssesN and later with other cyclonic features surrounding “remerged” Ulysses eddy formed

in April 2005. Its associated cyclonic circulation impacted the mooring region from August onwards particularly during October 2005.

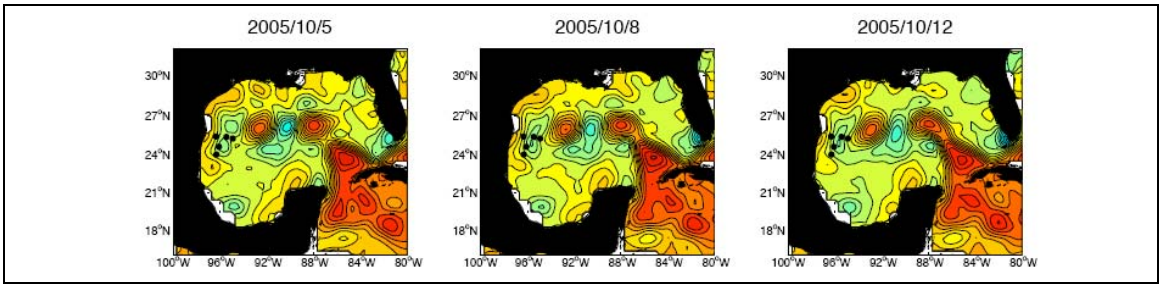

Figure 12. Snapshots of absolute sea surface height from the AVISO product showing cyclone C4 sitting over the mooring array. This eddy formed by several merging processes (see text for details).

On the second half of September 2005, a third eddy, named Vortex, was released from the Loop Current. It traveled directly to the west, approaching the region of our moorings from a northerly direction in by late October. Although cyclone C5 becomes smaller from late October and during November, it blocks eddy Vortex fully entering the mooring array zone. Hence it appears that only moorings MMS2 and MMS3 may have sampled eddy Vortex during that period. Unfortunately, there are no near surface measurements at mooring MMS3. The moorings were pulled out in December, so the effect of the eddy on the currents recorded lasted a bit less than 1.5 months (see Figure 13).

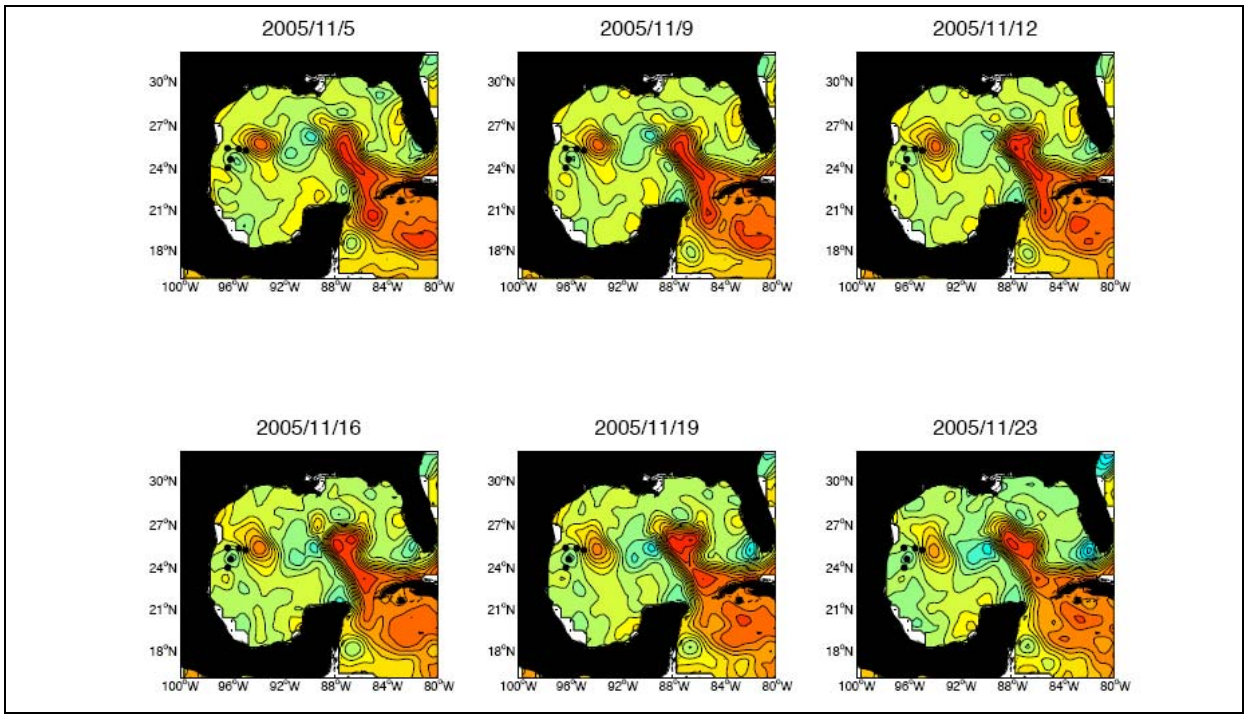

Figure 13. Arrival of LC eddy Vortex to the mooring array area. Vortex does not move into the mooring zone since its blocked by cyclone C4.

The behavior of the eddies can be summarized by the trajectories of the centroids (Figure 14). Titanic lasted 11 months, and followed a southerly path, reached the slope, and proceeded north. Ulysses lasted 12 months, followed a more central path, split into two halves, of which the southern one behaved essentially like Titanic had, moving north after reaching the slope and merging again with the northern half of the original eddy. It, nonetheless, seemed to possess larger amounts of energy, for it then repeated the clockwise path through the south before breaking up along the slope. Vortex followed a more northerly path, and took six months to move into the region of the moorings, when we ended the observational effort. The three eddies represented the various paths that have been proposed as typical behavior of the Gulf of Mexico eddies by Vukovich and Crissman (1986) from 11 years of data, and by Vukovich (2007) with 23 years of data. It appears that the lifespan, length of path, and the minimal distance to the coast of eddies is a function of their size, with Ulysses, the largest, lasting over a year, had to repeat the clockwise cycle near the coast to dissipate, and remained at more than 400 km form the coast. Vortex, the smallest, lasted only six months, and broke up before reaching the coast. Titanic was a medium sized eddy, lasted for 11 months, and got as close as 170 km from the coast. A rule-of-thumb appears to be that the center of the eddies never penetrates regions where the water depth is less than 2000 m. The time the eddies lasted after reaching the coast for the first time, 5 months for Titanic, and 9 months for Ulysses, were all spent in a region delimited by the 23.5 – 24.8º N and 93.5– 97º W, off the coast of Tamaulipas, Mexico. When the eddy was especially energetic, it cycled more than once around the area.

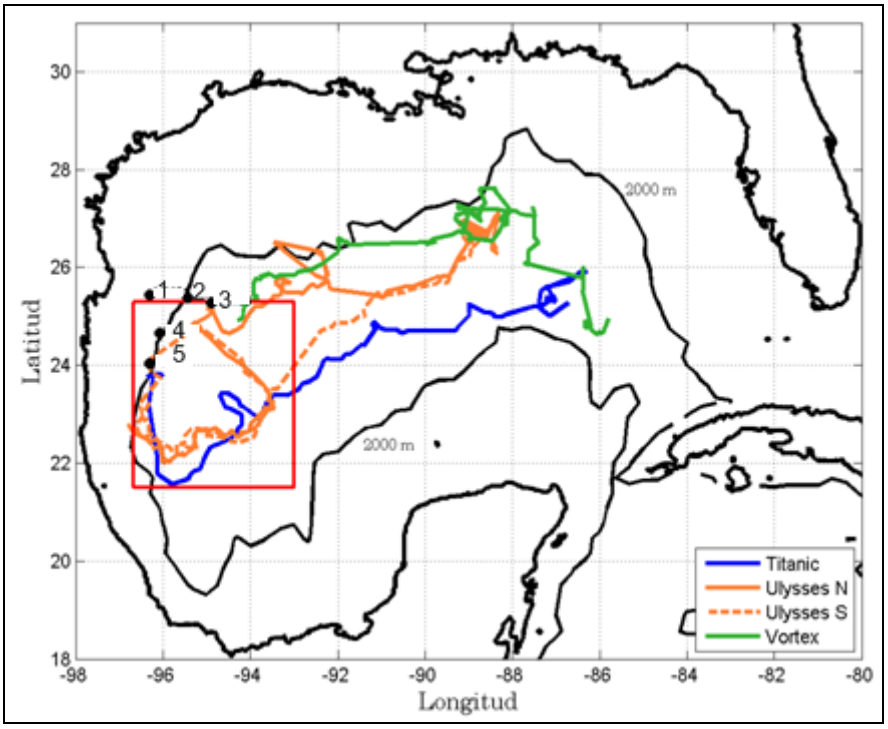

Figure 14. Trajectory of four LC eddys from December 2003 until November 2005. Red square shows the region where the eddies either dissipated or loose its coherent circular form.

The cold, cyclonic eddies were typically smaller than the warm eddies, the exception being some merger cases such as the larger C1-C2 combination that was able to split eddy Ulysses in two halves, and remain for several months with a diameter of close to 100 km.

The following section describes the mooring time series where it will be shown that the eddy events just described explain a great deal of the observed variability.

4.2. MOORING OBSERVATIONS

In spite of the loss of two complete current profilers, we recovered a rich data set, useful to describe the regional circulation over the edge of the shelf and slope of the Northwestern Gulf of Mexico. The flow is predictably dependent on the bathymetry and depth, with three different regimes occurring over the shelf, the deep slope and the abyssal plain. It is shown below, that flow in all regions is affected by the presence of eddies and most of the high velocity events detected in the time series can be associated with them. However, obviously there are other processes affecting the variability besides the eddies, particularly strong wind events, among them "Nortes" and hurricane Emily that leave their mark in the time series. Spectra of the variability is red and the most energetic signals are sub-inertial, but high frequency signals (inertial and supra-inertial) are ubiquitous and in some cases as energetic as low frequency ones. Following is a description of the variability. Afterwards rotary spectra and complex EOF analysis (Sections 5 and 6) will help us in its interpretation.

4.2.1. Flow Over the Shelf Break

Figure 15 shows vector time series of low-pass subinertial currents at several depths in mooring MMS1 (which consisted of a single ADCP, see Figure 3). Recall these time series begin until December due to a problem with the acoustic release which forced us to recover and redeploy the mooring (see Section 1). As mentioned in Section 2, the flow over the shelf edge, at the 500 m depth location, is mostly north-south along the topography. It appears to be divided into two main layers, with the upper levels dominated by large O (30-40 cm/s) fluctuations of a month's duration or longer that are very coherent in the vertical, extending down beyond 250 m depth and a predominant northerly flow during the summer, due to the presence of anticyclonic anomalies or simply because the wind-driven seasonal circulation of the region (Sturges, 1993). Below that level, events are shorter, close to a week in duration, reversals are frequent. Most fluctuations were smaller, of O(20 cm/s), and a few days to a week in duration, except for a large perturbation that began with a pulse of northerly flow and then dominated the entire water column during February 2005. The events seen in the top 250-270 m can be clearly associated with eddies as Figure 16 shows. The southward flow during February is associated with cyclone C1-C2 whereas the flow in March is related to the presence of eddy UlyssesN. In April, re-merged eddy Ulysses is to the east of mooring MMS1 and cyclonic circulation occurs over the mooring. The northward flow during summer is also related to the second arrival of Ulysses in the area as Figure 11 above shows. The southward flow seen in the whole water column in the last part of the record is interesting because it appears first in the flow near the bottom in early September when the flow at the surface is still northward (associated with an anticyclonic feature in the altimetry). Later in October and November, cyclone C4 is over the mooring area so the flow is coherent throughout the water column. Both events occurred in summer, when the winds and wind stress curl are small (Sturges, 1993; DiMarco *et al.*, 2005). Worth noticing is the fact that the flow below 300 meters is in general different from the one above but not opposite, in the

sense of a first baroclinic mode, showing perhaps that the exchange between the flow on the slope and the shelf edge is quite complex.

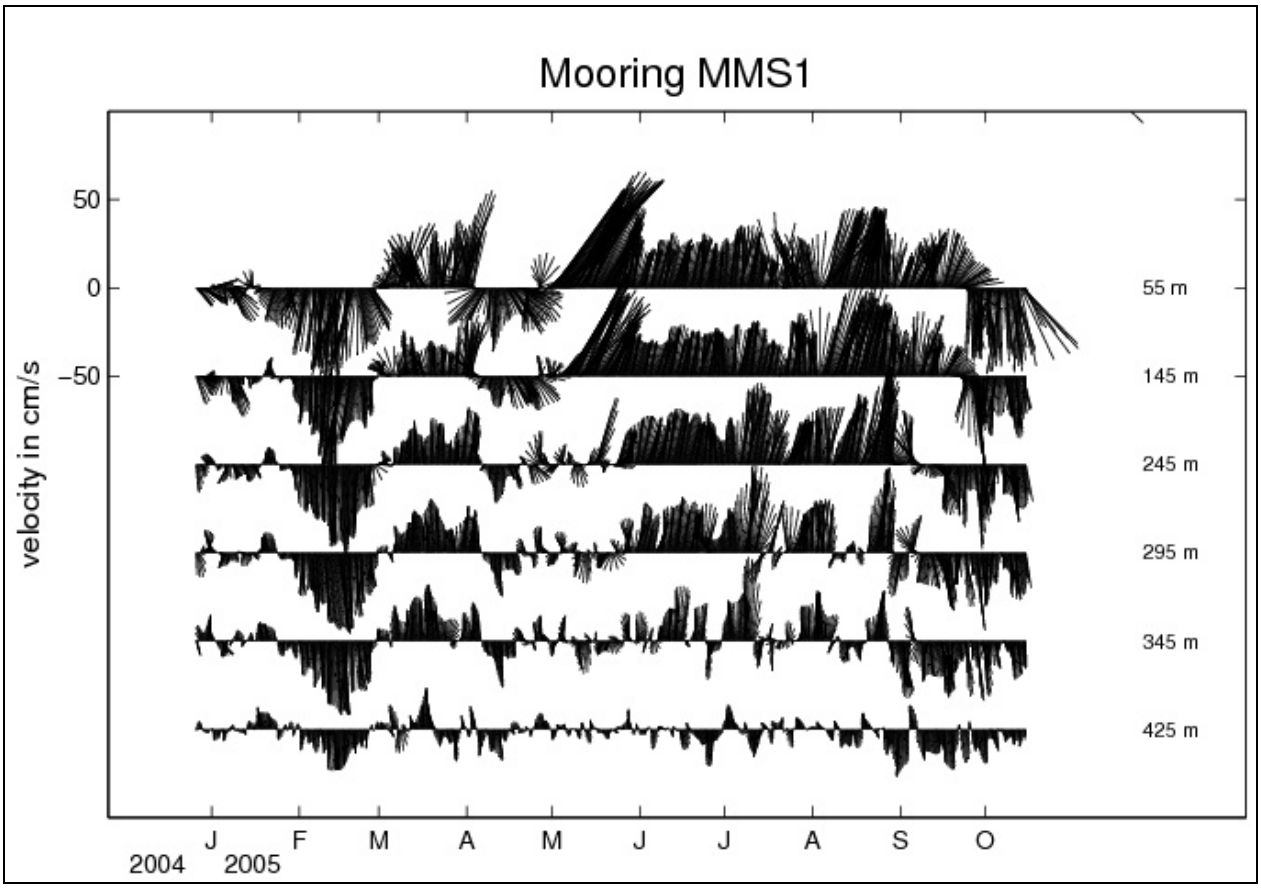

Figure 15. Vector time series of the currents measured at the shelf edge, in 500 m of water, in the northwestern Gulf of Mexico.

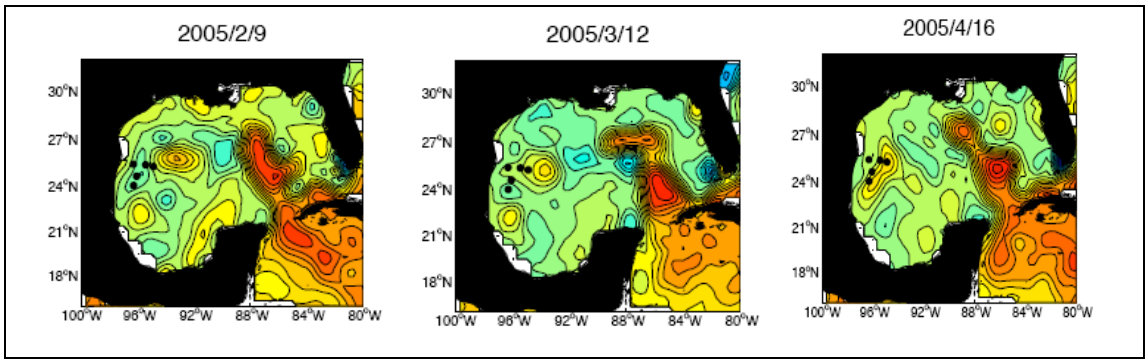

Figure 16. Snapshots of altimetry data from AVISO, which explain the observed current events in Figure 15.

Figure 17 shows time series of total speed (top panel), high frequency speeds (periods less than 40 hours, middle panel) and total and high-pass vertically averaged kinetic energy. Figure 18 shows time series of winds at the nearby NDBC station 42002. The middle panel in Figure 17

clearly shows the generation of high frequency motion and its downward propagation at the end of July 2005 due to the presence of hurricane Emily which crossed over near the mooring area on July 20. High frequency kinetic energy (Figure 17 lower panel) shows that near and supra inertial motions lasted for about 10 days, until the beginning of August and contributed close to 50% to the total kinetic energy. Other minor high frequency events occur between January and April and seem to be related with northern wind events ("Nortes") as Figure 18 shows. The one occurring in April is interesting since it is slightly more energetic at about 200 m depth than at the surface. The full speed time series (Figure 17 top panel) depicts the complicated and highly variable structure of the flow. Worth noticing again is perhaps the last part of the record (September onwards) which shows the initial intensification of the flow at the bottom.

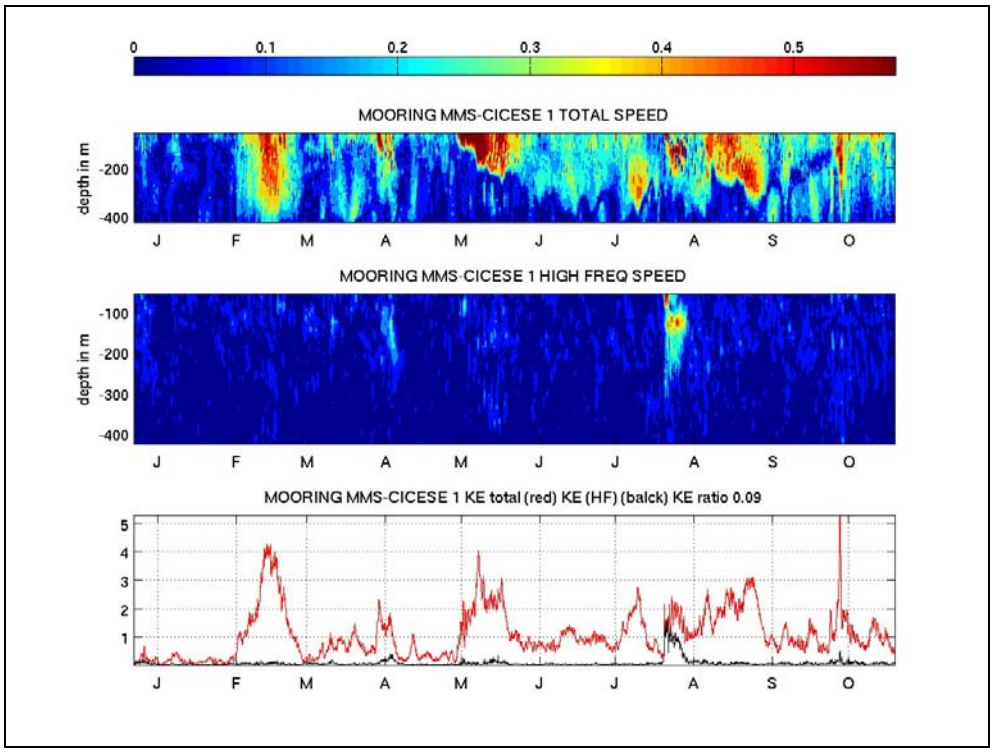

Figure 17. Time series of total speed vs depth (top), speed of high-pass velocity series (middle), and time series of total (red) and high-frequency (black) kinetic energy for mooring MMS1. Speeds in m/s and kinetic energy in (m^2/s^2).

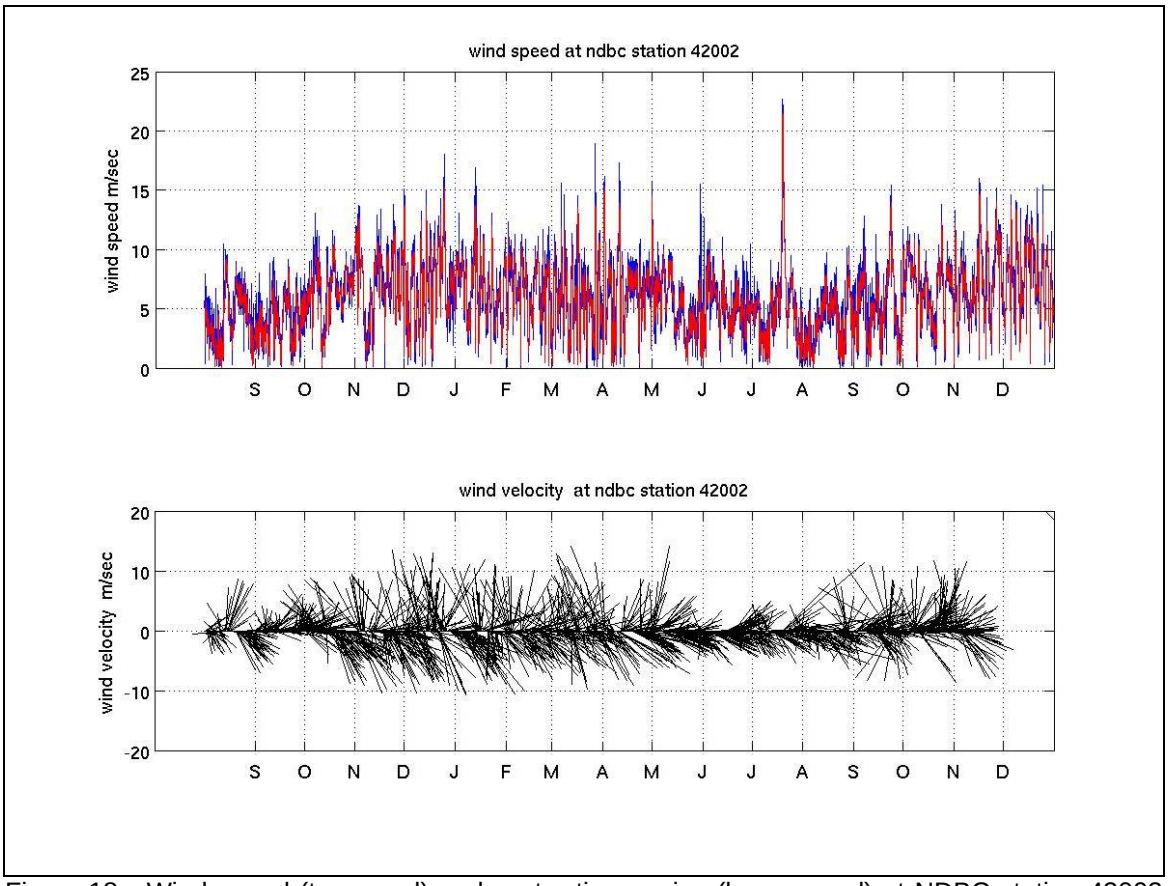

Figure 18. Wind speed (top panel) and vector time series (lower panel) at NDBC station 42002 located at 25.79° N 93.67° W. The red curve on the top panel is the 12 hour running mean.

Figure 19 shows total (blue) and high-pass (red) temperature anomalies at 435 m (from the ADCP's thermometer, top panel). Lower panel is the absolute sea level obtained from linearly interpolating the AVISO data to the mooring position. Notice the lack of correlation between bottom temperature and sea level. For example, during February 2005 while the flow is southward (cyclone C1-C2, Figures 15 and 16) and sea level is low, the temperature actually increases. Similarly, sea level increases from April to July and temperature basically just fluctuates. High frequency temperature fluctuations occur during high winds and clearly during hurricane Emily but also at other times when wind forcing is not particularly strong, such as during October 2005.

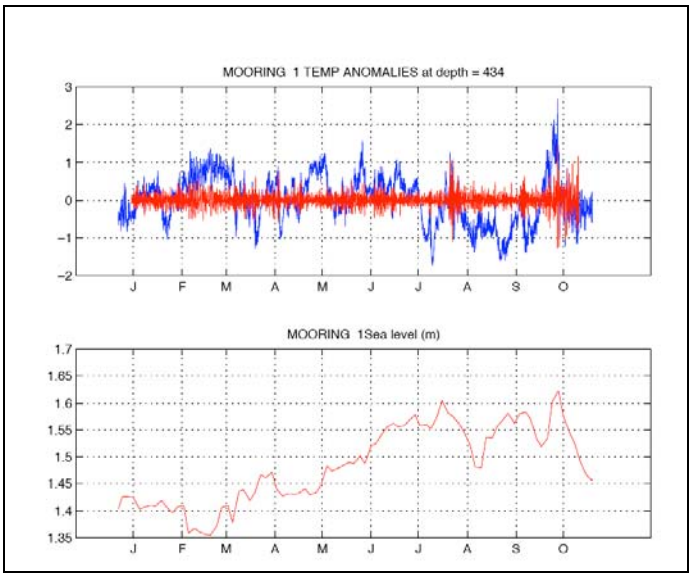

Figure 19. Total (blue) and high-pass (red) temperature anomalies at 435 m (from the ADCP's thermometer) (top panel). Absolute sea level obtained from linearly interpolating the AVISO data to the mooring position (lower panel).

4.2.2. Flow Over the Slope

Three moorings 2, 4 and 5 along the 2000 m isobath were supposed to document along-slope variations of the flow, while maintaining some degree of horizontal coherence. The records are surprisingly different from each other, with the upper 700 to 1000 m dominated by large events, and no discernible influence of a surface wind-driven layer. The current pulses in this upper layer are large, about one month duration, coherent with depth, although the current vectors tend to diminish and rotate with depth. We will examine the relation of these events to the passing eddies. Beneath, within the lower 1000 m, currents are smaller, only about 5 to 10 cm/s, but with very few reversals, so a net flow occurs near the bottom in the form of a steady southerly jet over the slope in the fashion of the cyclonic persistent circulation posited to exist at such depths by De Haan and Sturges (2005) and other authors. Altimetry data helps again to make sense of simultaneous different flow directions observed at the three moorings.

Figures 20, 21, and 22 show vector time series of low-pass filtered currents at different depths for moorings 2, 4 and 5 respectively. Currents decrease in the vertical but appear to be relatively coherent on the top 800-1000 m on moorings 2 and 4 (Figures 20 and 21). Notice vertical coherence is less clear on mooring 5 even on the top 400 m, or in other terms, currents at mooring 5 in the top 1000 m rotate in the vertical much more than in moorings 2 and 4.

Going back to Figure 9, one finds that from October to December cyclone C1 is over mooring 2. Mooring 4 samples the southern rim of C1 and the northern rim of the anticyclone byproduct of Titanic. Mooring 5 appears to sample just anticyclonic features either associated with Titanic or the arrival of Ulysses. The vector time series in the top layer (0-800 m) agrees with this picture: flow is mostly southward in mooring 1, eastward-southeastward in mooring 4 and northward-eastward in mooring 5. Similarly, during April and May flow direction in the 3 moorings agree with the presence of re-merged eddy Ulysses. Comparing altimetry with other periods the same result applies: flow directions in the moorings are consistent with the features

captured by the altimetry data. The fact that these two different data sets (moorings and altimetry) agree, at least qualitatively, is quite encouraging.

Flow at higher depths indicates the persistent along-slope southward flow near the bottom, being particularly strong in moorings 2 and 5 and less at mooring 4. This suggests not a different regime at mooring 4, just that we did not capture the core of the bottom current there. It is difficult to establish a pattern for the behavior of currents between the bottom and 1200-1400 meters just looking at the vector time series (Figures 20, 21, and 22). One can see the flow being some times in the same sense as the bottom flow some others in the opposite sense. Same thing occurs with events on the top 900 m: the flow below 1200 m (but above the bottom) is in the same direction as the near surface flow on some occasions but opposite or just different in others. The EOF analysis carried out below (see Section 6) clarifies what are the main modes of variability and suggests the main mode is quite barotropic.

Figures 23-25 are similar to Figure 17. They show time series of total speed vs depth (top panel), speed of high pass velocity series (middle panel) and (lower panel), time series of total (red) and high frequency (black) kinetic energy for mooring MMS2, 4, and 5 respectively in the top 400-500 m. Notice color scales are slightly different to highlight events at different moorings, but that does not affect their comparison. The total speed plots clearly mark the eddy events discussed before and the vertical extent of speeds larger than 40 cm/s which in general are at depths shallower than 400 m. All the middle panels, which depict high frequency speeds, show the impact of hurricane Emily at the end of July. Notice that moorings 2 and 5 show more high frequency fluctuations than mooring 4. Mooring 5 shows an event in April at about 400 m depth. Whether this indicates focusing of surface generated inertial energy (Kunze, 1985, 1986) or the inertial motions are generated by the eddies alone remains to be determined. Observe that besides the high frequency motions generated by hurricane Emily almost all of the energy is subinertial at these depths.

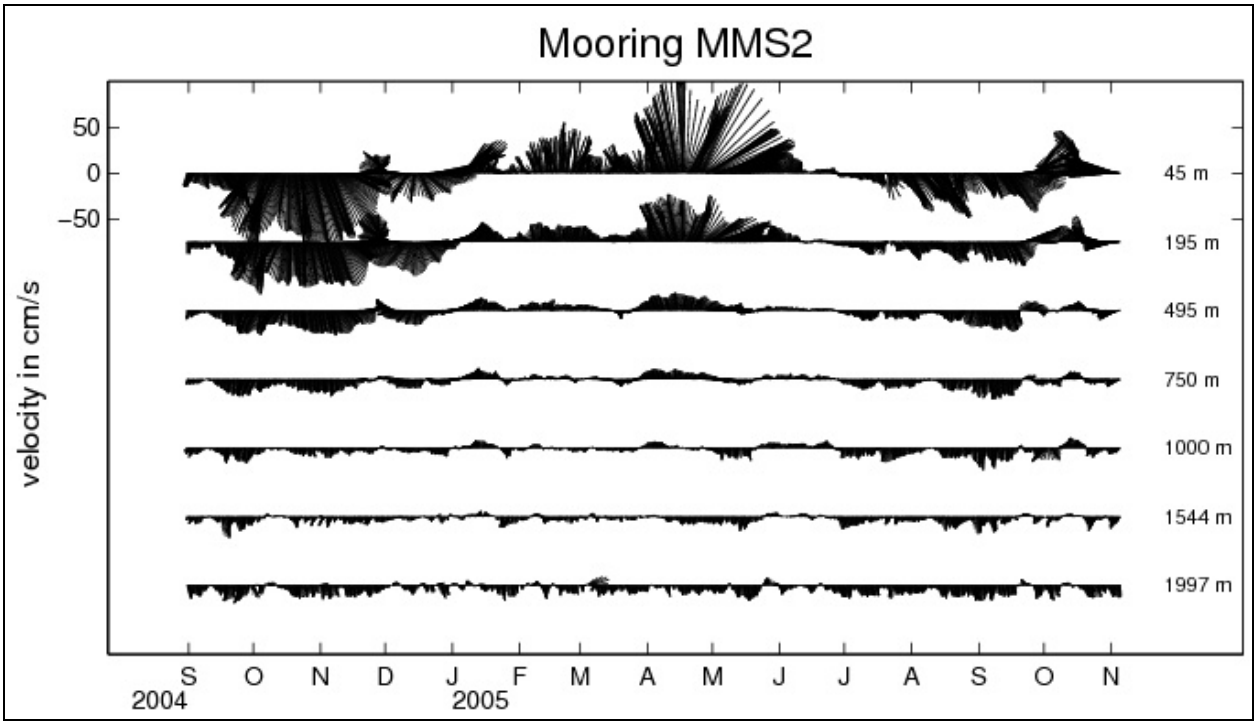

Figure 20. Vector time series of the currents measured over the slope, in 2,000 m of water, in the northwestern Gulf of Mexico, mooring 2.

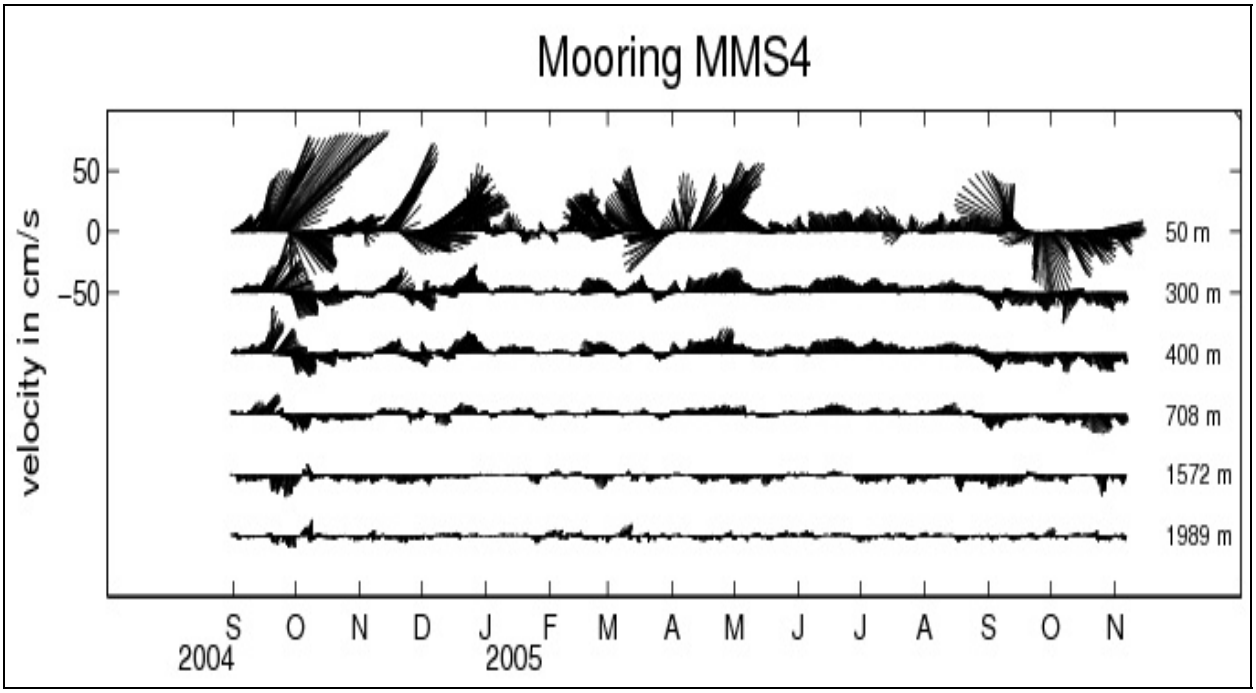

Figure 21. Vector time series of the currents measured over the slope, in 2,000 m of water, in the northwestern Gulf of Mexico, mooring 4.

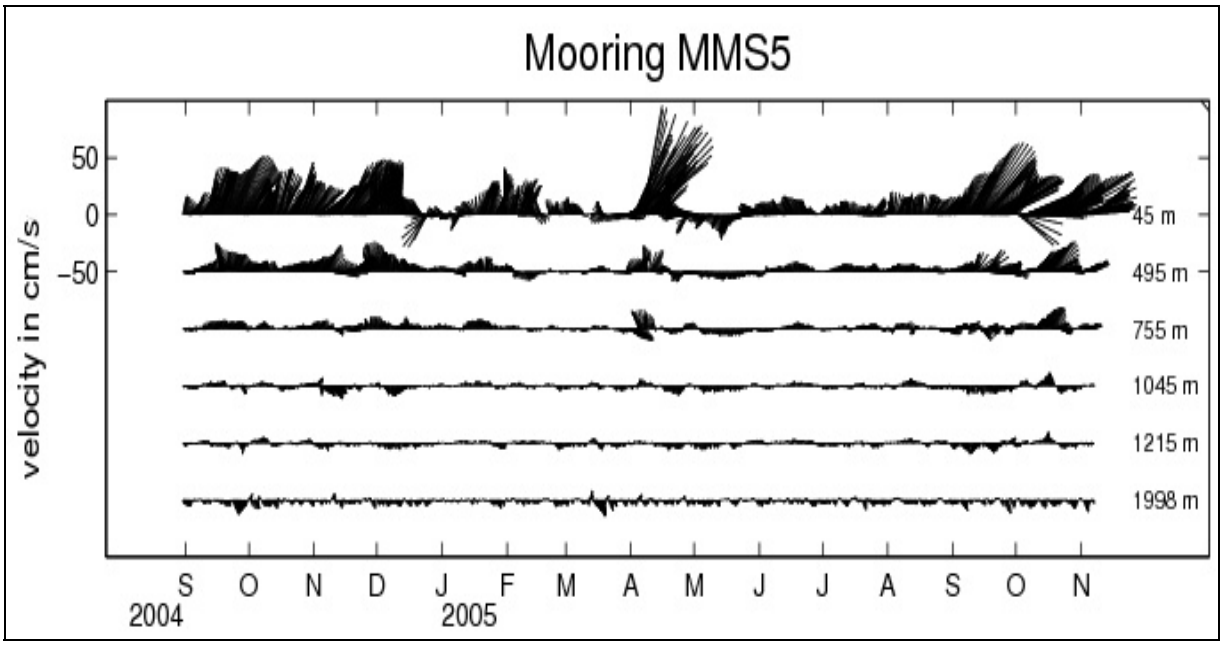

Figure 22. Vector time series of the currents measured over the slope, in 2,000 m of water, in the northwestern Gulf of Mexico, mooring 5.

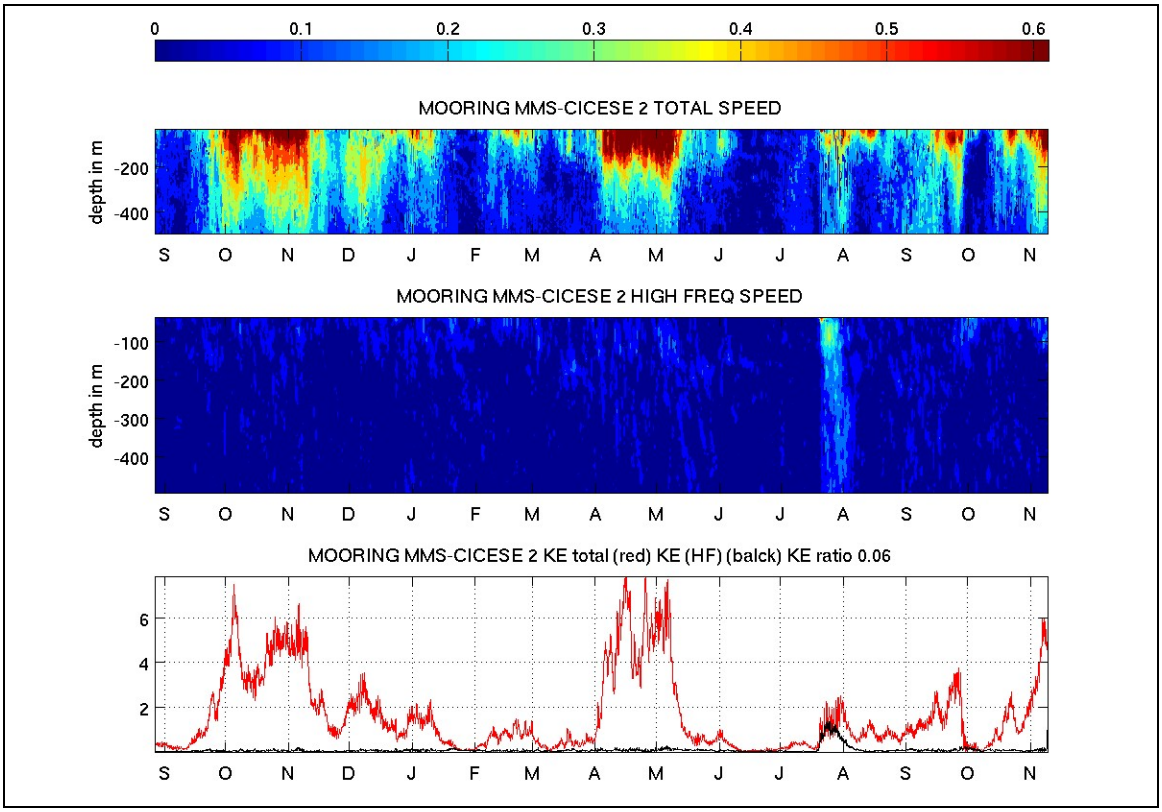

Figure 23. Time series of total speed vs depth (top), speed of high-pass velocity series (middle), and time series of total (red) and high-frequency (black) kinetic energy for mooring MMS2 in the top 400-500 m. Speeds in cm/s and kinetic energy in (m^2/s^2).

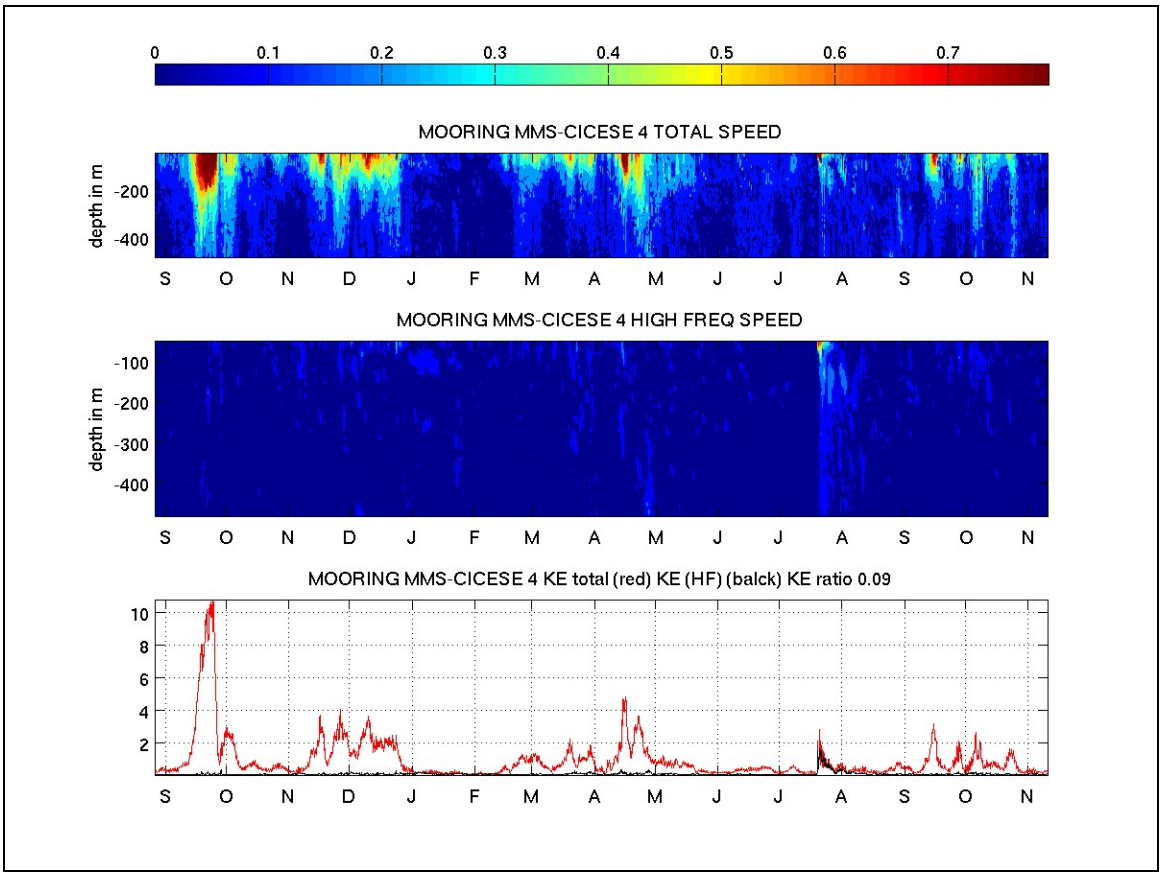

Figure 24. Time series of total speed vs depth (top), speed of high-pass velocity series (middle), and time series of total (red) and high-frequency (black) kinetic energy for mooring MMS4 in the top 400-500 m. Speeds in cm/s and kinetic energy in (m^2/s^2).

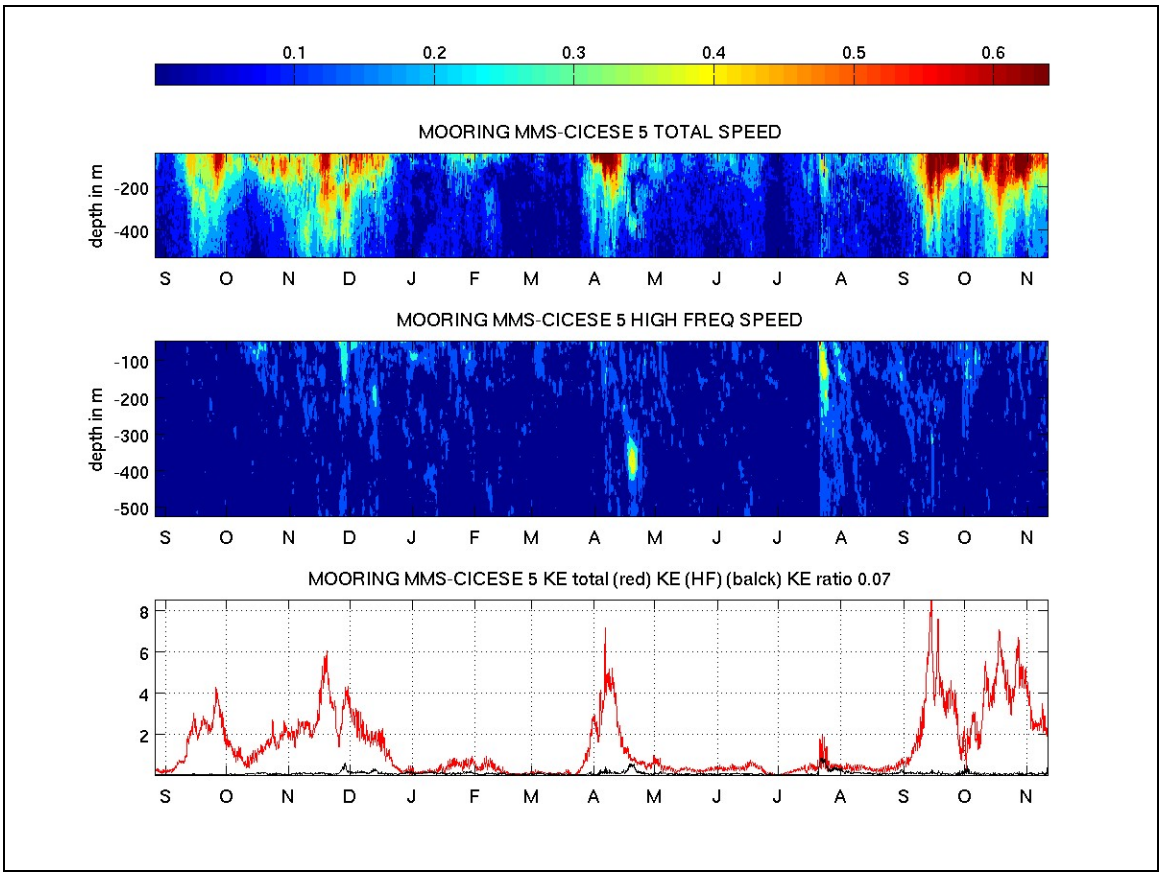

Figure 25. Time series of total speed vs depth (top), speed of high-pass velocity series (middle), and time series of total (red) and high-frequency (black) vertically averaged kinetic energy for mooring MMS5 in the top 400-500 m. Speeds in m/s and kinetic energy in (m^2/s^2).

Figures 26 and 27 show speeds, high frequency speeds and their energy contributions at other depths for moorings 2 and 5, respectively. The feature to notice here is that there appears to be a maximum in the relative contribution of high frequency energy to the total energy at depths between 800 and 1200 m. That can be appreciated looking at the size of the black curve relative to the red curve in the lower panels of Figures 26 and 27. We mentioned this feature already when discussing Figure 6 in Section 3. The other thing worth mentioning is that high frequency energy is present throughout the water column in all moorings. This will clearer below, (Section 5) with the spectral analysis. Figures for mooring 4 are not shown since the mid-depth ADCP instrument (measuring between 700-1200 m depth) failed.

Figures 28, 29, and 30 show standarized times series (i.e. the series are divided by their standard deviation) of of sea surface height anomalies and temperatures for moorings 2, 4, and 5 respectively. In contrast to mooring MMS1 (see Figure 19), temperature variations in the top 800 meters seem to be highly (above 0.5) correlated with sea surface height anomalies. Between 1200-1500 m correlations are low although the sign of the anomalies is generally the same as the temperature anomalies above and those from sea level. Anomalies near the bottom are more mixed, with their sign being opposite to the anomalies above in some cases. Moorings 4 and 5

capture a strong warming signal at depth during the second half of April 2005 consistent with the passage of " re-merged" eddy Ulysses near core region over them (see Figure10).

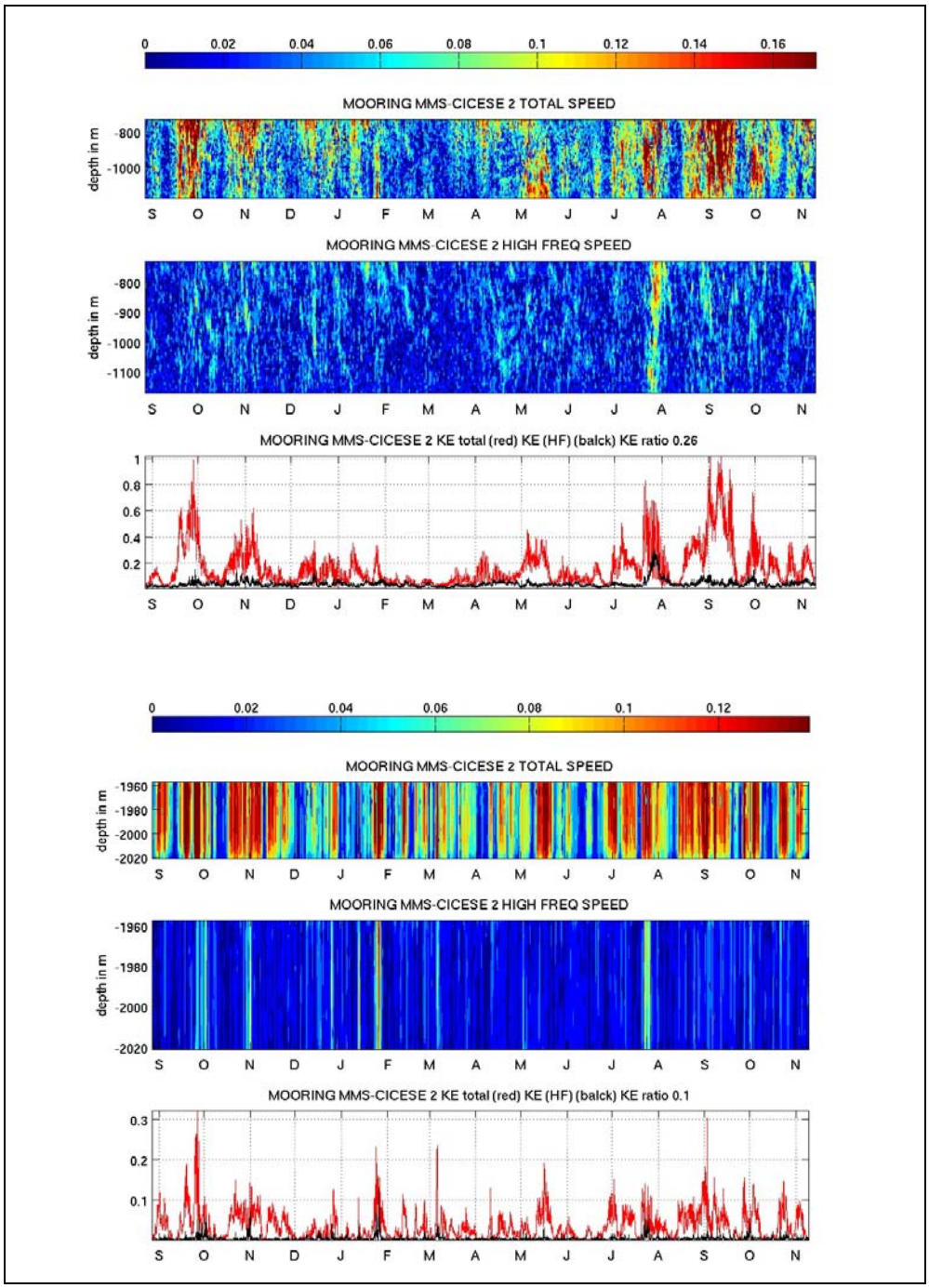

Figure 26. Same as Figure 23 for mid-depths 800-1200 m and near-bottom depths 1960-2020 m in mooring MMS2. Notice the higher contribution of high-frequency motions to the total energy at depths between 800 and 1,200 m for which the KE ratio (high pass KE/total KE) is about 25%.

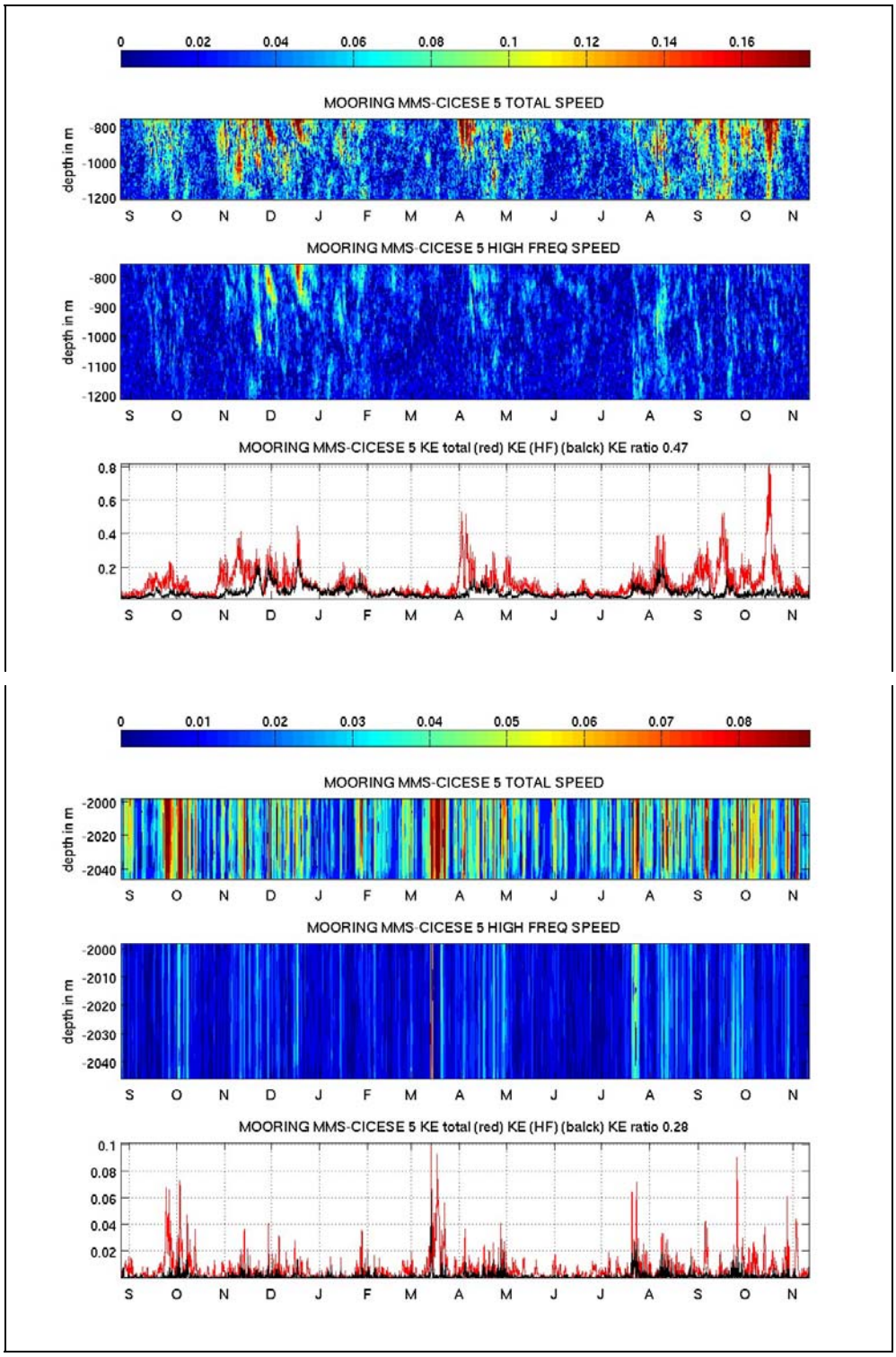

Figure 27. Same as Figure 25 for mid-depths 800-1200 m and near-bottom depths 2000-2050 m in mooring MMS5. Notice the higher contribution of high-frequency motions to the total energy at depths between 800 and 1200 m.

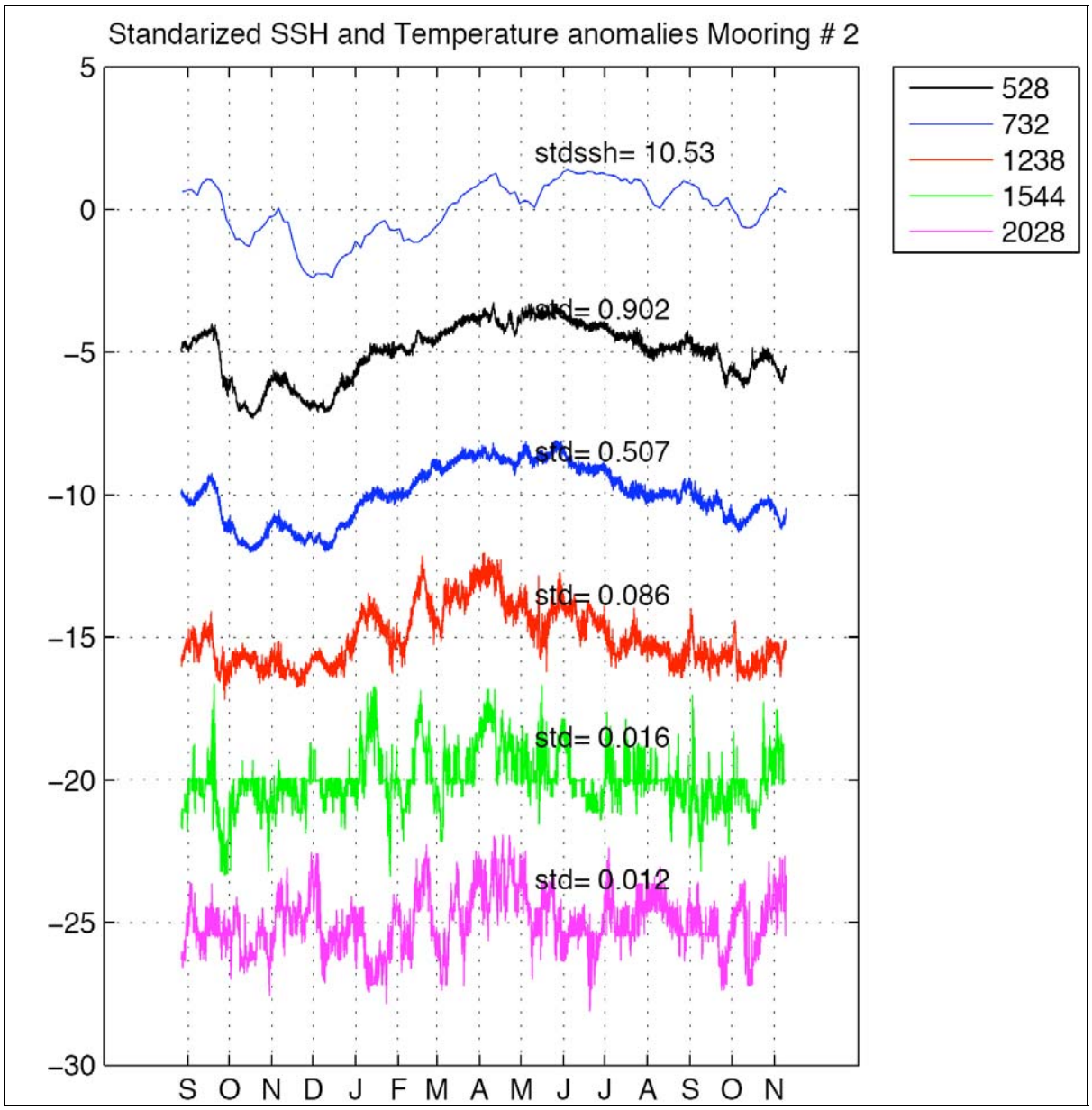

Figure 28. Standardized sea surface height anomalies and temperatures at different depths (indicated by the legend) for mooring MMS1. Series are offset by 5 units to ease visualization and comparison. Standard deviations, in cm for sea surface height and degrees C for temperature, are indicated. Temperature anomalies above 800 m have correlation coefficients with ssh anomalies higher than 0.5.

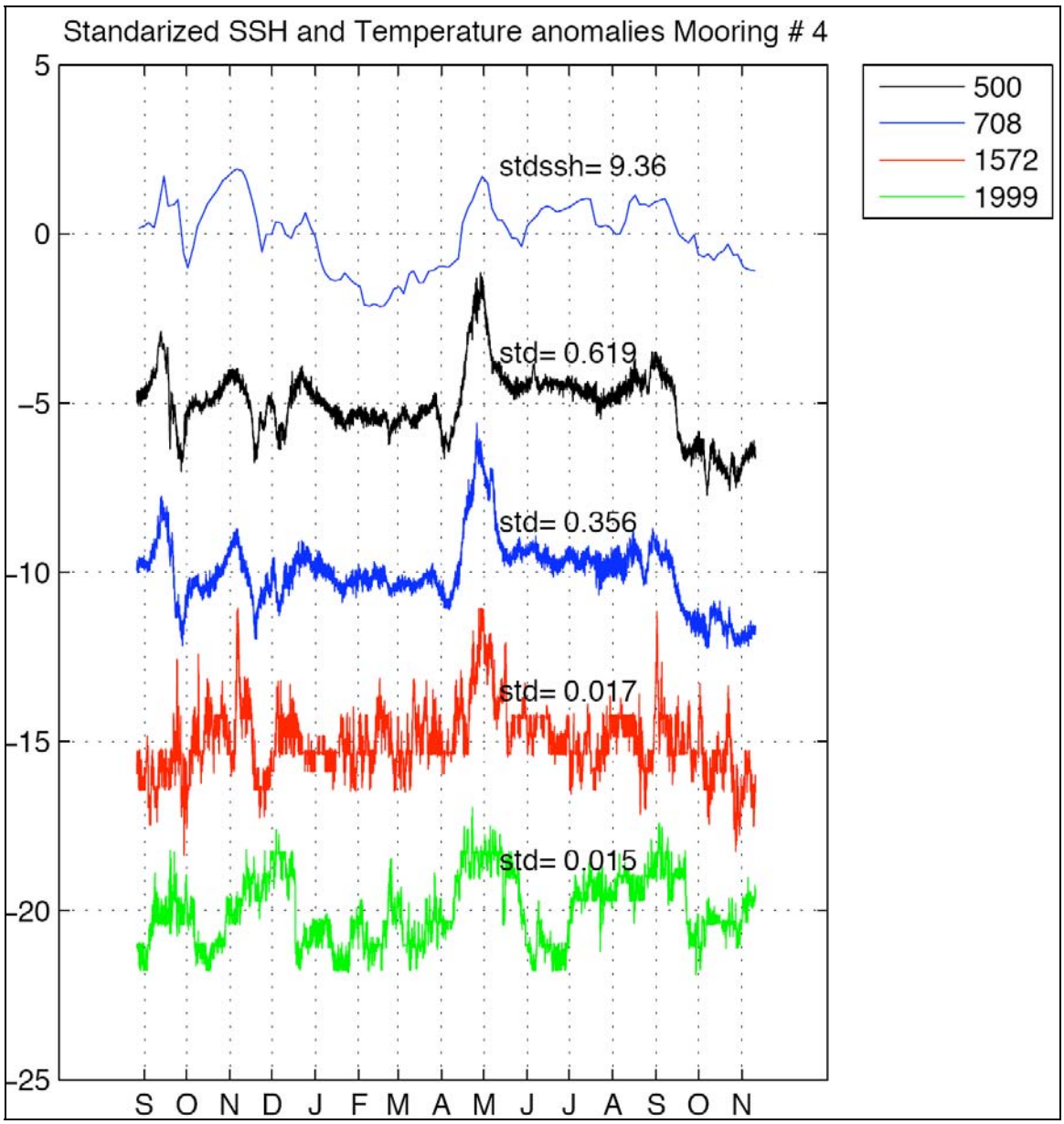

Figure 29. Same as Figure 28 but for mooring MMS4. Notice the strong warming produced by the passage of eddy Ulysses during April 2005, which is absent in mooring 2.

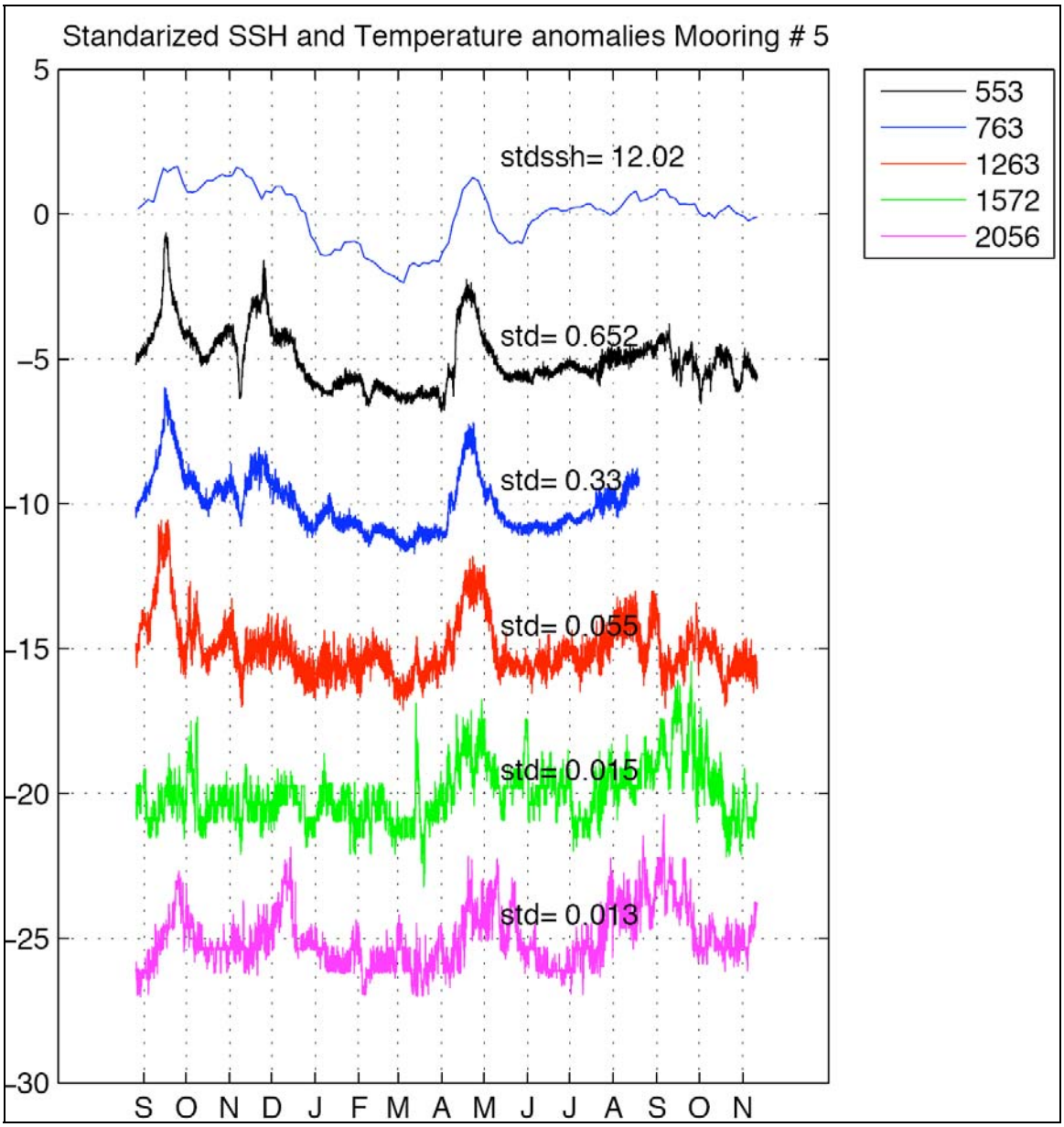

Figure 30. Same as Figure 28 but for mooring 5. Notice the strong warming produced by the passage of eddy Ulysses during April 2005, which is absent in mooring 2.

Figure 31 shows time series of temperature anomalies (blue) and high-pass anomalies (red) at around 750 m and 1250 m on moorings 2 and 5. Besides the increase in high frequency variations associated with hurricane Emily at the end of July, one can see there are other events (e.g. eddy Ulysses in mooring 5 during April) where suprainertial energy increases. Abrupt temperature variations associated with eddies seem to give rise to larger high frequency temperature fluctuations. Notice also that inertial-suprainertial motions related to hurricane Emily appear to last longer at mooring 5 than at mooring 2 at 1250m.

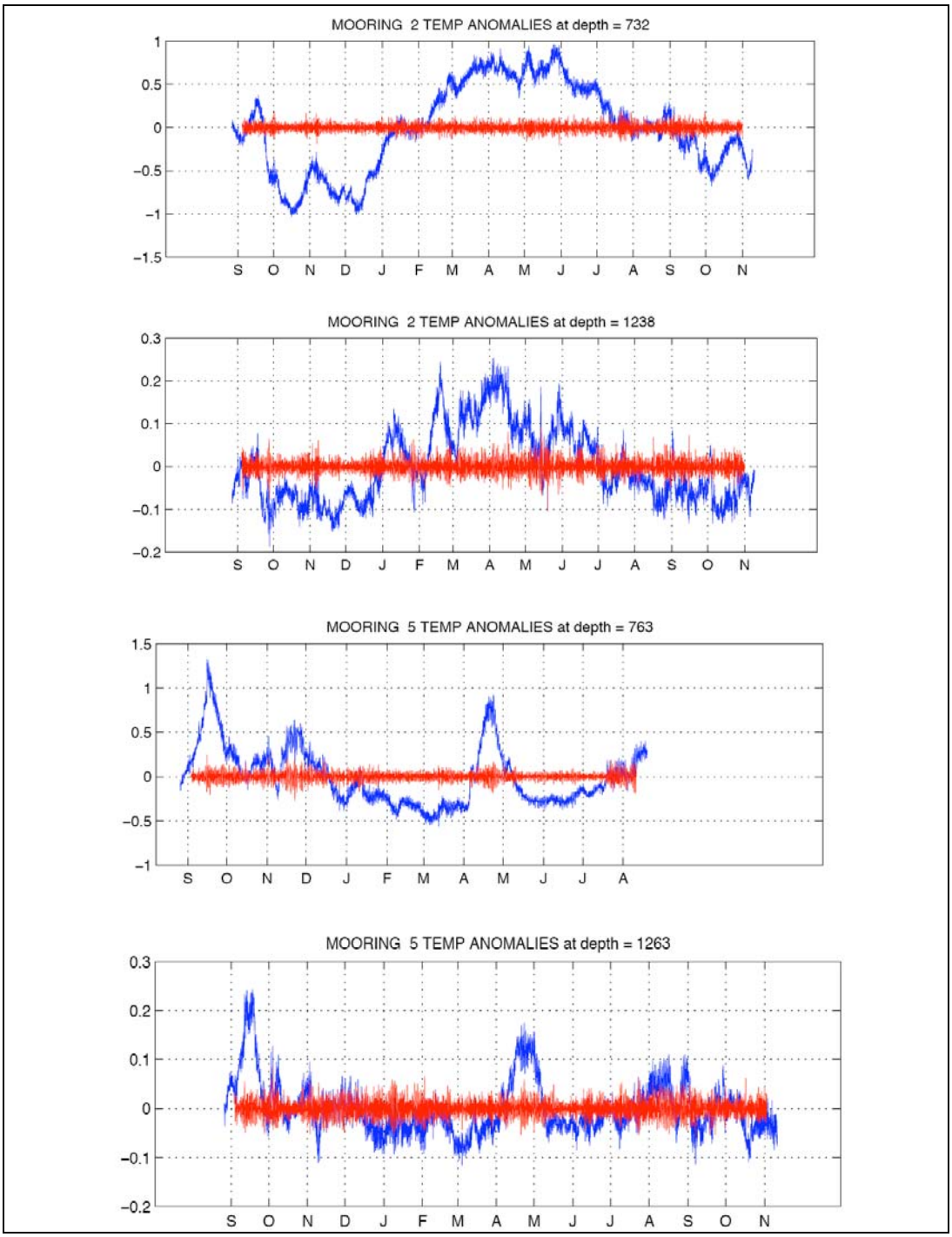

Figure 31. Total (blue) and high-pass (red) temperature anomalies at around 700 and 1,250 m depth at mooring 2 (first two panels) and mooring 5 (lower two panels). Note time series at 700 m on mooring 5 is shorter than the others. Observe high-frequency fluctuations at 1,250 m associated with Hurricane Emily appear to last longer at mooring 5 than at mooring 2. Abrupt temperature changes associated with eddies seem to enhance high-frequency variations.

4.2.3. Abyssal Flow

Finally, mooring MMS3 depicts the current regime offshore, over the deep gulf. Unfortunately the ADCP sampling currents at the near surface (top 500 m) was faulty so the analysis is based on currents below 700 m. Figure 32 shows vector time series for this mooring for comparison with Figures 20, 21, and 22 (all along the slope). First thing one notices is that currents are much more coherent in the vertical than the ones along the slope. The other obvious feature is the absence of the persistent southward flow near the bottom. Another singular event occurred in March of that year, when a strong, bottom-intensified, southerly current was present from 787 m to the bottom, and caused the mooring to sink by more than 70 m, the largest event of that kind during the period of measurements. To relate the mooring observations with eddy features it is interesting to compare them with the surface geostrophic flow obtained from altimetry data which is shown in Figure 33. During September-October there is consistency throughout the water column between the surface geostrophic flow and the deeper mooring velocities. Figure 9 shows cyclone C1 moving to the west at that time, so the mooring samples the western branch of C1 during September and its eastern branch during October. During November and December, the surface flow shows the signature of eddy Ulysses over the mooring and the flow rotating clockwise. In early November, the deeper flow is quite weak to the north above 1000 m and to the south below that depth. As time progresses, the flow rotates anticyclonically. At the end of December, southeastward flow is seen at 700 m rotating clockwise with depth while the flow at the surface is to the northeast. The rapid changes in flow direction in early February 2005, seen both at the surface and at the deeper mooring currents signal the interaction between cyclone C1-C2 and UlyssesN eddies, with the flow going from northeast to northwest very rapidly. In March the bottom intensified event occurs with currents rotating clockwise (south-southwest) while at the surface the flow goes northwest-northeast. In the period April-May-June the flow is similar in the whole water column. This is the period where “re-merged” eddy Ulysses is over the whole mooring array. The rapid changes seen during early May signal the rapid rotation of this eddy (see Figure 11). From July to the end of September the surface flow is determined by a cyclonic feature (C5) and the flow rotates southwest-southeast. Meanwhile the deeper flow during this period is basically to the northwest until the end of September when it starts rotating clockwise. October signals the arrival of eddy Vortex. Surface geostrophic flow and mooring currents coincide at the beginning and end of the month with flow going north then north-west whilst in the middle of the month the deep flow is to the southeast. Note that the flow at a point may rotate cyclonically even when an anticyclone is present due to the orientation of the eddy.

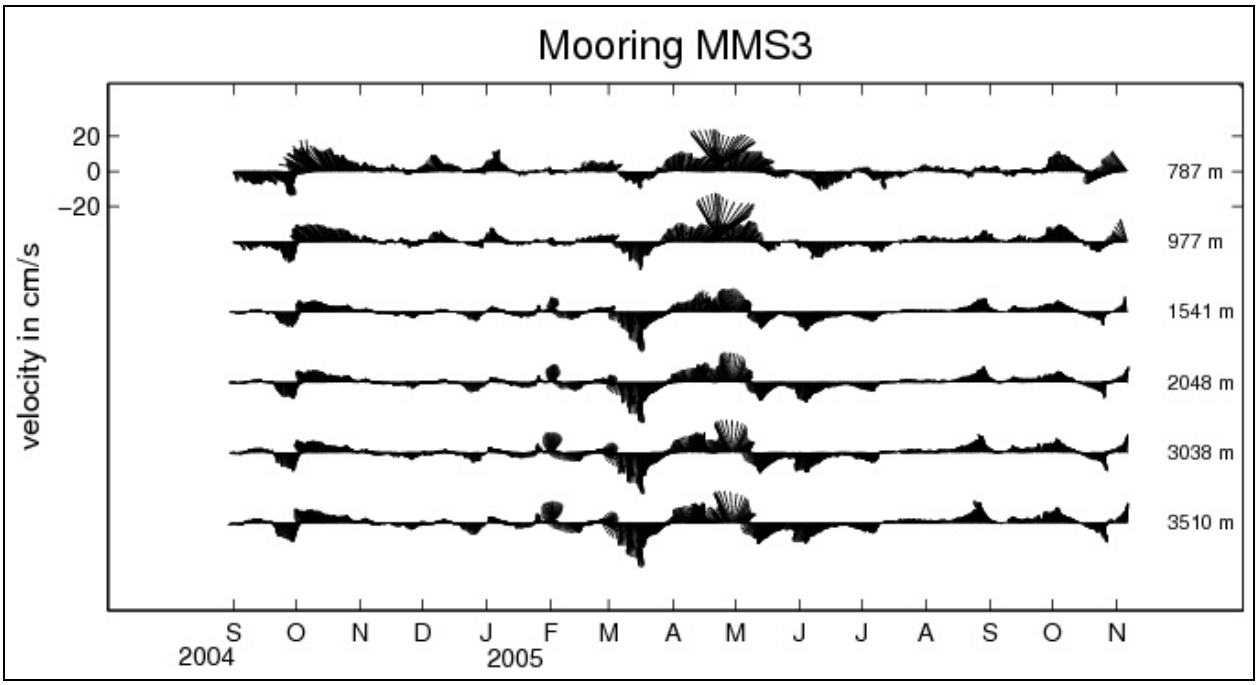

Figure 32. Vector time series from mooring 3, located at the abyssal GoM at 3,500 m.

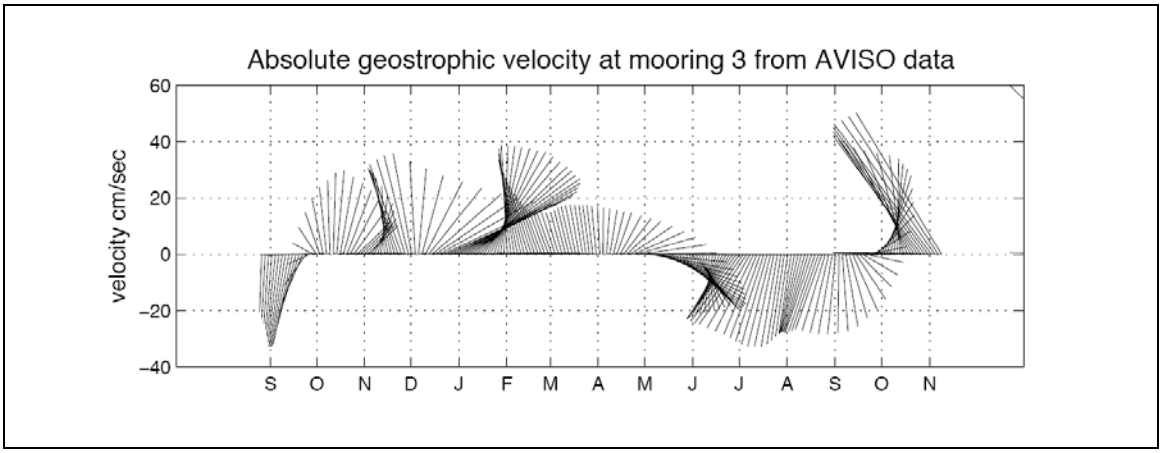

Figure 33. Absolute geostrophic velocity interpolated from AVISO data to the mooring 3 position. For comparison with Figure 32 since the mooring lacks near-surface measurements.

Figure 34 is similar to Figures 26 and 27, and shows time series of total speed (top panel), high-pass speeds (middle panel) and total (vertically integrated) kinetic energy (red) and high-pass kinetic energy (black) on mooring 3. Similar to the results in moorings 2 and 5 (Figures 26 and 27) the relative contribution of high-frequency motions to the total energy is larger in the 800-1200 m depth. We see again the signature of hurricane Emily, though this time in the very last days o July and first couple of days of August. Besides hurricane Emily one sees again an increase in high frequency energy during the winter season probably associated with northern wind events and during April when there is a strong warming in the water column associated with eddy Ulysses and a northern event (see Figure 35 below and Figure 18).

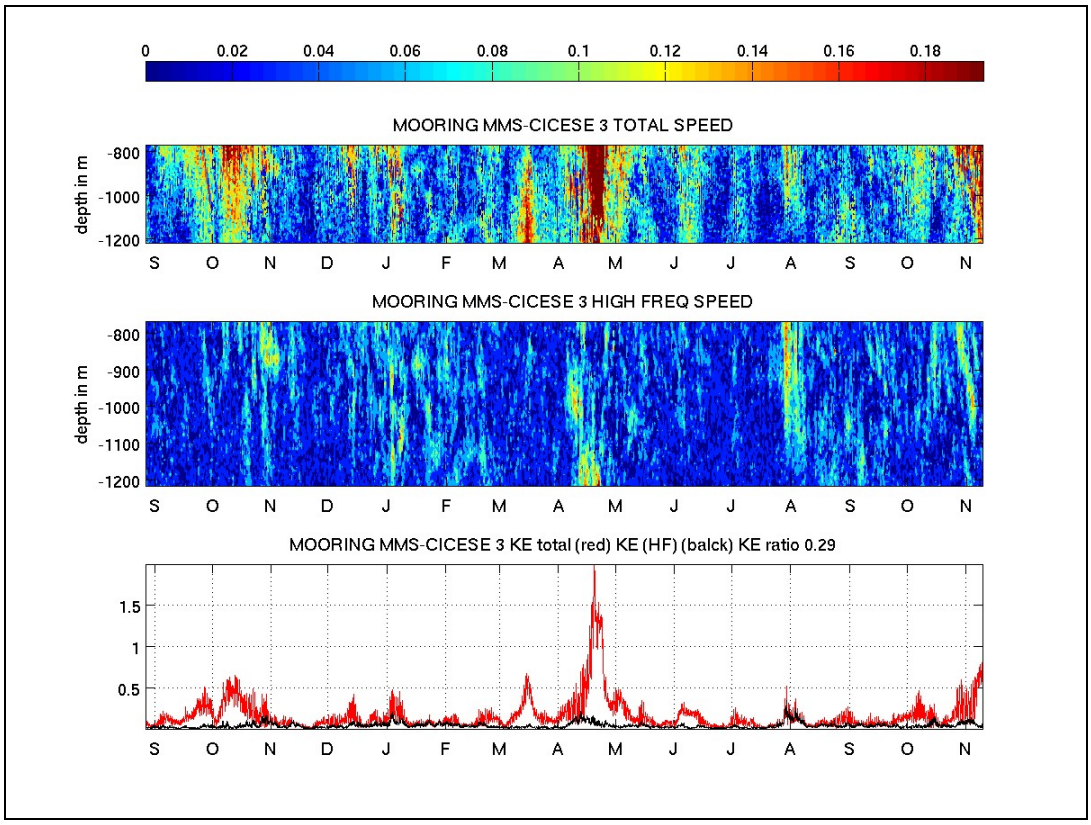

Figure 34. Time series of total speed vs depth (top), speed of high-pass velocity series (middle), and time series of total (red) and high-frequency (black) vertically averaged kinetic energy for mooring MMS3 in the 800-1,200 m range and near the bottom (3,500-3,600 m). Speeds in m/s and vertically averaged kinetic energy in (m^2/s^2). Note the higher relative contribution of high-pass motions to total kinetic energy in the 800-1,200 m range, similar to moorings 2, 4, and 5 along the slope, given by the total KE ratio (high-pass KE /total KE vertically and time integrated).

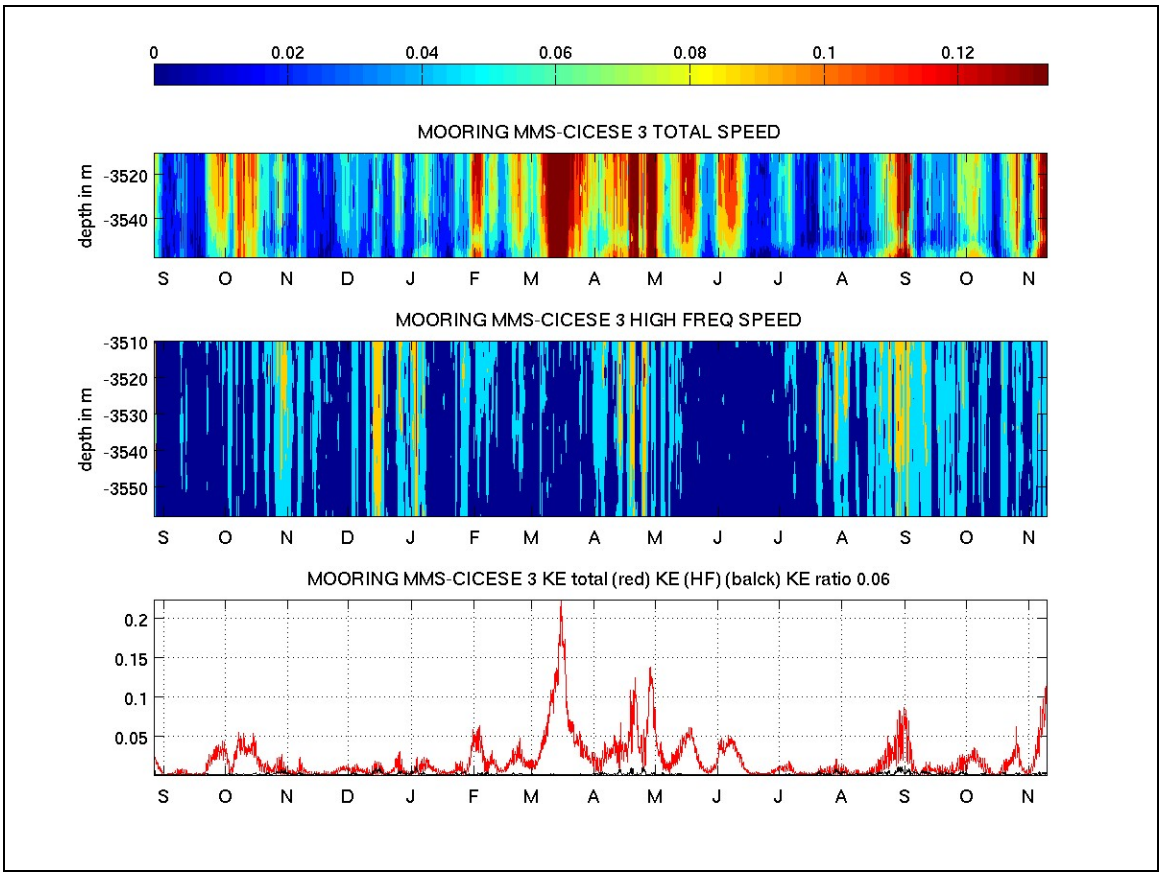

Figure 34. Time series of total speed vs depth (top), speed of high-pass velocity series (middle), and time series of total (red) and high-frequency (black) vertically averaged kinetic energy for mooring MMS3 in the 800-1,200 m range and near the bottom (3,500-3,600 m). Speeds in m/s and vertically averaged kinetic energy in (m^2/s^2). Note the higher relative contribution of high-pass motions to total kinetic energy in the 800-1,200 m range, similar to moorings 2, 4, and 5 along the slope, given by the total KE ratio (high-pass KE /total KE vertically and time integrated) (continued).

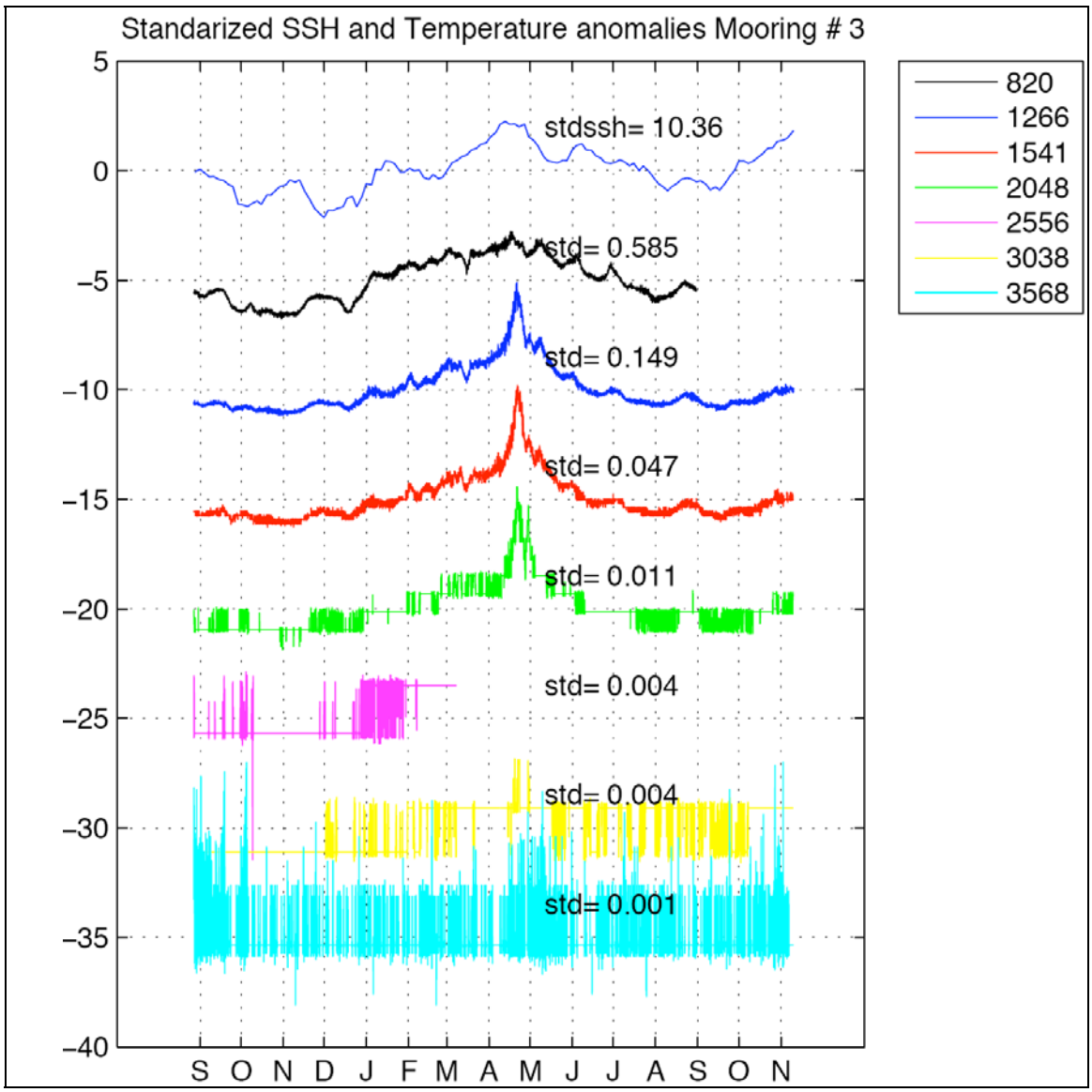

Figure 35. Standardized sea surface height anomalies and temperatures at different depths (indicated by the legend) for mooring 3. Series are offset by 5 units to ease visualization and comparison. Standard deviations, in cm for sea surface height and degrees C for temperatures, are provided to estimate actual variations. Notice the strong warming at the end of April associated with "re-merged" eddy Ulysses.

Figure 35 shows standardized sea surface height anomalies and temperature anomalies at different depths (indicated by the legend). Series are offset 5 units to ease comparison. The main feature in this plot is the strong warming that occurs at the end of April 2005 in the 1200-2000 m depth, although the signal can be detected all the way to the bottom at 3600 m. Comparing mooring 3 with moorings 4 and 5 over the slope (Figures 29 and 30) we see that, relative to its overall variance, the warming in mooring 3 at 800 m -and probably above that level too- is not as strong as the warming at deeper levels, whereas in moorings 4 and 5 the relative warming is

similar in the 1500-500 m range. In absolute terms, the warming at 800 m is about 1.5 degrees whereas below it is of about 0.7 and 0.25 degrees at 1200 m and 1500 m respectively. The event, we repeat, is related to the presence of eddy Ulysses over the mooring. Correlation coefficients between ssh anomalies and temperature anomalies is higher than 0.7 in the top 4 instruments (from 800 to 2000 m). Hence cold (warm) anomalies do indicate the presence of cyclones (anticyclones).

To determine when high frequency temperature fluctuations enhance, the next figure shows full (blue) and high-pass (red) temperature anomalies at 1200 and 2000 m depth. Besides the strong high-frequency event during April, notice that there is no clear enhancement of high-pass temperature variations associated with hurricane Emily as it occurs in moorings 2 and 5 (see Figure 31). Although there too, the effect of the hurricane is clearer in the velocity data rather than the temperature data. Overall, comparing Figure 36 with Figure 31, there seems to be less high-pass temperature variations at depth in mooring 3 than in moorings 2, 4, and 5.

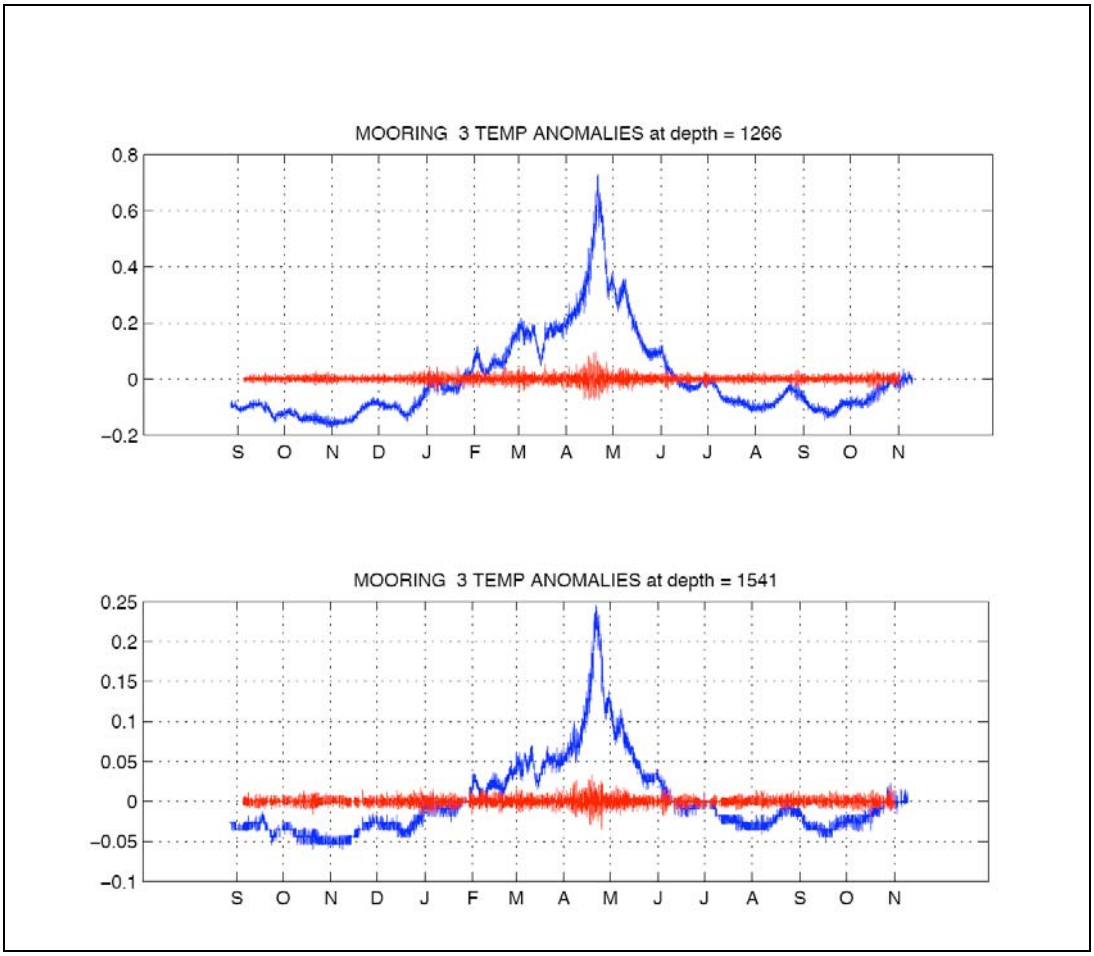

Figure 36. Total temperature anomalies (blue) and high-pass anomalies (red) at around 1,200 m and 1,550 m depth. Note the increase of high-frequency fluctuations in the middle of April 2005.

5. SPECTRAL CHARACTERISTICS OF THE VARIABILITY

To dissect and quantify the spectral content and structure of the variability described in the previous section, we first carry out rotary spectral analysis of the velocity vector time series and spectral analysis of the temperature data. The spatial structure of the variability is studied using Empirical Orthogonal Function analysis in Section 6.

Rotary cross spectra (Mooers, 1973, Gonella, 1972) are calculated between current observations at the same depth on different moorings and between different depths at the same mooring. Besides the spectral density at positive and negative frequencies the following plots also show internal coherence square, that relate components rotating in the same sense on the current series being analyzed, and their phase relation, with negative phase for positive frequencies and positive phase for negative frequencies indicating that the input series leads the output series by that phase amount.

Figure 37 shows cross spectra, between two adjacent moorings MMS1 and MMS2 at 50, 250 and 400 m. Only at 50 m there is some coherence of motions around the inertial frequency, which is lost at depth since the inertial energy decreases rapidly with depth on the shallow mooring (MMS1) where there is not a discernible inertial peak at the 400 m depth. The vector cross spectra analysis shows little coherence in the across shore directions at all depths. Also cross spectra between mooring MMS2 and MMS3 at depths of 850, 1350 and 1950 m depth, in the across shelf direction, do not show significant coherence at any of the resolved frequency bands (Figure 38).

In the along 2000 m isobath direction there is significant coherence of currents only at the 1/20 cpd band between moorings MMS2 and MMS5 at depths between 1150 to 1750 m (Figure 39). The associated phase for this frequency band, ~25 degrees for the negative frequency and ~-30 degrees for the positive frequency, indicate a signal propagating from mooring MMS2 to mooring MMS5, cyclonically around the gulf, with a phase speed of about 1.7 m/s, which is quite plausible for an internal Kelvin wave propagating around the gulf. Interestingly, Candela *et al* (2003), when analyzing the transports through Yucatan Channel, with direct observations and numerical model simulations, found that both observations and models gave a significant coherence only at the 1/20 cpd band when calculating the cross-spectra between the transports above and below the 6 ^{0}C isotherm, which they interpreted as possibly the signal of a first baroclinic Kelvin wave traveling cyclonically around the gulf trapped to the slope.

There is significant coherence of currents at subinertial frequencies below 760 meters on the deep mooring MMS3 (Figure 40), which was installed at a depth around 3550 m (Figure 3). This aspect is also evident on the subinertial EOFs calculated for this mooring and discussed in the following section. An interesting feature of the spectra calculated at all depths on the deep moorings (>2000 m) is the evidence of a distinguishable inertial peak.

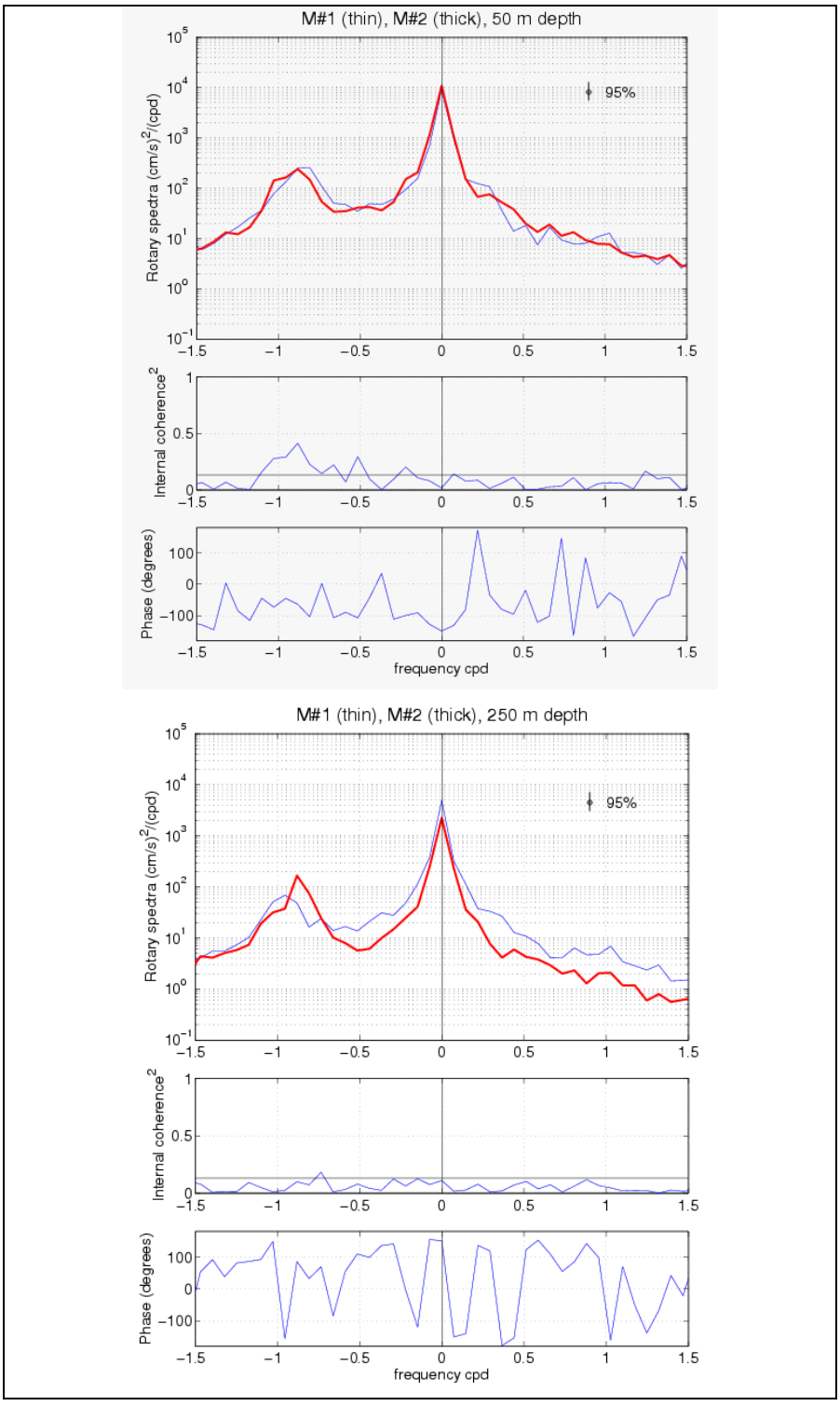

Figure 37. Rotary spectra, internal coherence, and phase between currents measured at 50, 250, and 400 m on moorings MMS1 and MMS2.

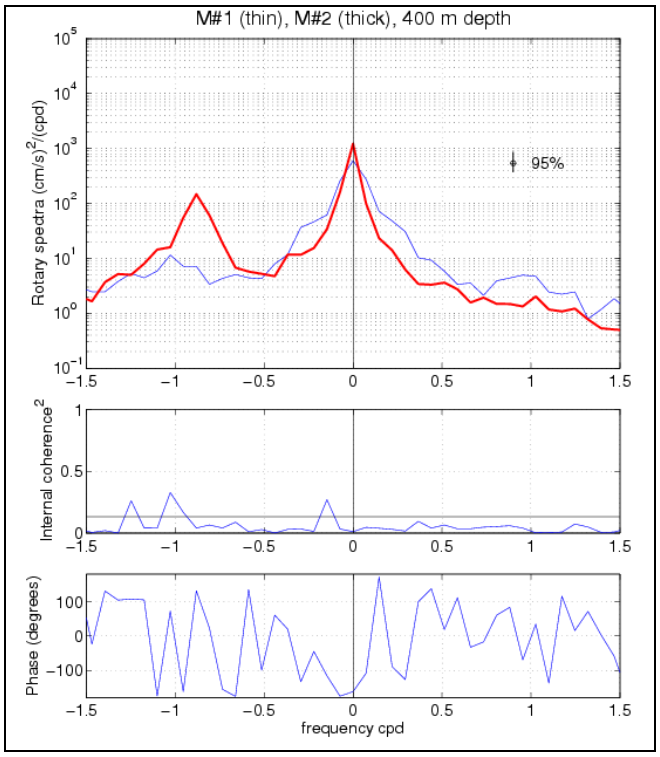

Figure 37. Rotary spectra, internal coherence, and phase between currents measured at 50, 250, and 400 m on moorings MMS1 and MMS2 (continued).

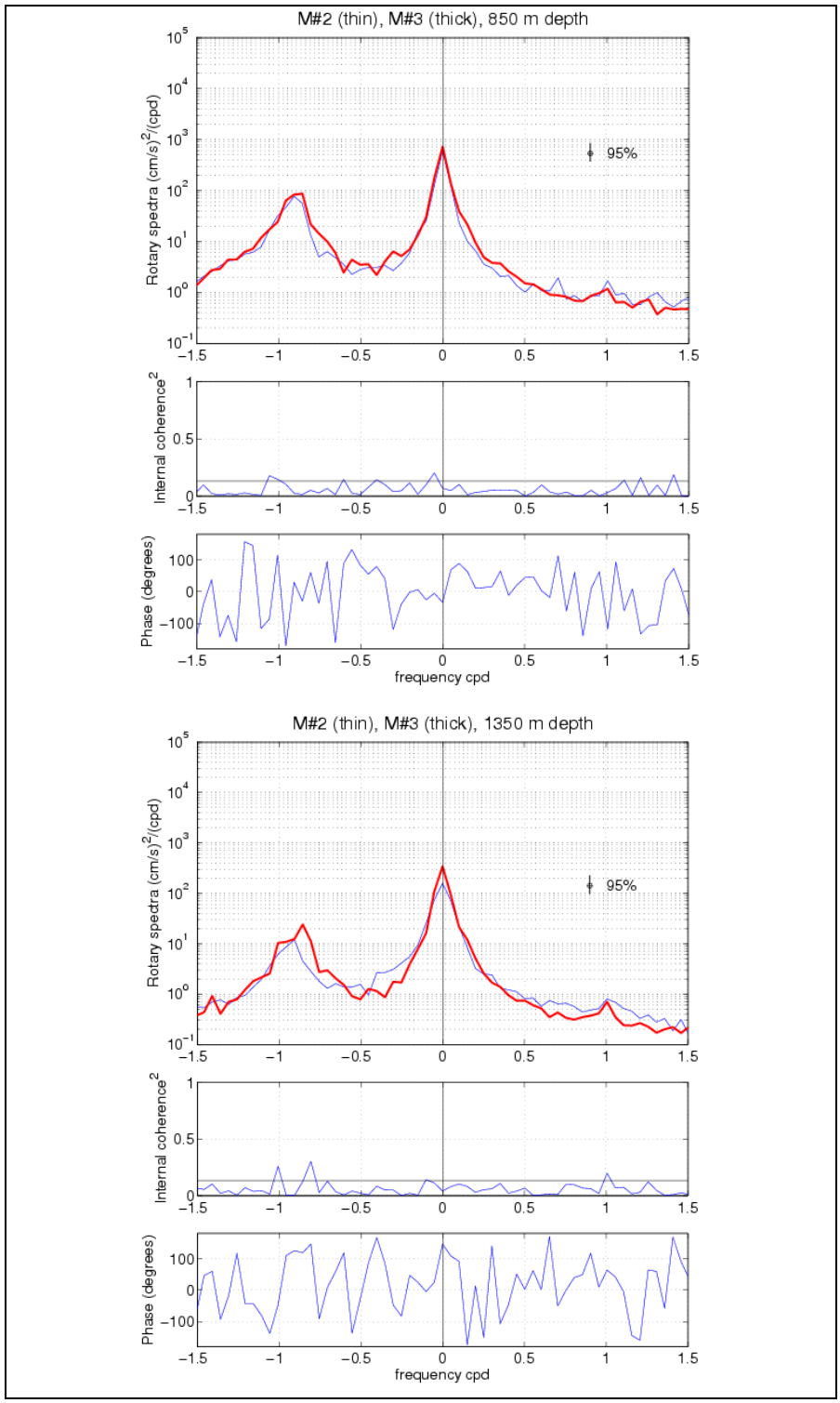

Figure 38. Rotary spectra, internal coherence, and phase between currents measured at 850, 1,350, and 1,950 m on moorings MMS2 and MMS3.

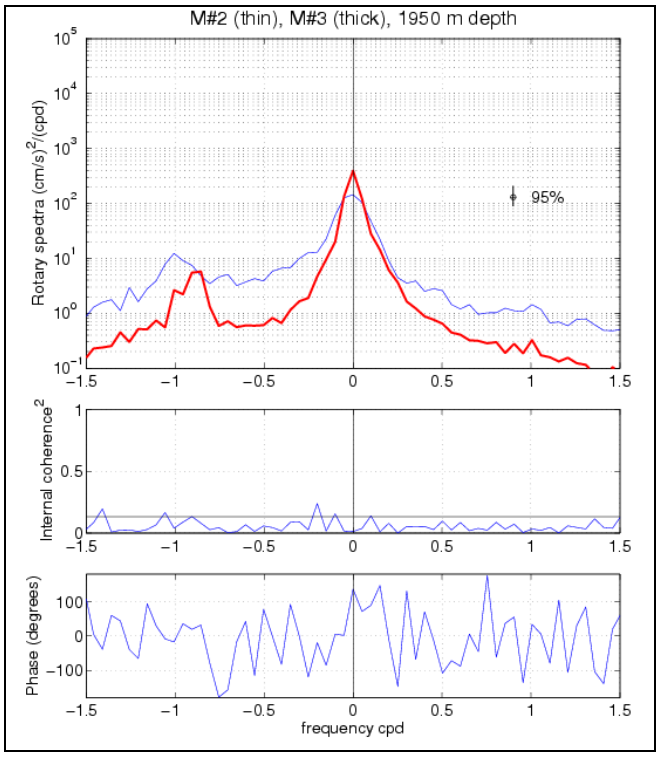

Figure 38. Rotary spectra, internal coherence, and phase between currents measured at 850, 1,350, and 1,950 m on moorings MMS2 and MMS3 (continued).

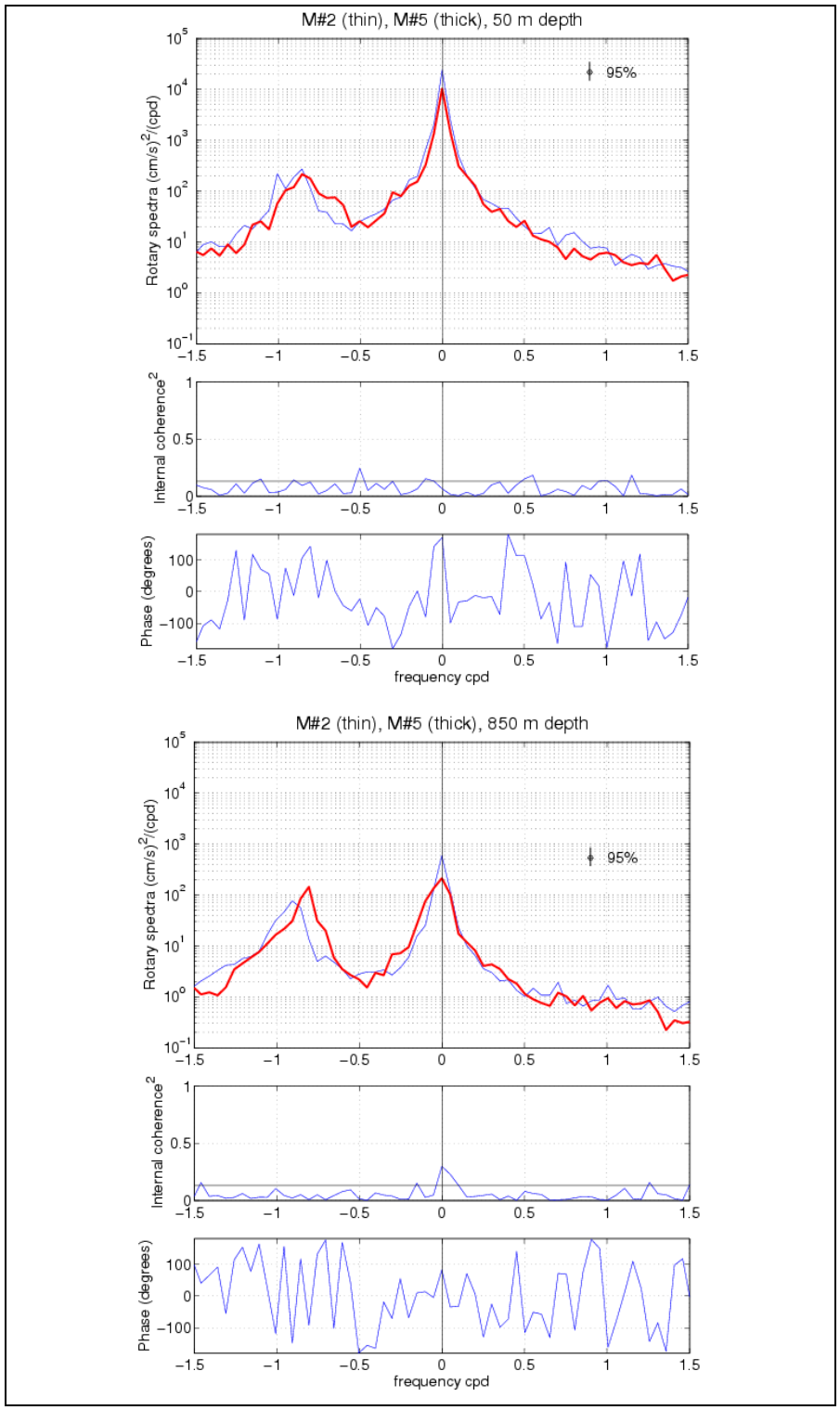

Figure 39. Rotary spectra, internal coherence, and phase between currents measured at 50, 850, 1,350, and 1,950 m on moorings MMS2 and MMS5.

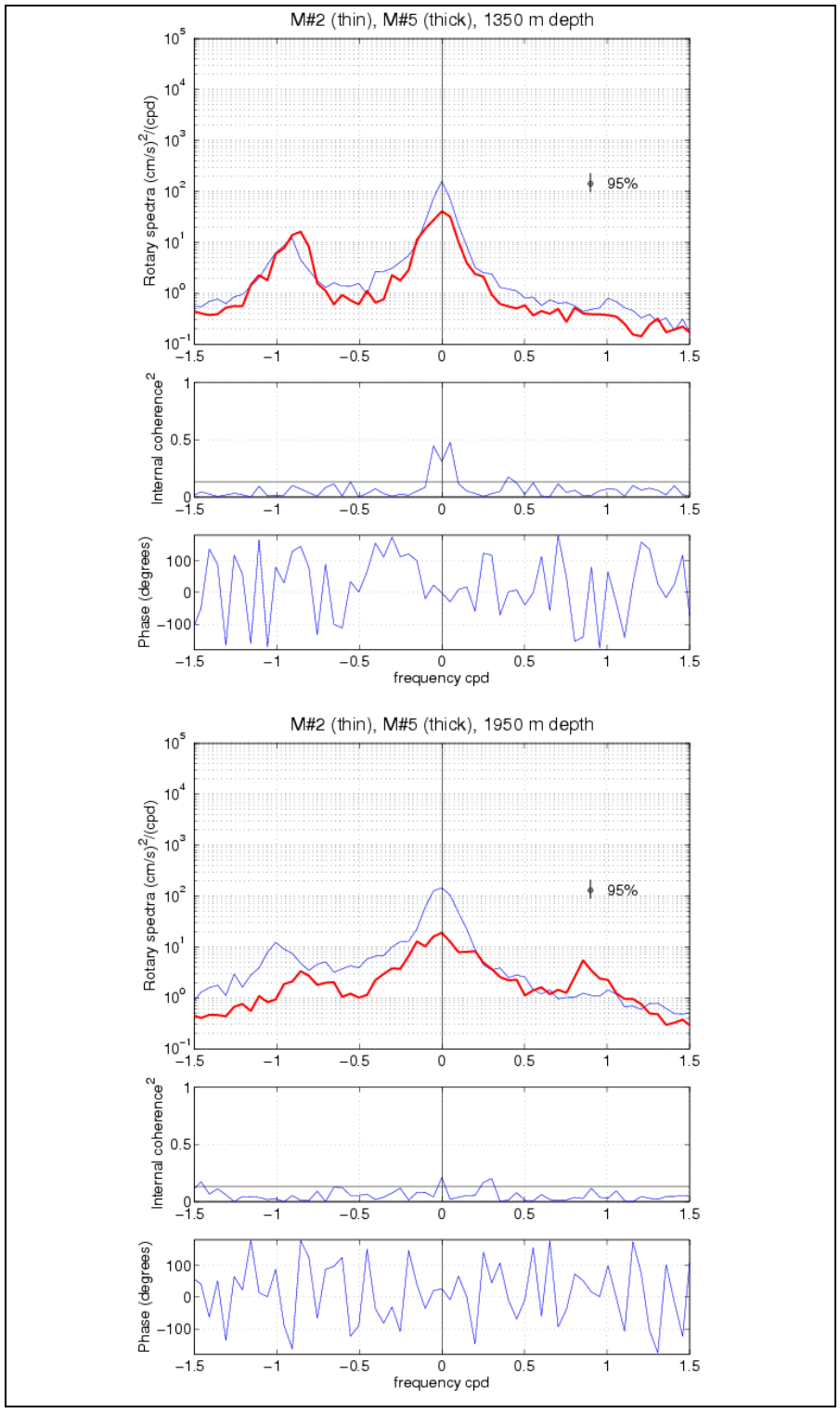

Figure 39. Rotary spectra, internal coherence, and phase between currents measured at 50, 850, 1,350, and 1,950 m on moorings MMS2 and MMS5 (continued).

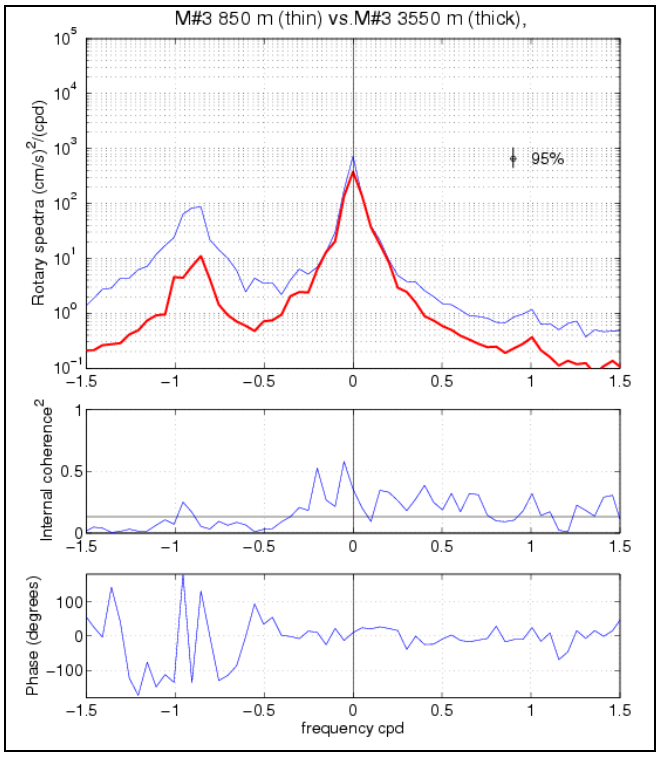

Figure 40. Rotary spectra, internal coherence, and phase between currents measured at 850 and 3,550 m on mooring MMS3.

6. EMPIRICAL ORTHOGONAL FUNCTION ANALYSIS

Using Empirical Orthogonal Function (EOF) analysis of the currents in each mooring, one can decompose the variance of the currents into vertically coherent patterns that can help simplify understanding the behavior of the variability observed on each mooring.

Depending on the degree of polarization of the current data being analyzed one can either arrange the data along independent components (zonal and meridional), maintaining the analysis in the real domain, or combine the horizontal currents into a complex vector. For the case when the observed currents are not well polarized, the complex arrangement usually results in a more compact and clear representation of the patterns. In our present case, the variability ellipses along each mooring, shown in Figure 8, indicate that in most of the water column the currents are quite circular in nature not showing a strong polarization or a well defined direction of variability. Therefore, a complex EOF analysis is preferable. Also to evenly weight current observations in the vertical and to take into account the longest measurement interval, currents were linearly interpolated to nominal depths using only the longest common time series in each mooring.

The first two modes of the subinertial currents are shown in Figures 41-45. The first mode usually represents more than about 80% of the variability of the currents in the vertical profile at each mooring, showing a surface intensified structure at all moorings except at the deep mooring MMS3 where there are no measurements above 760 m (Figure 43). The first mode at this mooring, which represents 90% of the variability, presents a uniform vertical profile from 760m to the bottom. The second modes on all moorings represent around 10% of the variability and show, by orthogonality requirements of the method, a structure resembling a first baroclinic mode. An interesting aspect is that the subinertial EOF modes, in all of the 5 moorings, do not reflect a clear signal of the passage of hurricane Emily over the mooring array.

The first two modes of the suprainertial currents are shown in Figures 46-50. Between the two modes around 50% of the suprainertial variability is taken account for. The spatial vertical structure is quite complicated for the two modes. Contrary to the subinertial modes, what is clear at all locations, is the fact that the suprainertial variability increases both whenever there is a strong atmospheric event, like the passage of hurricane Emily over the mooring array on the 19 and 20 of July 2005, or strong "Norte" events during the winter season, due to excitation of inertial motions (Pollard 1970), but also when Loop Current associated eddies (or their remains) are in the vicinity of the mooring location, like the presence of eddy Ulysses on April 2005, that also excite inertial like motions in the water column.

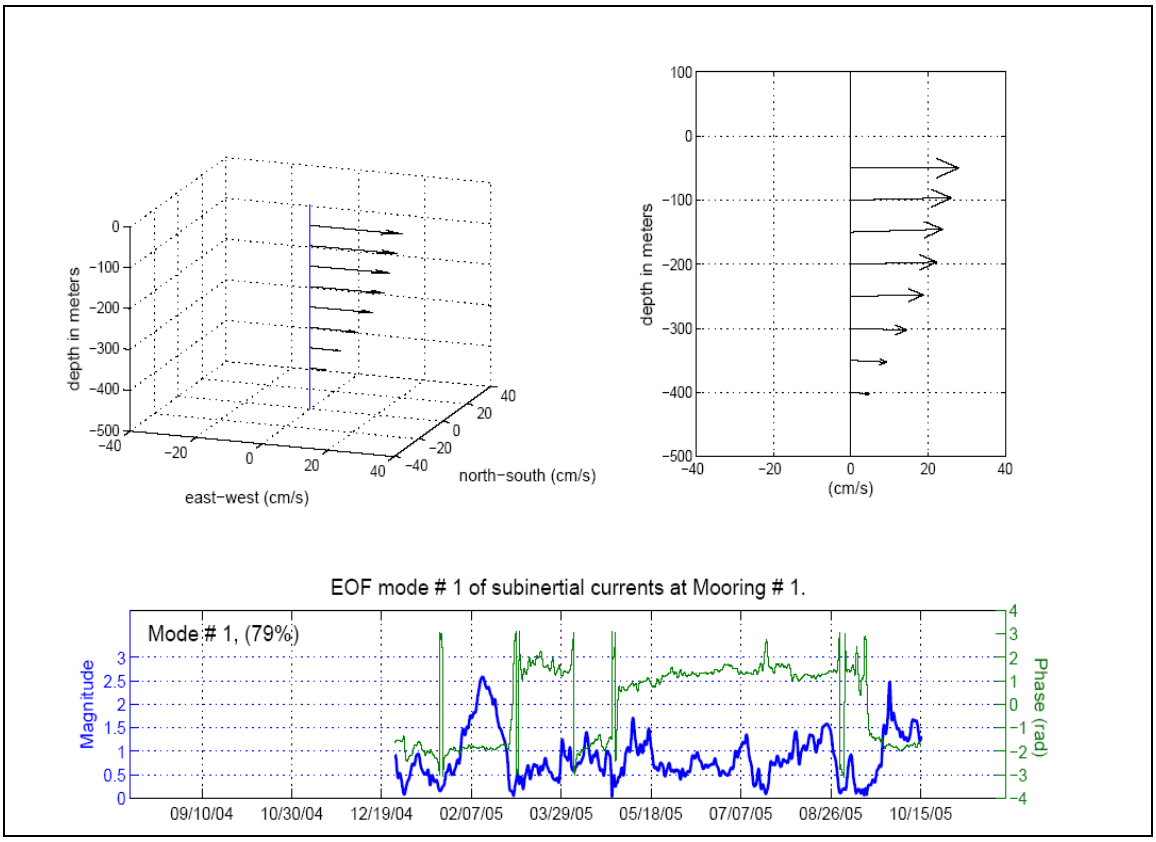

Figure 41. First two EOF complex modes for the observed subinertial current interpolated at regularly spaced vertical levels on mooring MMS1. The upper two panels show the dimensioned spatial structure of the mode in two equivalent representations, on the left, vectors in 3-D space, and on the right, vectors in 2-D with the north-south/east-west component in the abscissa/ordinate directions and each vector starting at its corresponding depth. The lower panel shows the time series (also called principal components) of the mode. Since the EOFs are for a complex time series, i.e. u+i*v, both the spatial structure and principal components are complex and here presented with the time evolution of its magnitude and phase.

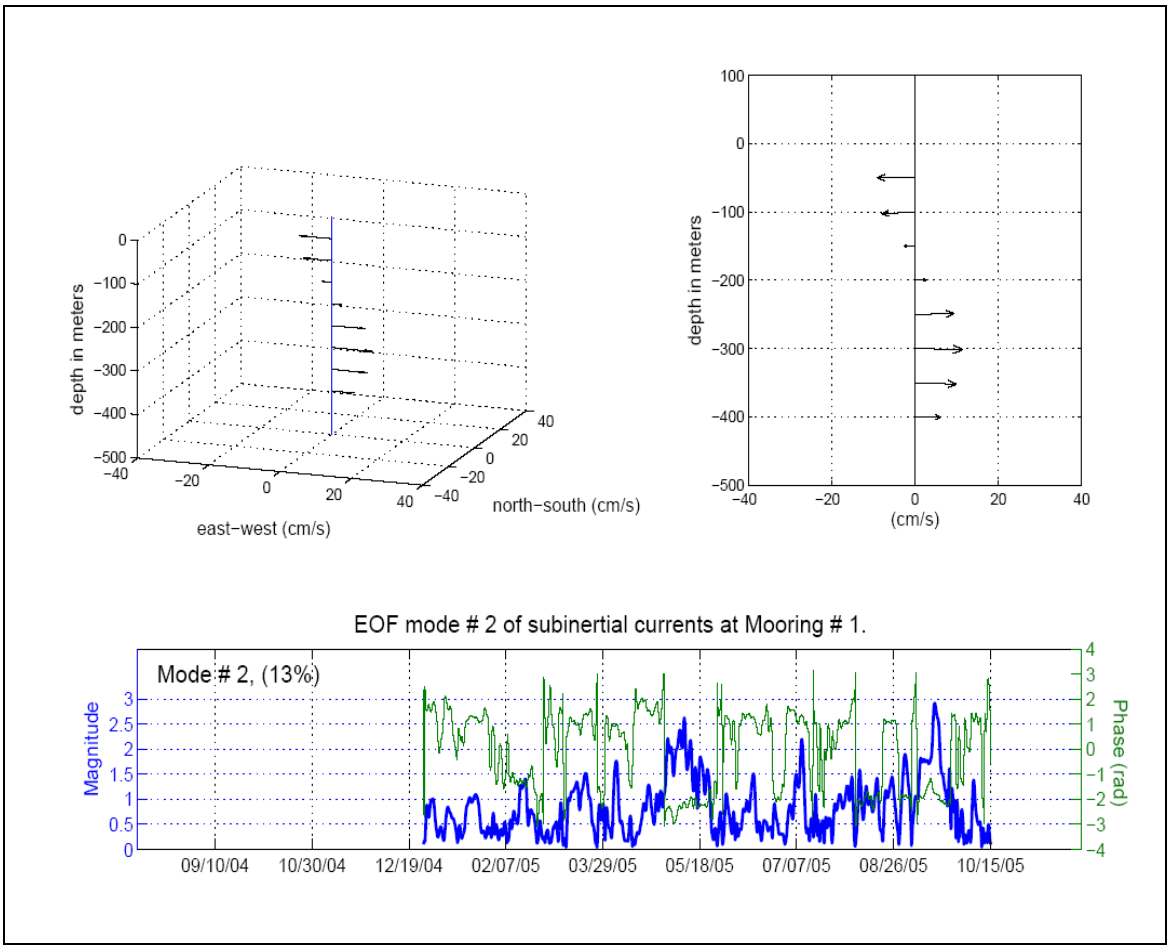

Figure 41. First two EOF complex modes for the observed subinertial current interpolated at regularly spaced vertical levels on mooring MMS1. The upper two panels show the dimensioned spatial structure of the mode in two equivalent representations, on the left, vectors in 3-D space, and on the right, vectors in 2-D with the north-south/east-west component in the abscissa/ordinate directions and each vector starting at its corresponding depth. The lower panel shows the time series (also called principal components) of the mode. Since the EOFs are for a complex time series, i.e. u+i*v, both the spatial structure and principal components are complex and here presented with the time evolution of its magnitude and phase (continued).

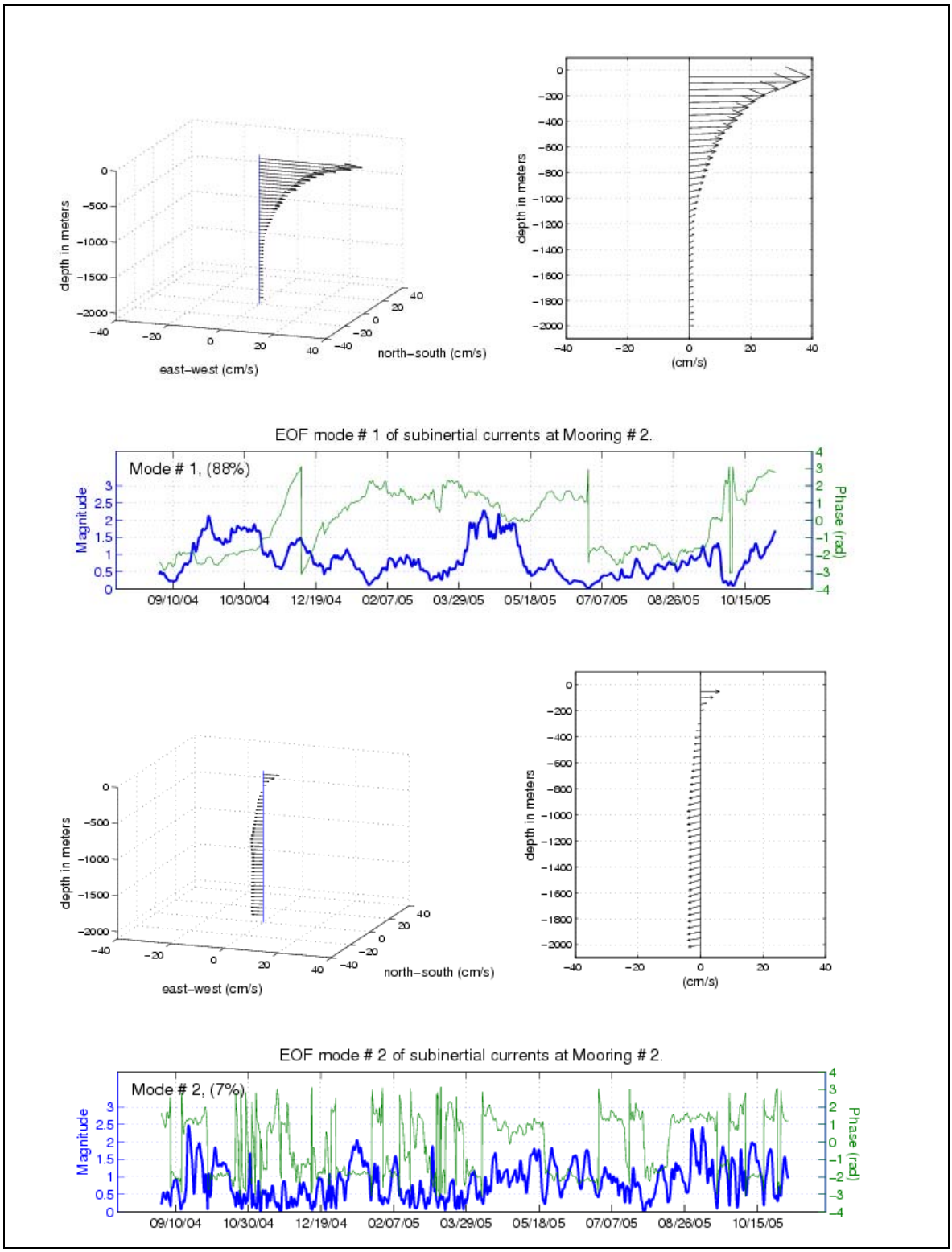

Figure 42. First two EOF complex modes of the subinertial current vertical profile measured on mooring MMS2. Currents have been linearly interpolated to nominal depths between 50 and 1,950 m every 50 m.

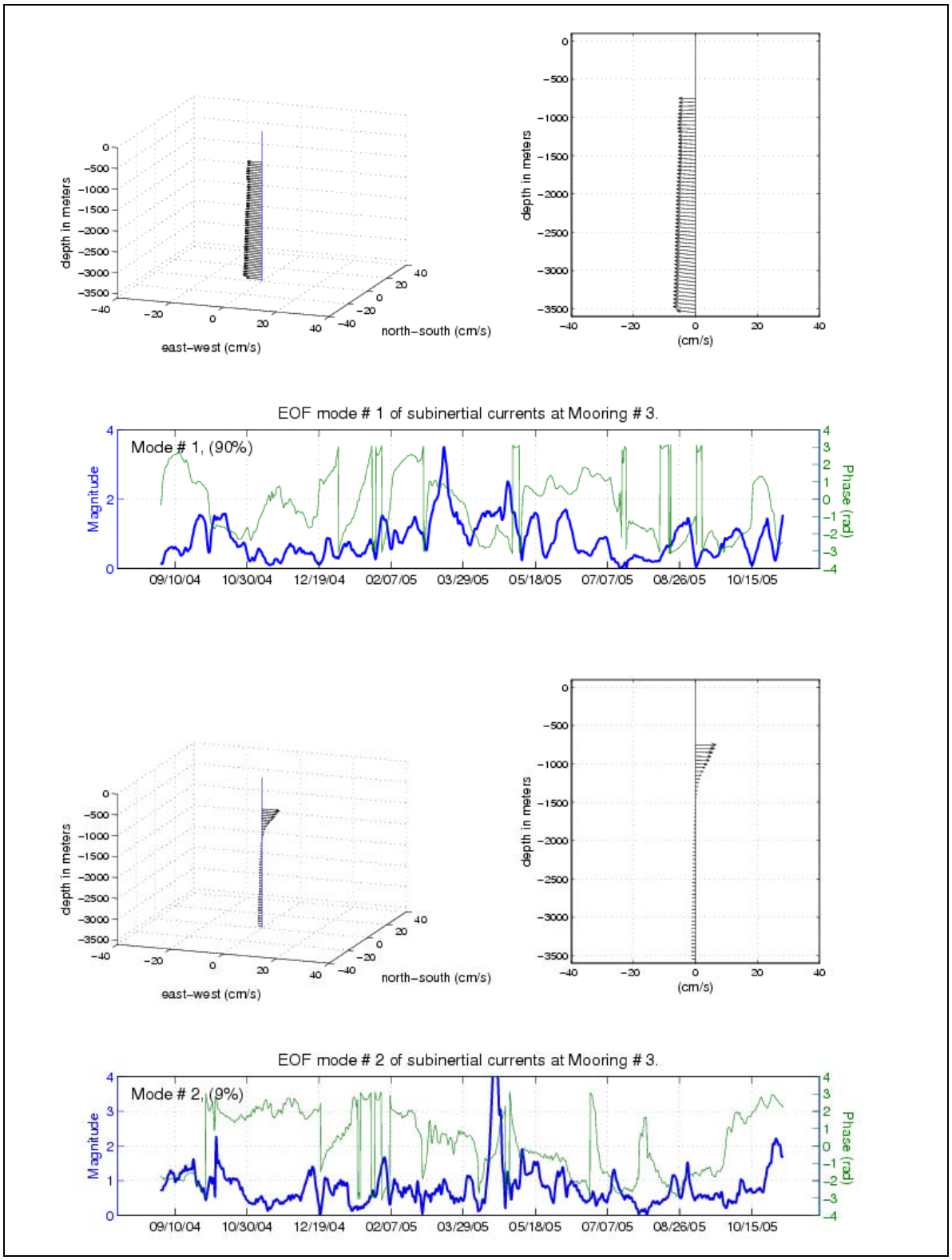

Figure 43. First two EOF complex modes of the subinertial currents measured on mooring MMS3. Currents have been linearly interpolated to nominal depths between 750 and 3,550 m every 100 m.

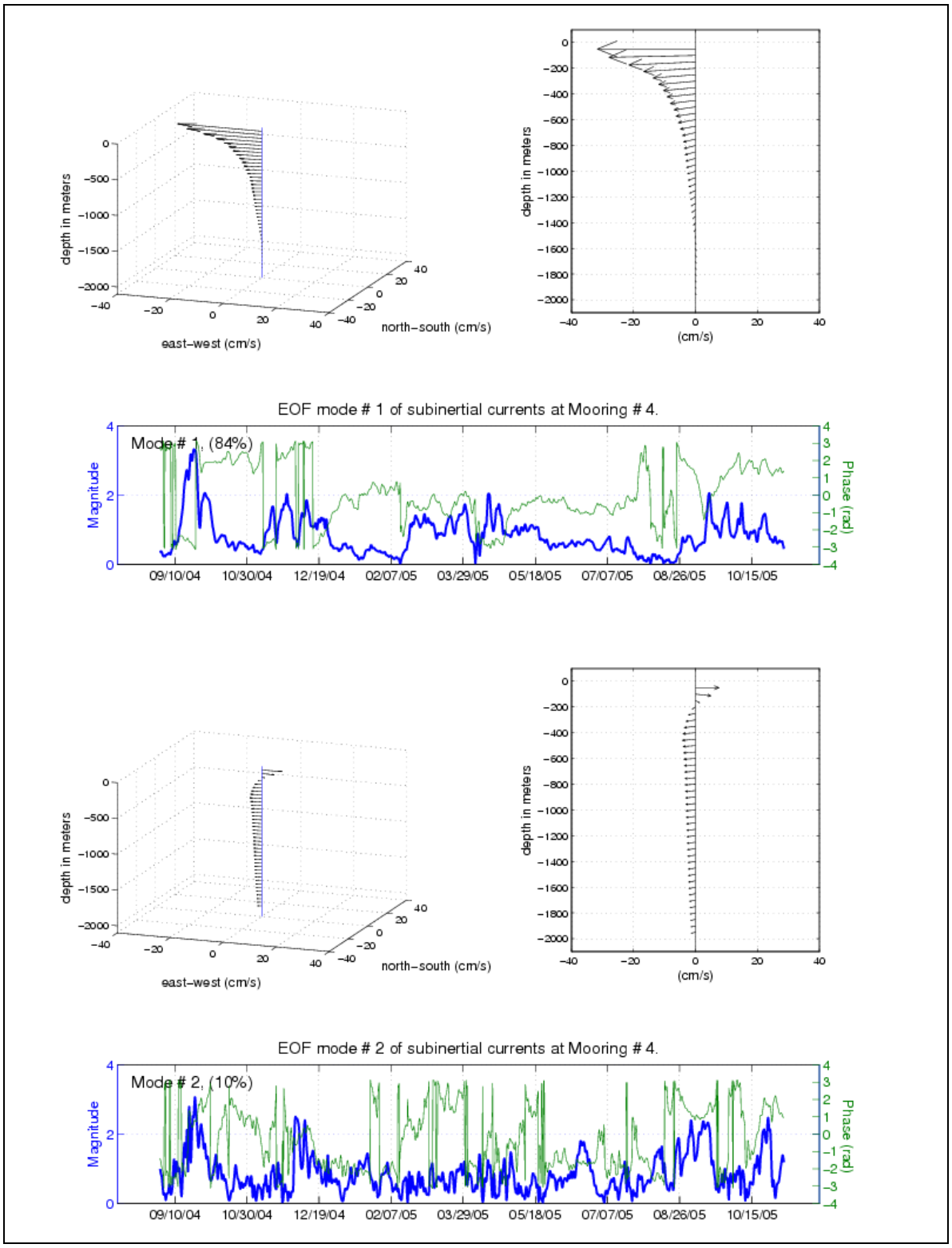

Figure 44. First two EOF complex modes of the sub-inertial current measured on mooring MMS4. Currents have been linearly interpolated to nominal depths between 50 and 1,950 m every 50 m.

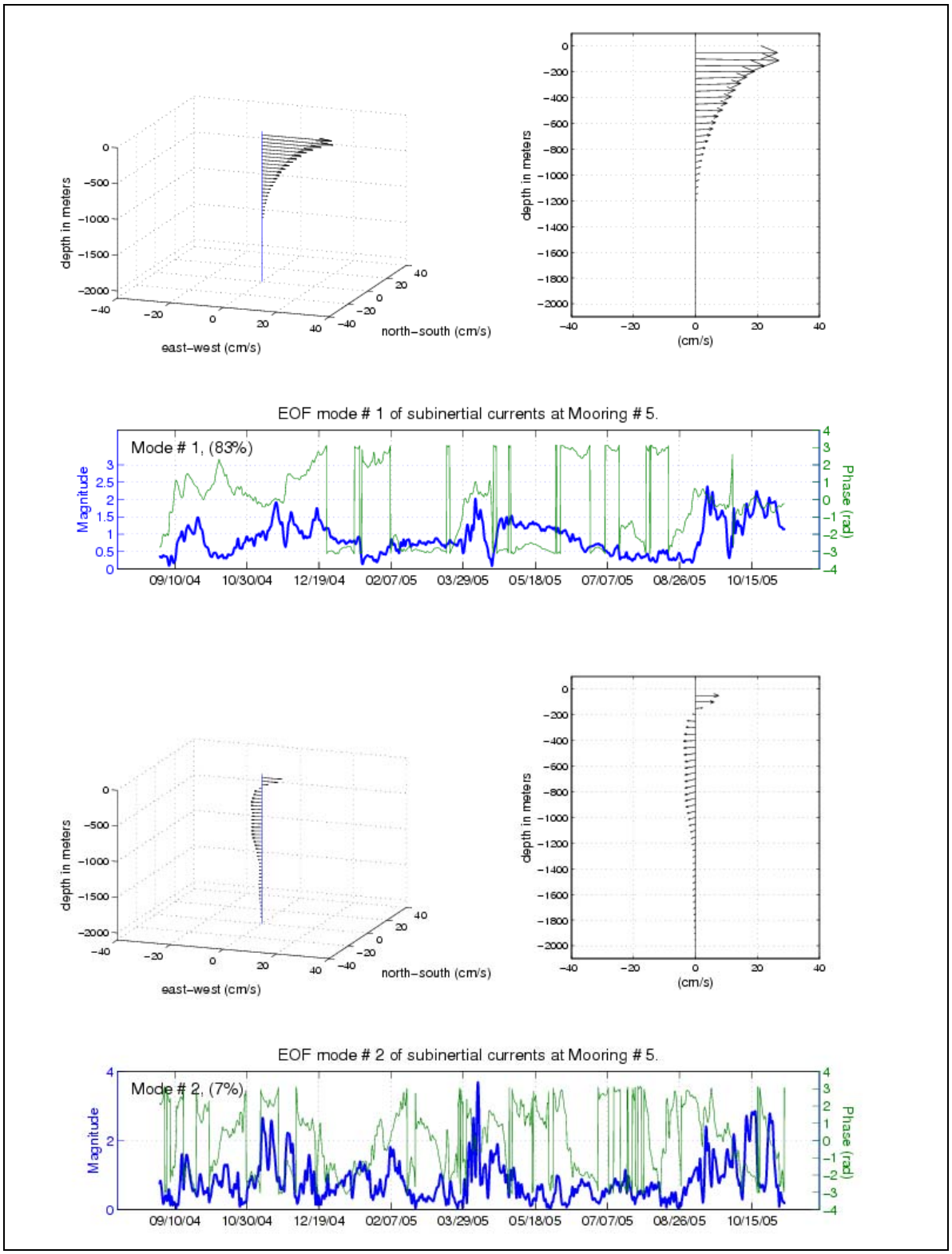

Figure 45. First two EOF complex modes of the sub-inertial currents measured on mooring MMS5. Currents have been linearly interpolated to nominal depths between 50 and 1,950 m every 50 m.

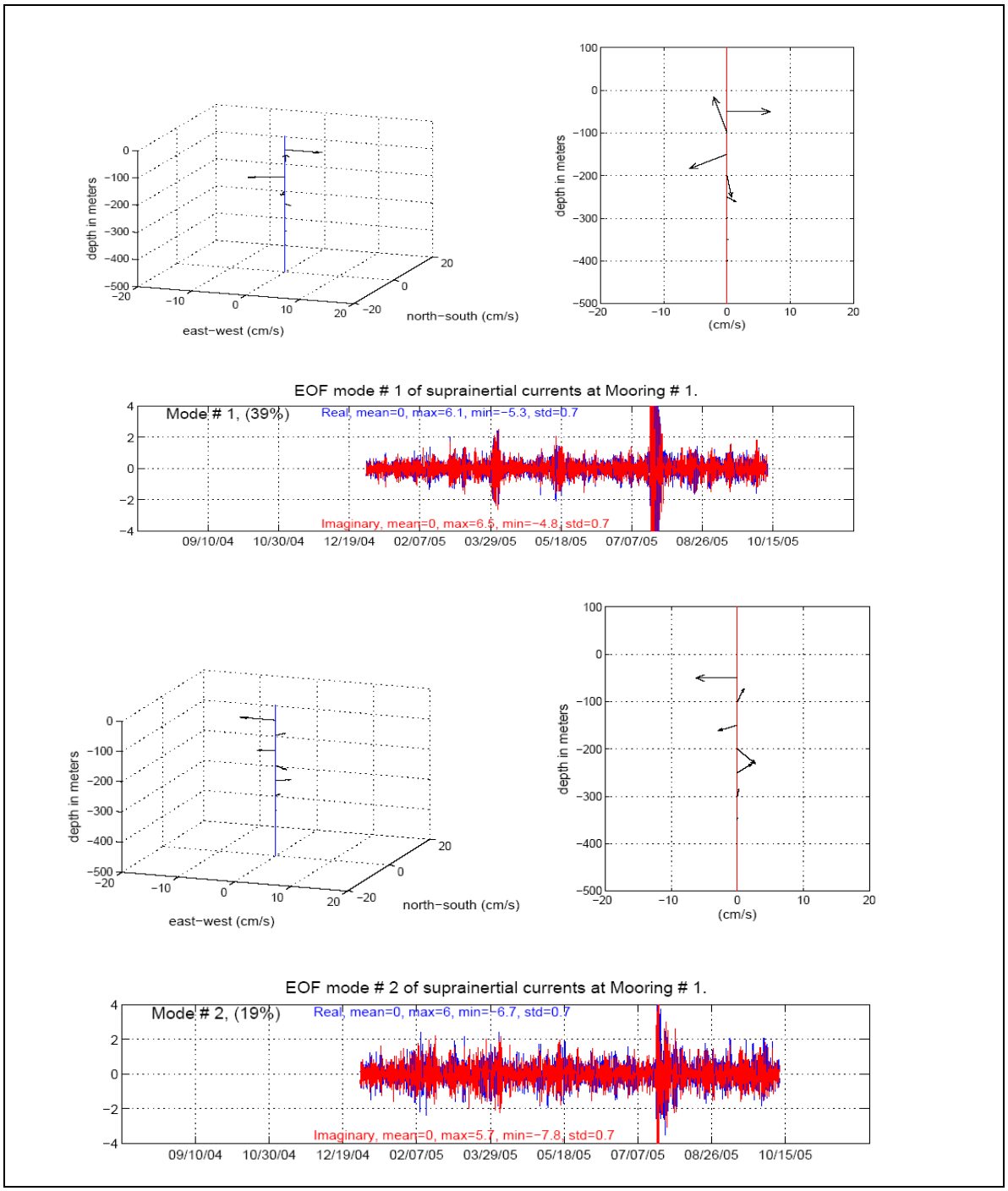

Figure 46. First two complex EOF modes of the supra-inertial currents on mooring MMS1.

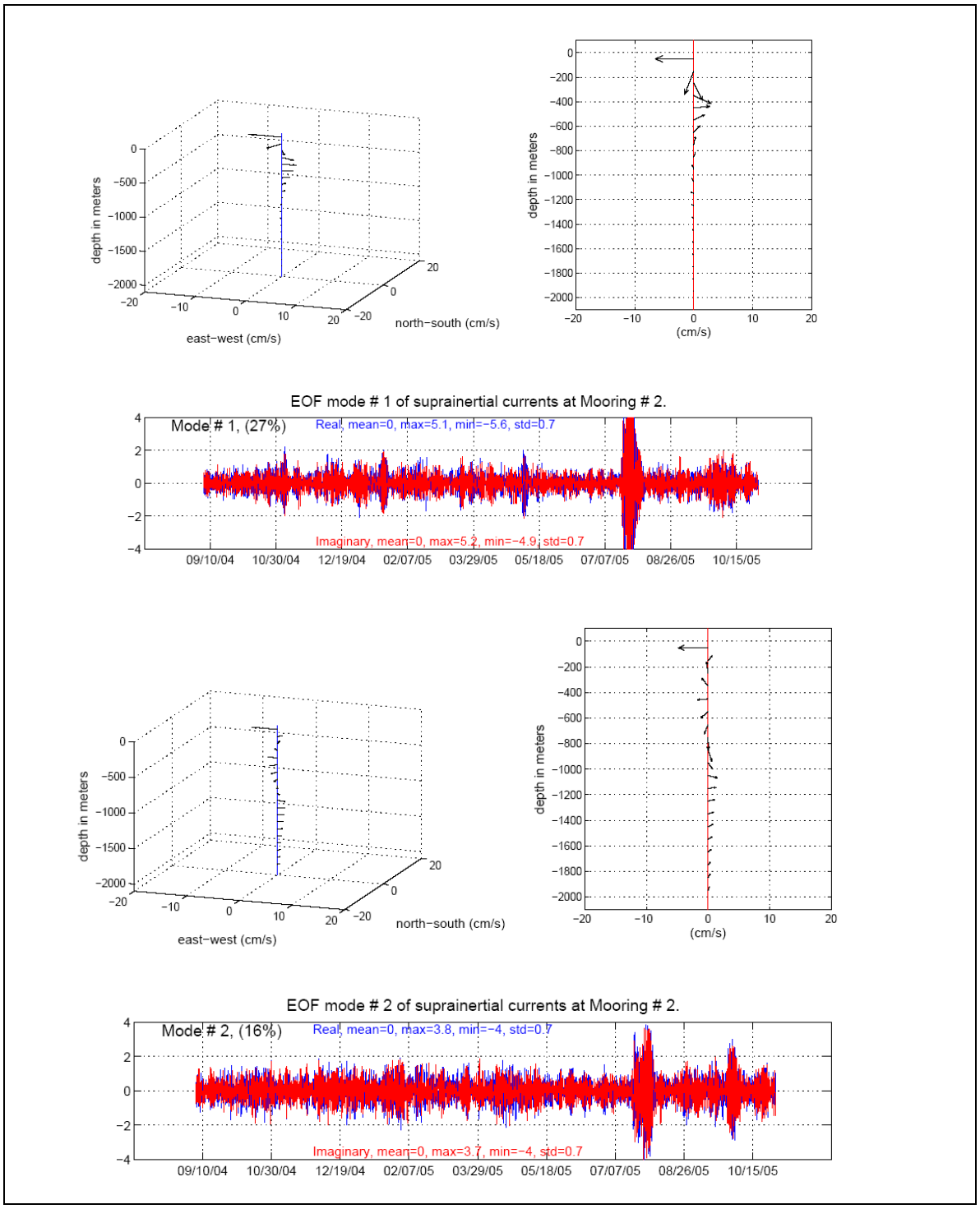

Figure 47. First complex EOF modes of the supra-inertial currents on mooring MMS2. Currents have been linearly interpolated to nominal depths between 50 and 1,950 m every 100 m.

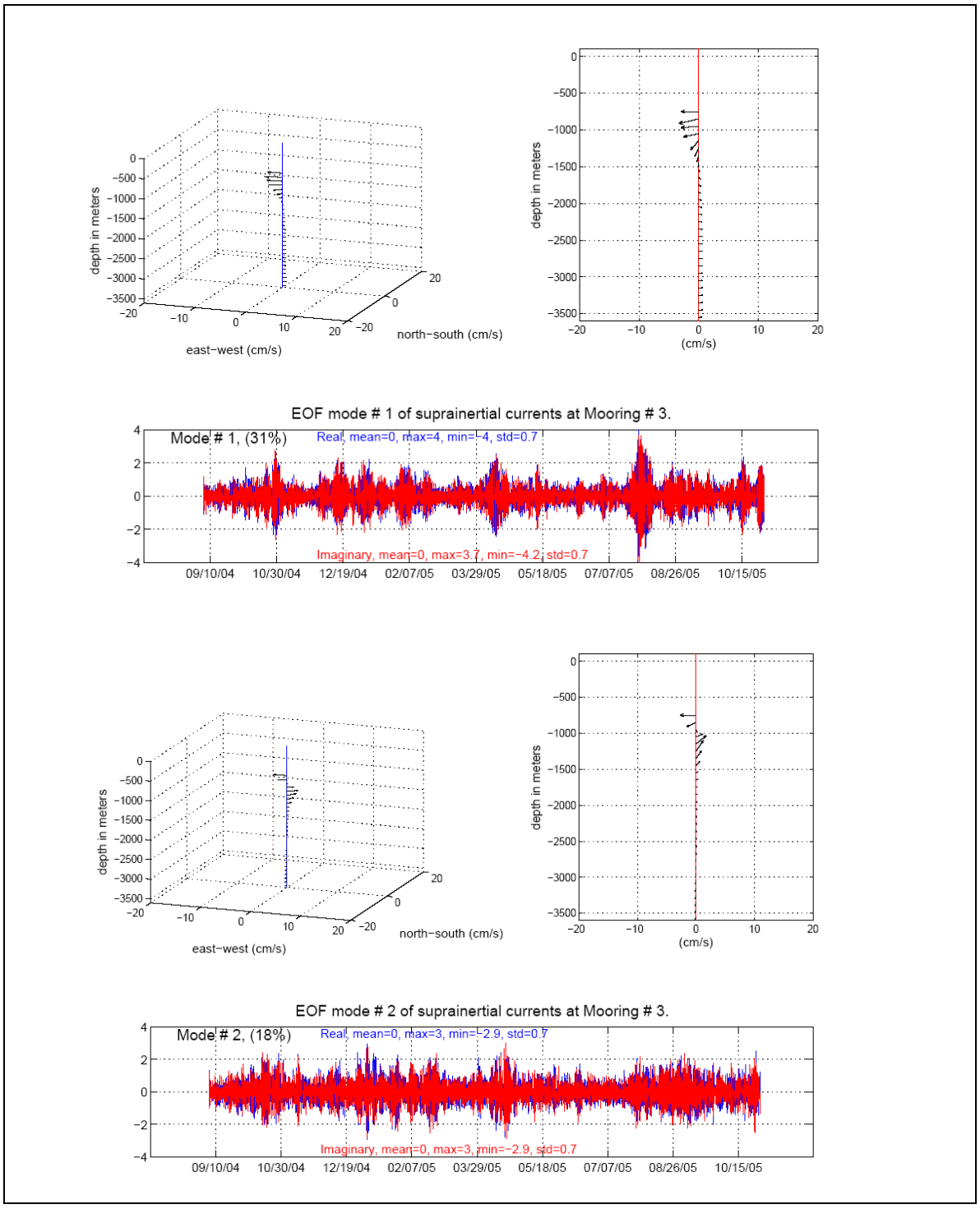

Figure 48. First two complex EOF modes of the supra-inertial currents on mooring MMS3. Currents have been linearly interpolated to nominal depths between 750 and 3,550 m every 100 m.

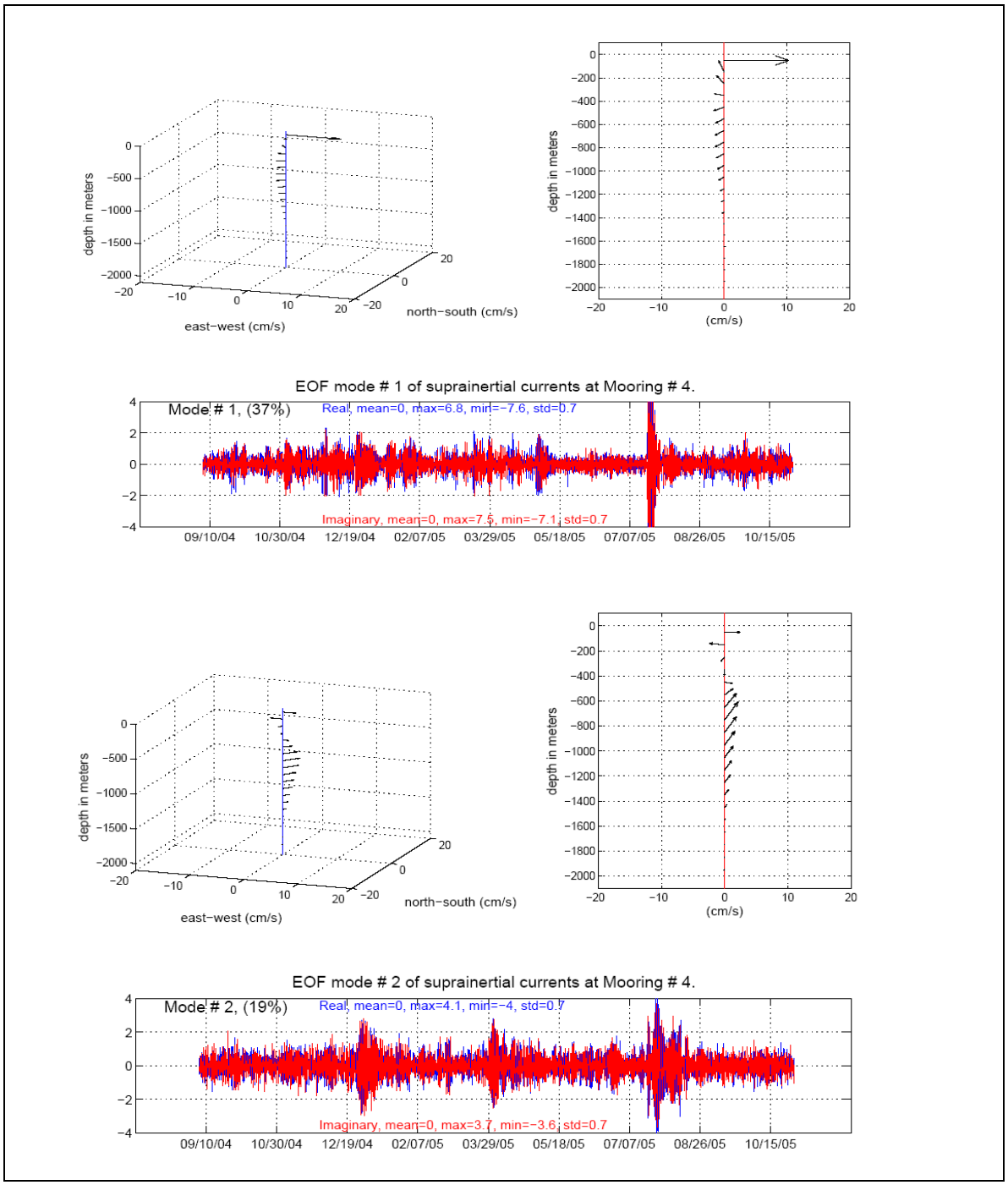

Figure 49. First two complex EOF modes of the supra-inertial currents on mooring MMS4. Currents have been linearly interpolated to nominal depths between 50 and 1,950 m every 100 m.

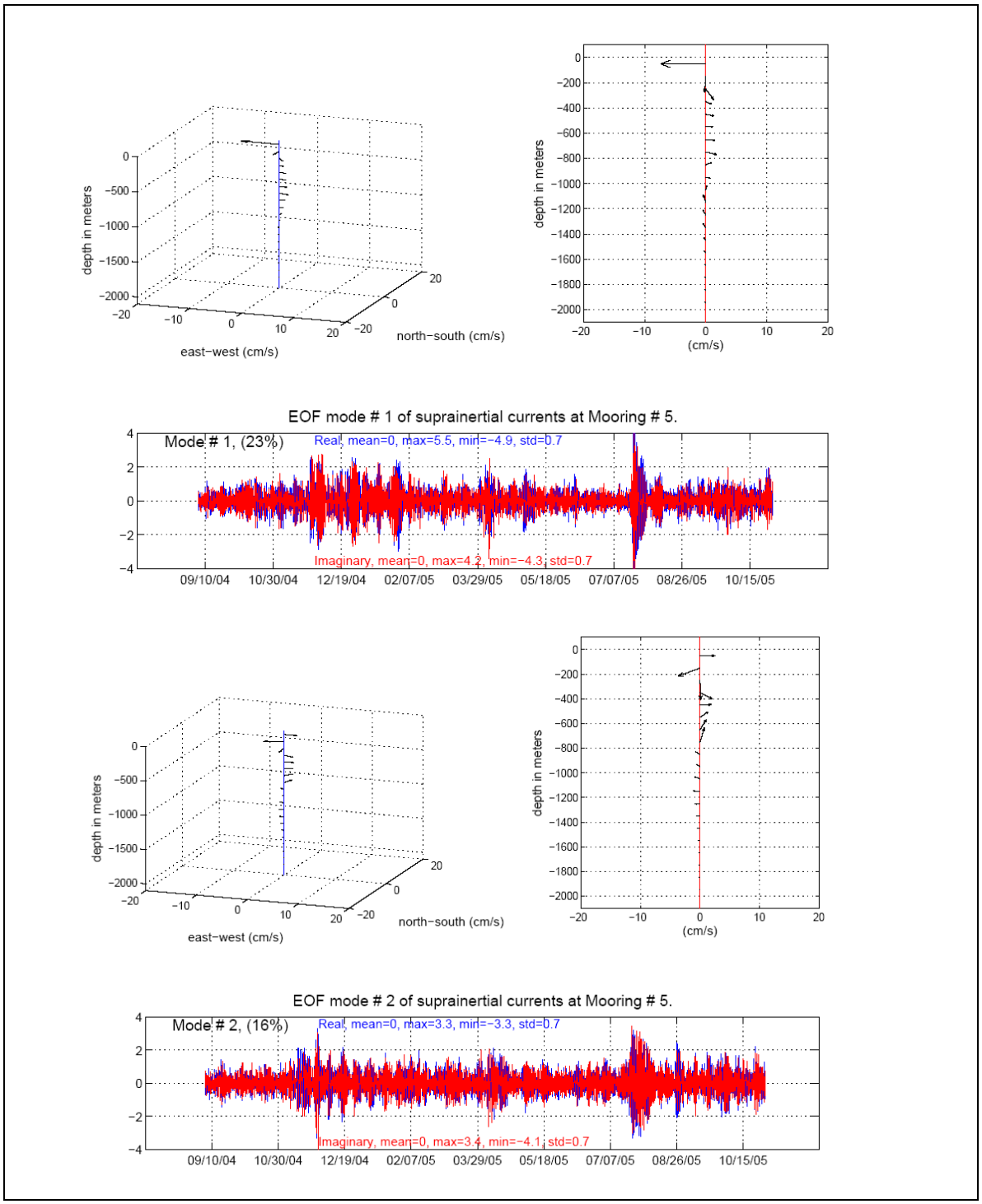

Figure 50. First two complex EOF modes of the suprainertial currents on mooring MMS5. Currents have been linearly interpolated to nominal depths between 50 and 1,950 m every 100 m.

7. MEASUREMENTS OF VERTICAL MOTION OF ZOOPLANKTON

A well known capability of ADCP measurements is the observation of diel vertical migration (there are many many references, see for example Ott, 2005; Luo *et al*., 2000; Tarling *et al*., 2001), it was used since the beginnings of ADCPs (Plueddemann and Pinkel, 1989). Two ADCP measurements are significant in relation to the amount of plankton and its vertical migration; the echo intensity and the vertical component of velocity. Here we present an analysis, related to such capabilities, as a subset of the measurements pertinent to this report. The moorings in 2000 m and the one in 3500 m have two upward looking LR75KHz RDI ADCPs close to 500 m and 1200 m below the surface. For completeness, we also include in this analysis measurements from the Canekito deployment (at 25° 05.47' N, 90° 39.00' W from May 12, 2003, to August 27, 2004) in 3500 m depth. The novel feature shown with these measurements, given their length, is the precise relative timing from surface to 1200 m of the mean diel migration cycle. To our knowledge, no other report has shown the timing in the mean cycle for all levels from the surface to 1200 m. With a limited amount of measured cycles, given the high variability and noise in the data, the different start, intensity, duration and end in the mean upward and downward migration phases cannot be established to the precision here shown.

Multiple studies have dealt with the estimation of zooplankton biomass via the echo intensity of echo sounders and ADCPs, which are themselves echo sounders (see for example Weeks *et al.*, 1995, Flagg and Smith, 1989, Record and de Young, 2006, Jiang *et al*, 2007). Following clouds of scatterers, shown as bands in the echo intensity profiles vs time graphs, the vertical migration speed might also be determined (see for example Tarling *et al*., 2001). The simultaneous measurements of acoustic backscatter intensity and vertical velocity have been combined in biomass balance equations (see Record and de Young, 2006, Putzeys and Hernández-León, 2005, and their references). In particular, Roe *et al* (1996) show a method to estimate the amount of biomass with the use of simultaneous RDI ADCP and hydrographic data, and Jiang *et al* (2007) made net tows to produce calibration curves between zooplankton biomass and acoustic backscatter intensity. Without the purpose of estimating biomass, in what follows we use the raw recorded RDI ADCP echo intensity as a biological-related signal.

The ADCP measures the velocity of scattering particles relative to the ADCP's variable velocity but, since its vertical velocity is estimated via the pressure gauge, the scatterers' vertical motion relative to the sea surface, which in this case are mostly zooplankton, is easily derived. For the observations here considered the corrections, due to ADCP motion, turn out to be insignificant for diel migrations; while migrations speeds are order 2/1 cm/s at 300/900 m depth the standard deviation of the ADCPs vertical velocity, via its pressure sensor, is order 0.05 cm/s.

The recordings of the Long Ranger RDI ADCPs where programmed for averages of 18 'pings' evenly distributed during half hour and there where 442 full days recorded, from August 24, 2004 to November 11, 2005. Figures 51 and 52 show color-coded diagrams of the vertical velocity and echo intensity as a function of depth and time. These two figures, made with the aid of the ADCP's manufacturer software (RD Instruments), are examples of the daily regularity. It will be shown how the timing in the migration varies with depth. Near surface plankton reaches its maximum velocity in downward migration earlier than deep plankton, and vice versa in the upward migration, therefore the nightly shallower stay of zooplankton is longer with depth.

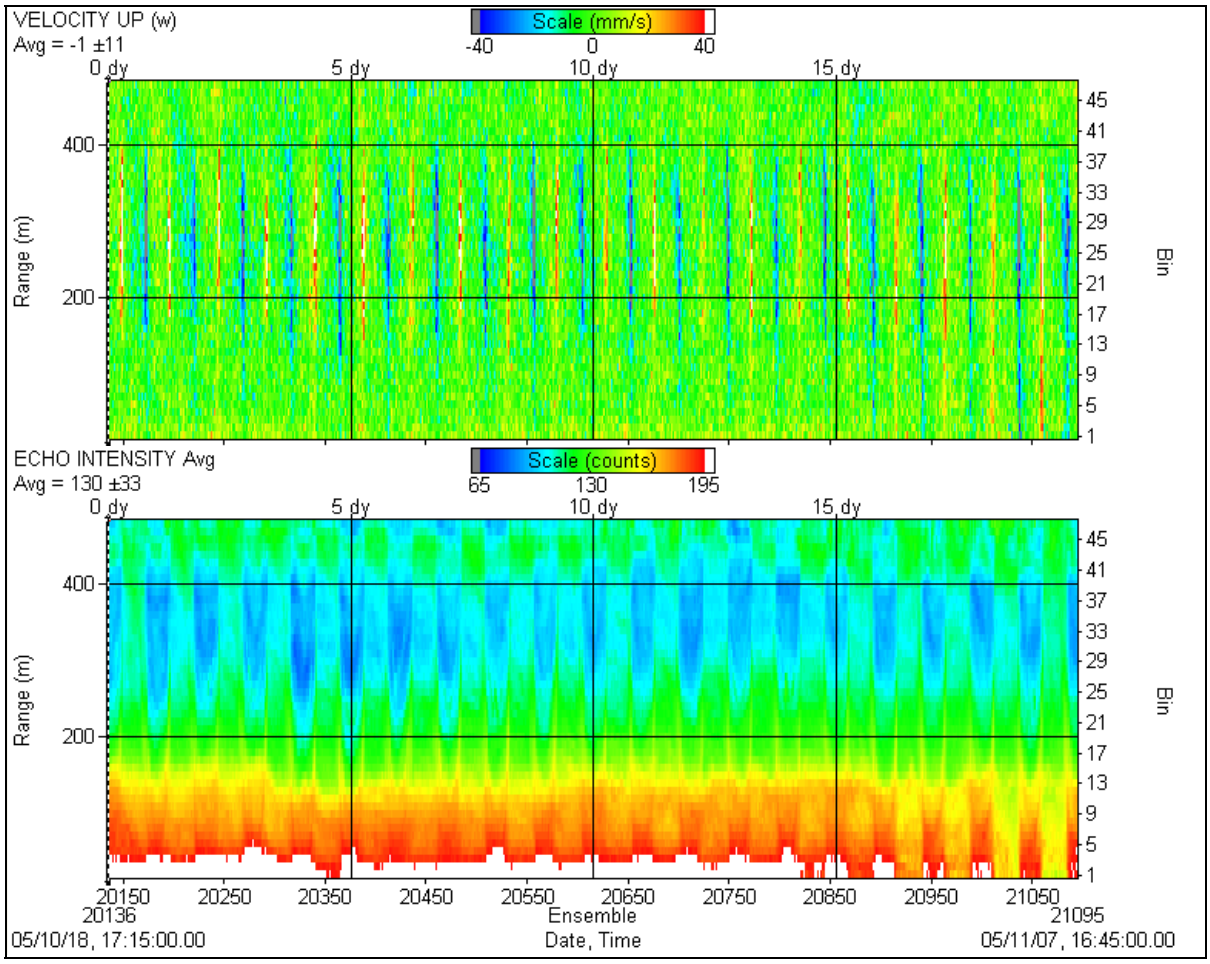

Figure 51. Twenty diel cycles of the vertical velocity (upper frame) and echo intensity (lower frame) for the RDI 75kHz ADCP moored at a mean depth of 550 m in mooring MMS5. The depth interval goes from 550 (Range scale 0) to 50 m (Range scale 500) below the surface.

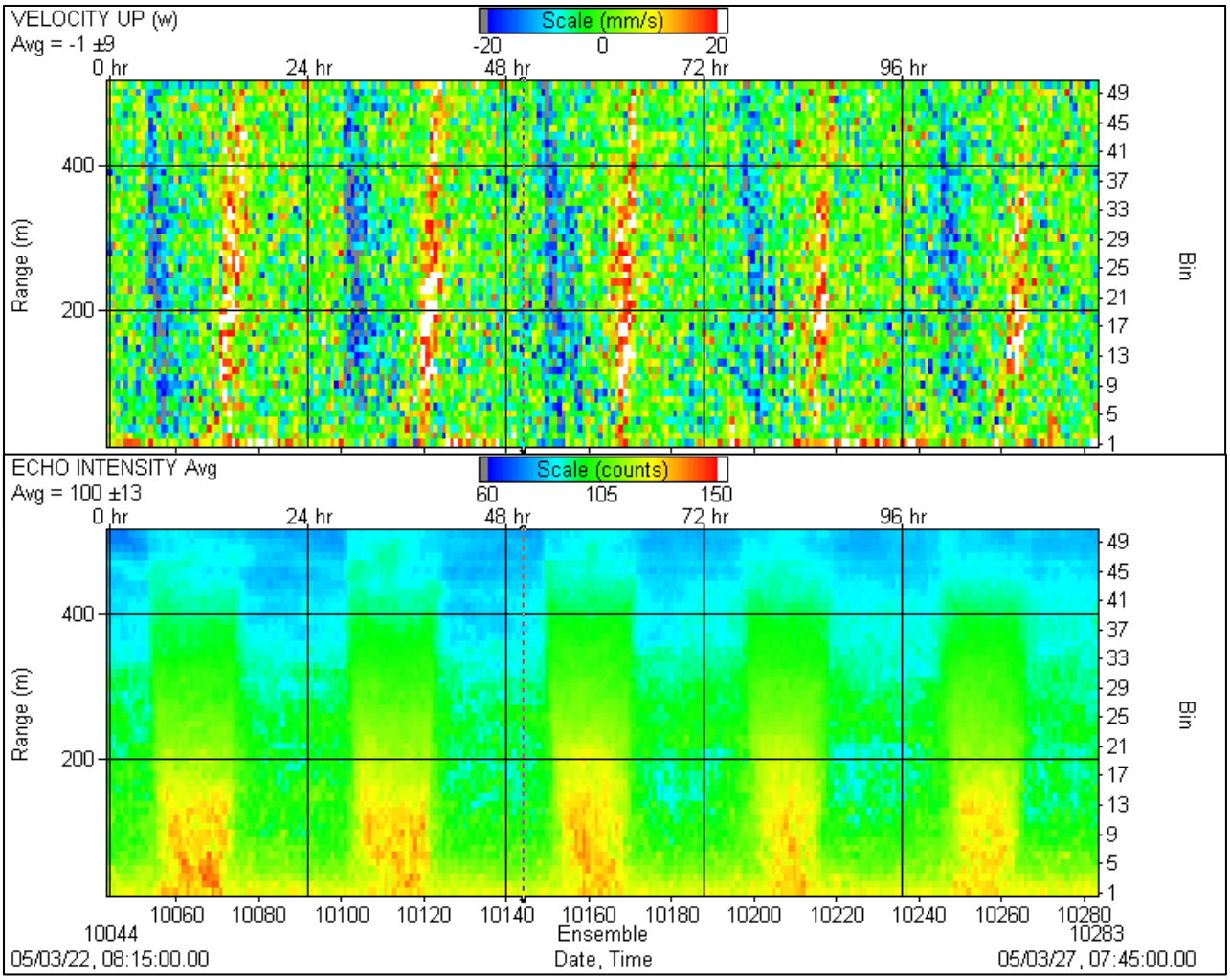

Figure 52. As in Figure 51, five diel cycles are measured by another RDI 75kHz ADCP in the same mooring (WG-5), but looking upward from a depth of 1,250 m, showing depths from 1,250 to 750 m below the surface.

The analysis here presented first shows how a time axis based on shifting the GMT is appropriate for computing the mean diel cycle (Section 7.1). Then the major differences for near surface and deep layers are shown (in Section 7.2.). Last, the mean diel cycle is shown as a function of hour of the day and depth (Section 7.3), followed by a discussion (Section 7.4).

7.1. Proper Time Scale for Daily Migration Cycles

In order to produce a low noise signal in vertical velocity time series, we average ADCP bins 5 to 20, which are neither too close or far from the ADCP. Figures 53 and 54 show fractions of the available records averaged over 150 m thick layers as function of time corresponding to the mooring WG-5.

The ADCPs were programmed for recordings of 18 ‘pings’ averaged over half hour. The near surface oscillations are more regular than in the 1000 m deep layer. Figures 53 and 54 show two examples where diurnal variations in vertical velocity and echo intensity are easily recognized. They show the well-known correlation of daylight and migration cycles. The daylight cycle is shown in these figures via the black trace; a function that is larger/lower during

daylight/night with jumps at sunrise and sunset. We used the conventional definition for sunrise and sunset; the times when the upper edge of the disk of the sun is on the horizon. We checked our formulas with tables published by the U.S. Naval Observatory (http://www.usno.navy.mil/USNO) having a maximum difference in a full year of 1.8 min and a standard deviation of less than one min. The sunrise and sunset, which by definition are close to 06:00 and 18:00 in local times, are for 96º 18.071' W, the longitude of WG-5, close to 12:00 and 24:00 GMT (Figures 53 and 54). Echo intensities shown in Figure 54 were vertically averaged in the same way as the velocities shown in Figure 53.

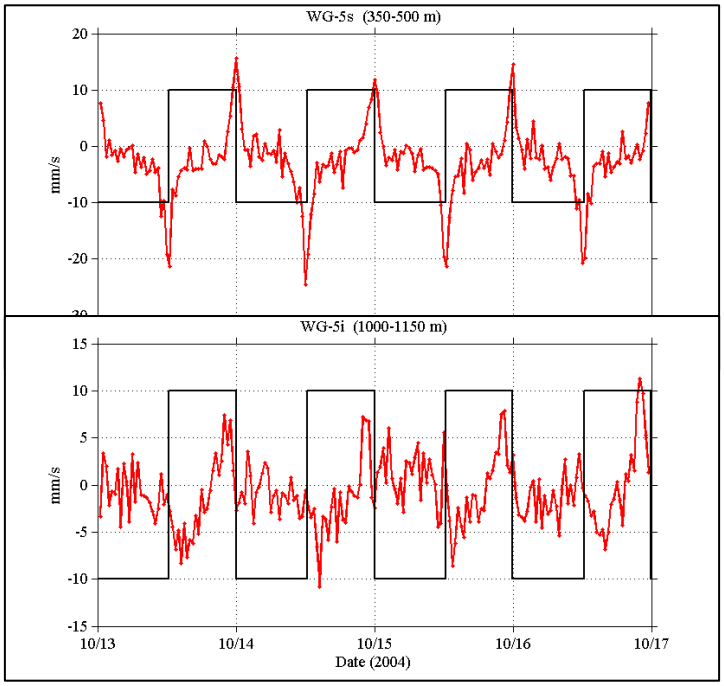

Figure 53. Time series of the diel cycle in vertical velocity averaged over two 150 m thick layers, one near surface and the other deep centered at 425 and 1,075 m. The time is in GMT and the black trace indicates the sunlight cycle (see text).

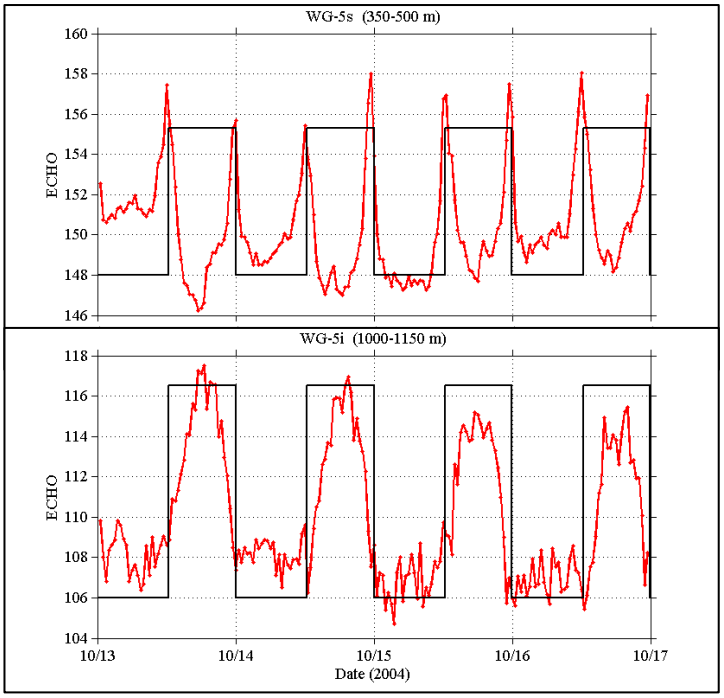

Figure 54. Time series of the diel cycle in echo intensity, in similar format than Figure 53. Notice the echo intensification at sunrise and sunset during the downward and upward migrations in the near surface layer and the intensification during daylight in the deep layer signal.

The timing of migrations is very much phase locked with the sunrise (downward migration) and sunset (upward migration) to the point that the daylight length shows when the stack of days is graphed over the full set of days recorded. Figures 55-57 are from the Canekito data.

To properly average the available individual daily cycles and thus produce a mean cycle, a time scale based in the sunrise and sunset times is needed. Using the local time, the mean will average on times shifted from the natural reference that sets the cycles, and produce an over-smoothed estimate of the mean cycle. Shifting the first half of the daily cycle so 06:00 coincides with sunrise in the downward migration phase, and shifting again the second half cycle so 18:00 hours coincides with the sunset upward migration the alignment is quite clear (Figures 56 and 57). There is a higher degree of regularity in the near surface than in the deep measurements, and the amplitude of the velocity cycle is larger in the near surface than at depth.

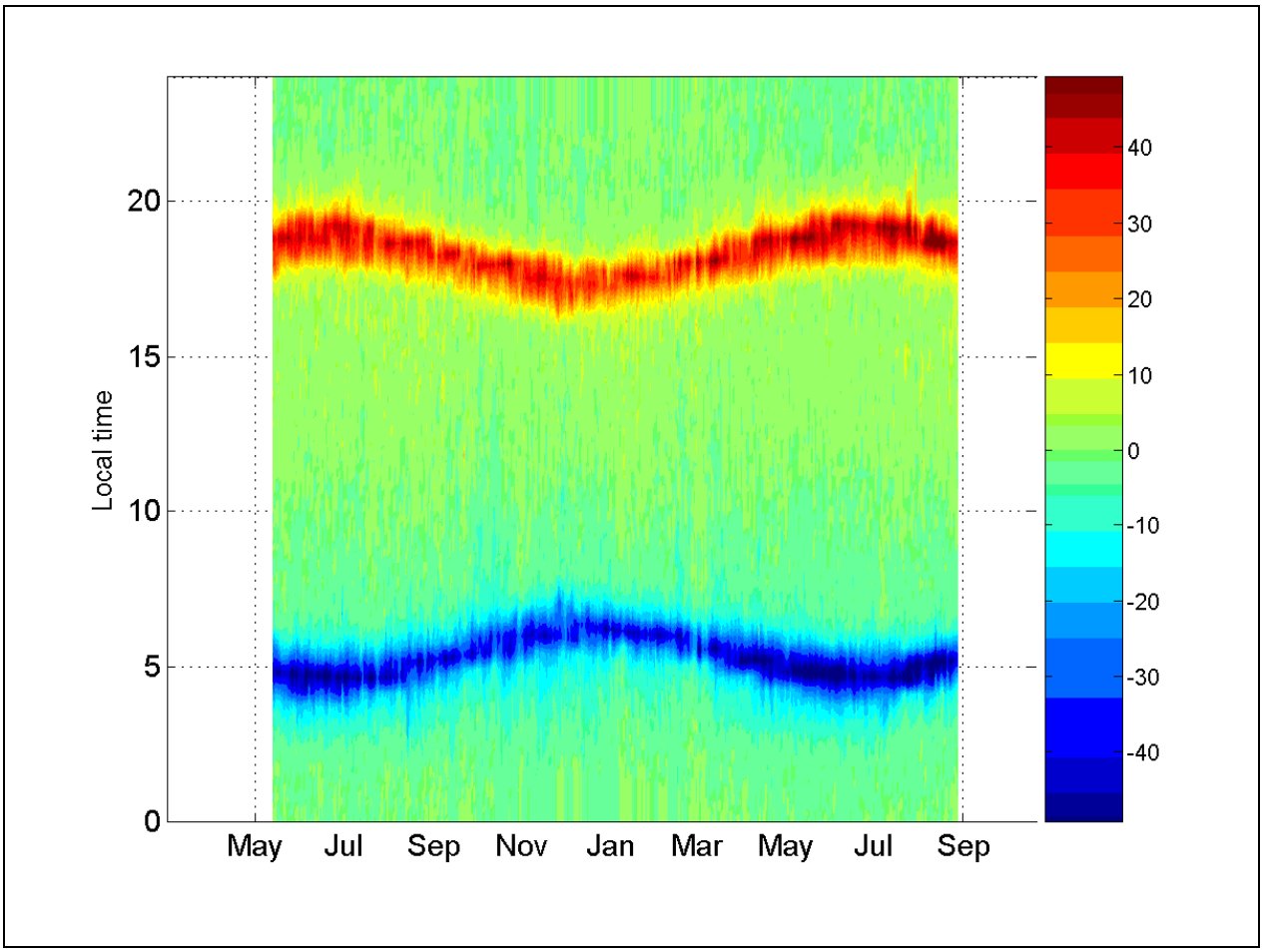

Figure 55. Color-coded diagram of the vertical velocity in the near surface layer, as a function of date, throughout the Canekito measuring period. There are 473 days and the migrations show the modulation by the daylight length; shorter in winter, longer in summer. The modulation also shows weaker velocities in winter than in summer.

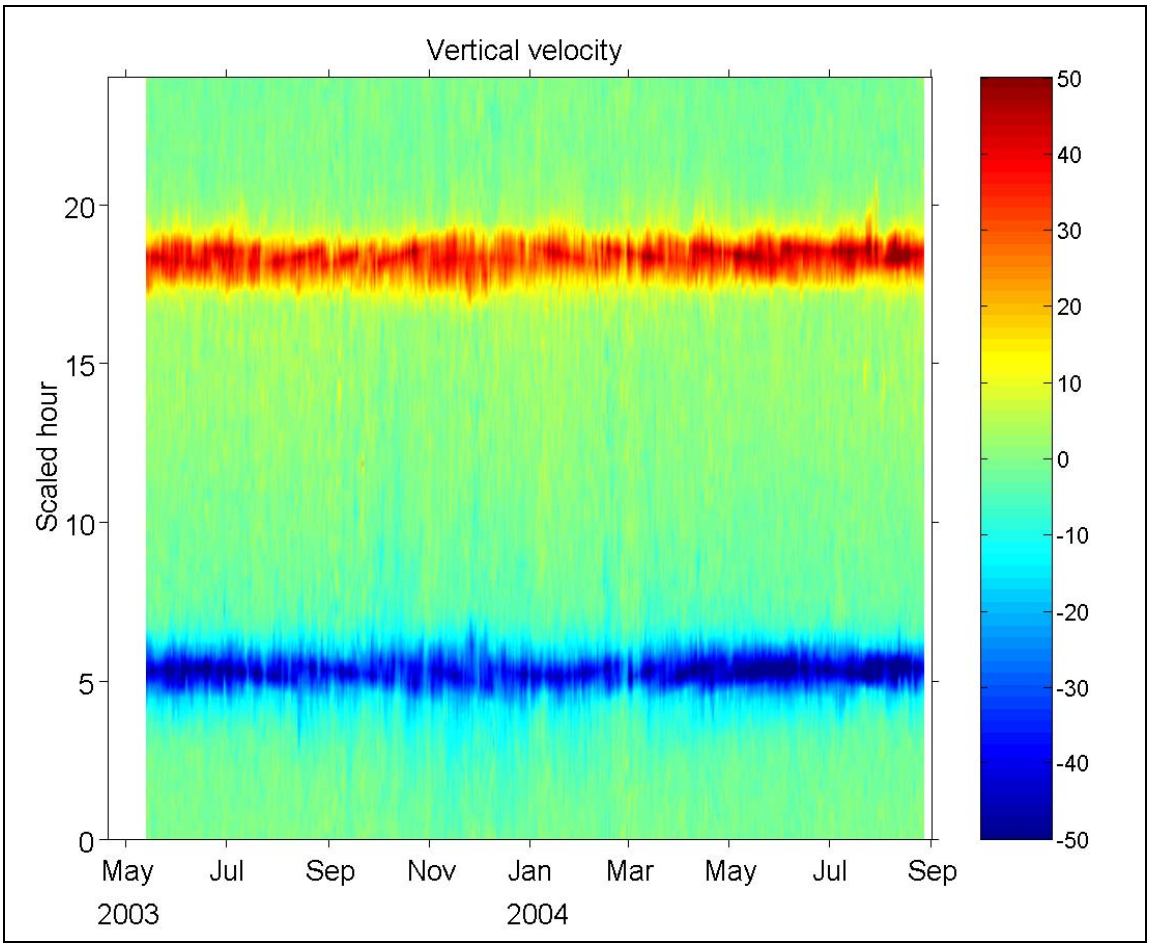

Figure 56. Vertical velocity as in Figure 55, but using the sunrise/sunset times as 06:00/18:00 as described in the text and shown in Figures 53 and 54. In comparison with Figure 55 the alignment is quite evident.

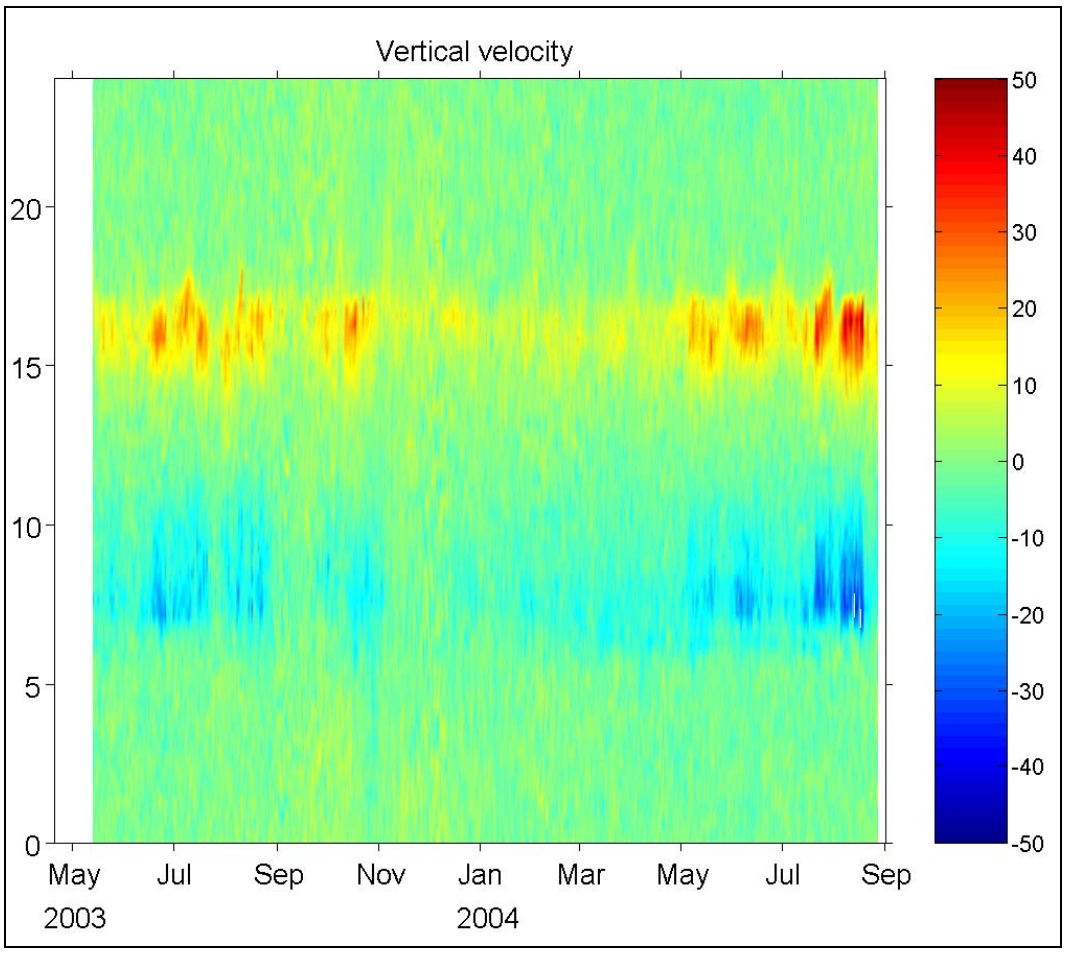

Figure 57. Vertical velocity in the deep layer, near 1,000 m below the surface, with the same sunrise/sunset times as in Figure 56. The deep layer has a weaker velocity cycle and is less regular than the near surface layer.

7.2. COMPARISON OF THE EUPHOTIC ZONE AND 1,000 M DEPTH MEAN DIEL CYCLES

Having the sunrise (Sr) and sunset (Su) as reference, it is appropriate to define the time axis relative to such times. An on purpose over sampled linear interpolation, with a uniform time interval of 3 min from 5 hours before sunrise or sunset to 5 hours after, allows to stack all days and average them to yield the mean cycle, as shown in Figures 58 and 59.

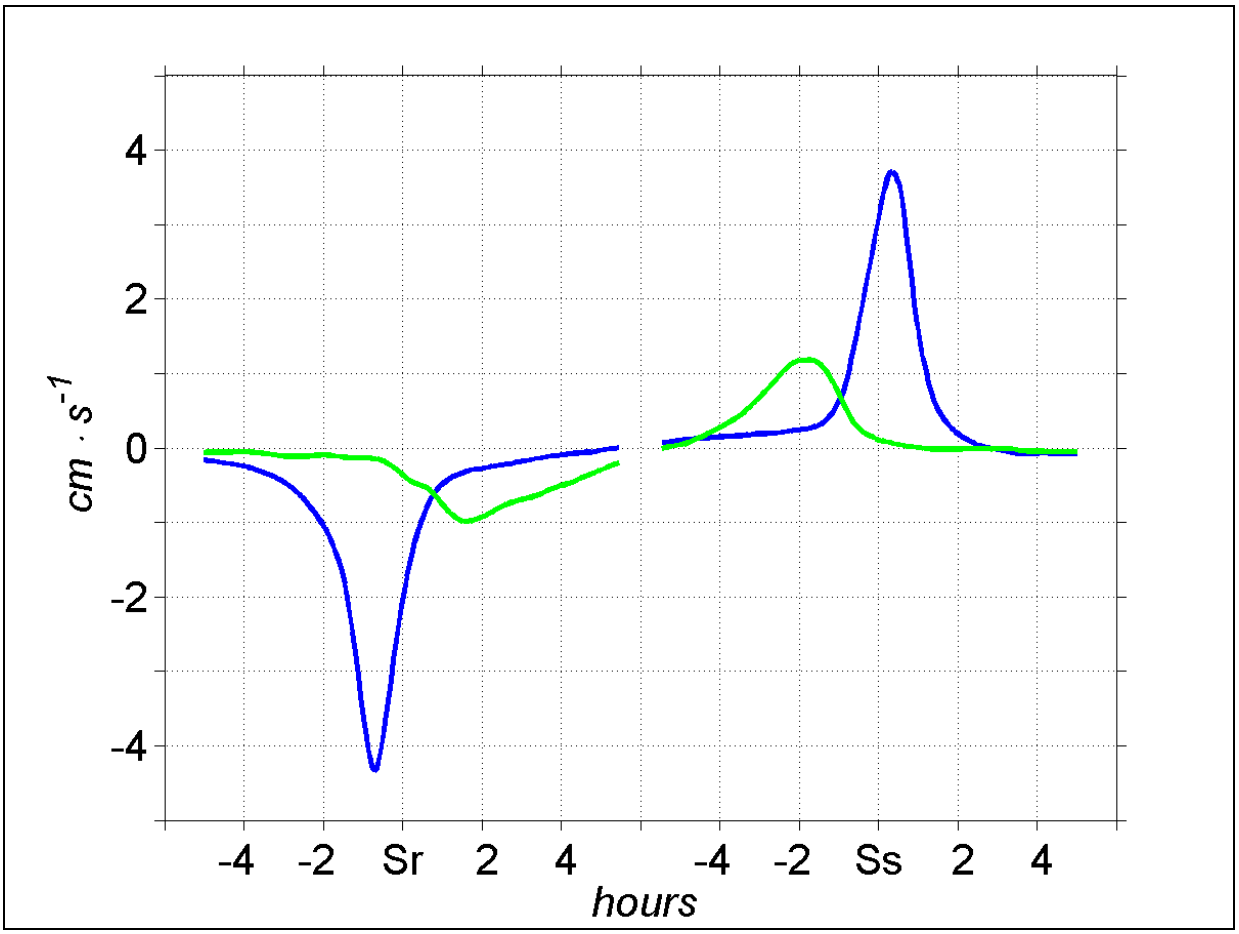

Figure 58. Two functions are the mean diel cycle in vertical velocity for the data shown in Figures 56 and 57 (i.e., for two 150 m thick layers), here with the time axis defined in hours relative to sunrise (Sr) and sunset (Su). The blue and green traces are for the near-surface (Figure 56) and deep (Figure 57) layers.

The standard deviations of vertical velocities in the near surface and deep layers are 1.21 and 0.58 cm/s while once the diel cycle is removed are 0.29 and 0.37 cm/s. The daily cycles account for 94% and 59% of the variance in the upper and deeper levels, therefore the regularity in the near surface is much grater than in the deep layer. The deep and near surface mean velocity cycles show the fastest migrations at different times. In the downward phase, the near surface zooplankton reaches the maximum speed during twilight before the sunrise, but the deep zooplankton has its maximum downward motion well after sunrise. In contrast, the maximum upward migration speed occurs earlier as depth increases.

The echo intensities time series, as in Figure 54, show similar variability but substantial different means. The standard deviations of the full series shown in Figure 54 are 5.2 for the near surface, and 7.5 for the deep layer, but their means are 150 and 106, respectively. Hence, we plot the anomalies.

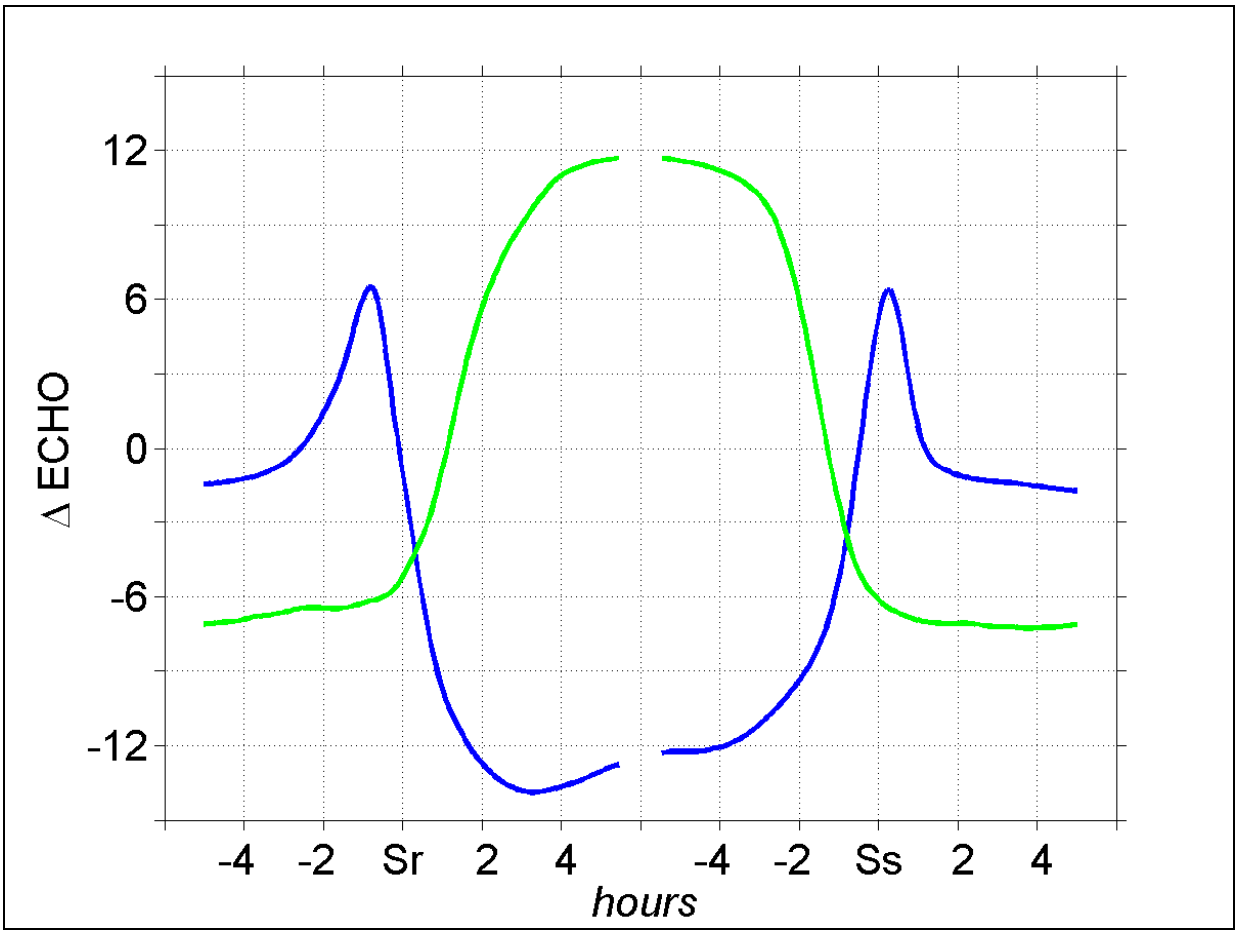

Figure 59. Functions shown display the anomaly in the mean echo intensity cycle following the same format as Figure 58; averaged over two 150 m thick layers and 473 days or cycles, and with the time axis relative to sunrise and sunset. The blue and green traces are for the near-surface and deep layers. Notice the higher echo intensity during daylight for the deep layer, contrasting with the well-studied behavior in the near-surface layer.

Figures 58 and 59 show the main distinct behavior for shallow vs deep layers, the purpose of this analysis is to manifest these differences as a continuous function of depth.

7.3. MEAN CYCLES AS A FUNCTION OF HOURS OF THE DAY AND DEPTH

Having more than 400 days in each of the ADCPs used in this section allows splitting the functions shown in Figures 58 and 59 in each level. Since the ADCPs were programmed with a vertical resolution (i.e., bin size) of 10 m we keep such in this section. Figures 60 and 61 are the result of averaging after linear interpolations; one in depth, such that the vertical displacement of the ADCP is considered and each level is fixed relative to the surface, and the second in time with over-sampling as described in the previous section.

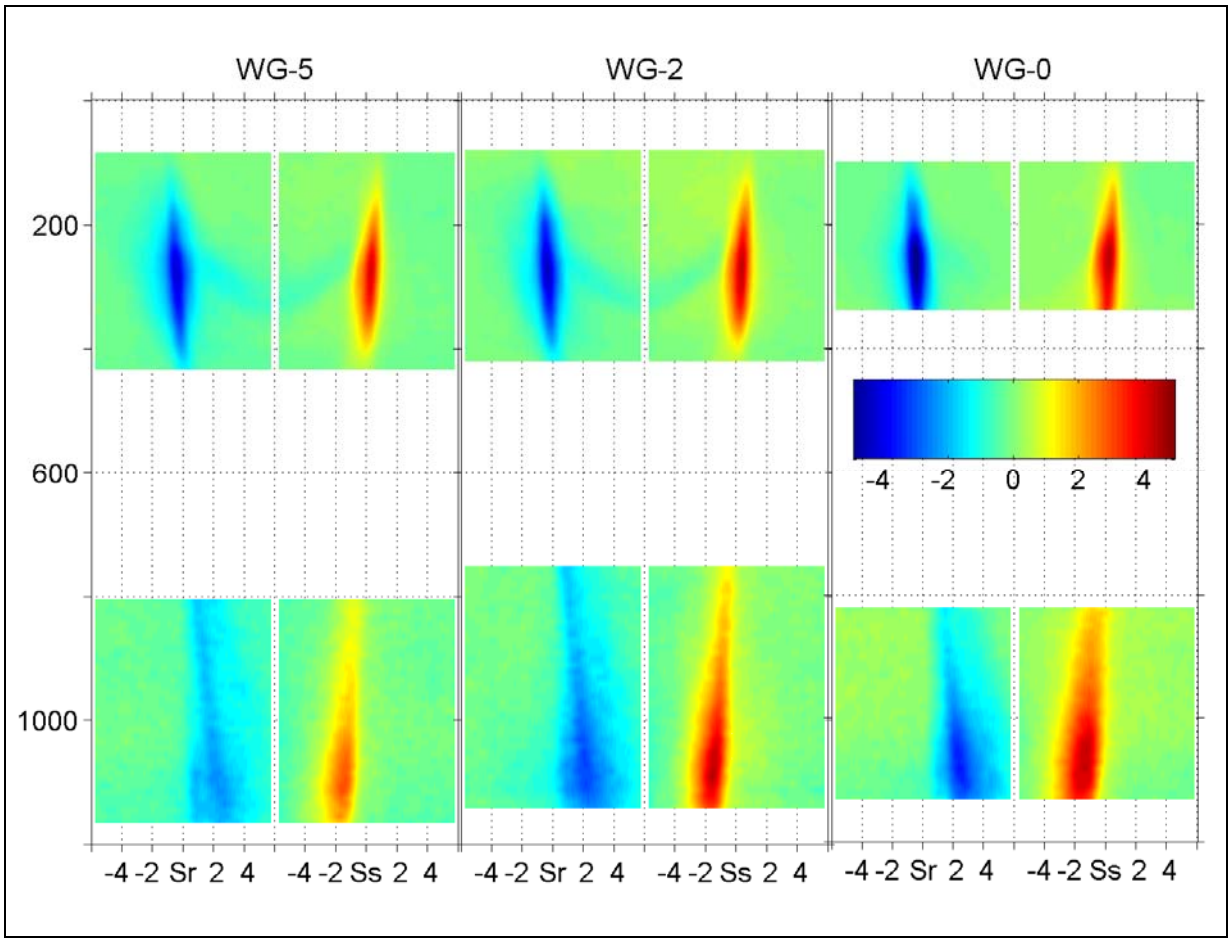

Figure 60. Color-coded mean vertical velocity diel cycle as a function of time, relative to sunrise and sunset as in Figure 58, and depth in m. The label on top is according to the mooring, with WG-0 for Canekito. The color scale, in cm/sec, at the gap in frame WG-0, applies to the data from 600 m to the surface, and divided by 3 applies to the deep cycle.

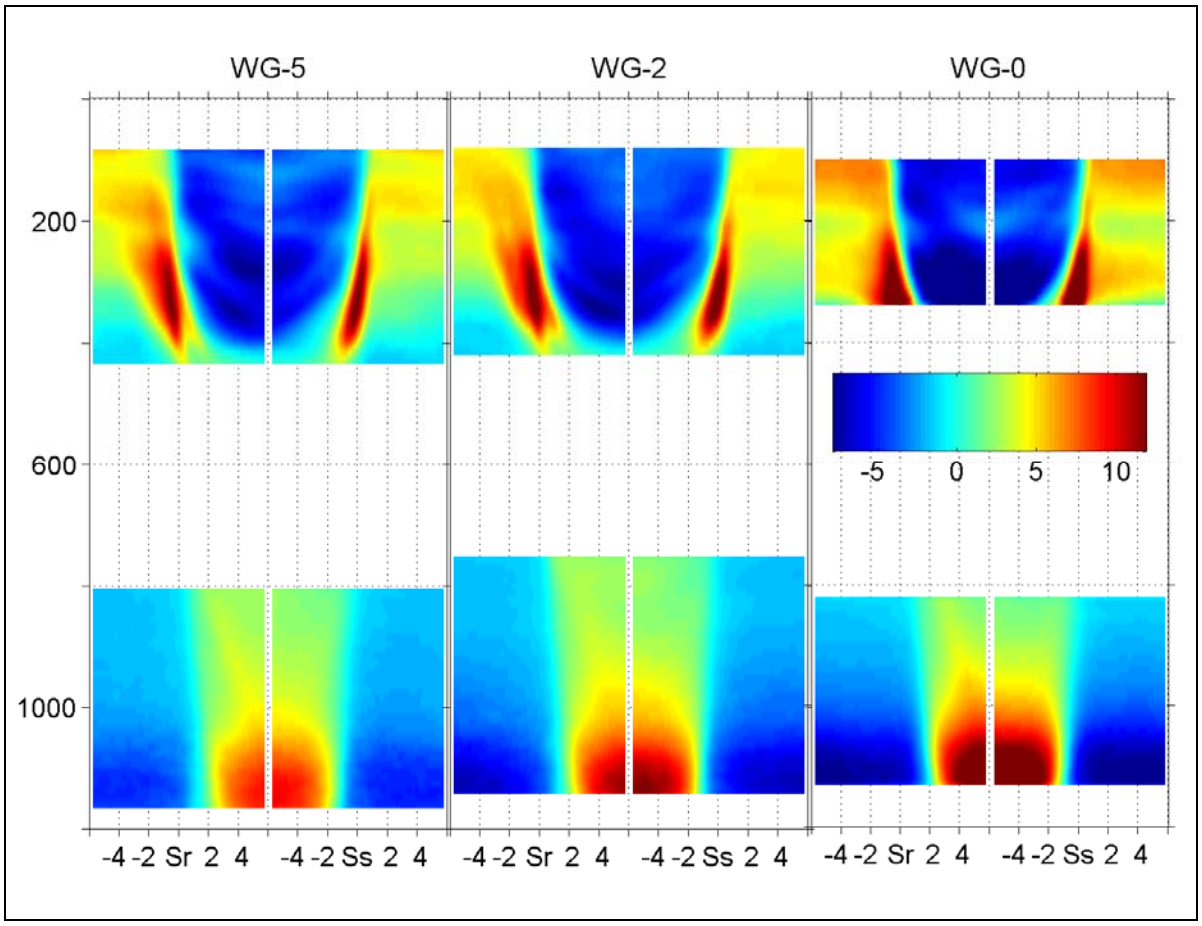

Figure 61. Anomaly in the mean echo intensity as a function of time and depth, following the same distribution as in Figure 60. The color-coded scale applies to all frames.

Peak vertical velocities of zooplankton at 100 to 500 m depths are near 4 cm/s≈144 m/h≈3500 m/day, values that are huge compared with low frequency water movements. This is also the case for the zooplankton's peak vertical velocities at 800 to1200 m depths; a value of 1 cm/s≈36 m/h≈860 m/day, therefore much larger than anything expected for low frequency water motion.

With the purpose of showing the intensity of such mean diel cycle the mean vertical displacement function is defined such that particles trajectories follow the mean velocity cycle as a function of time and depth. The displacements thus computed show the vertical positioning, during the daily cycle, of some mean-weighted zooplankton. Careful interpretation and statements should be used with such time-depth mean cycles. Each vertical velocity measured by the ADCP is a weighted mean of a large variety of scatters, with difficult to asses weighting factor per particle, and turbulent fluctuations in the water. The echo signal depends on a combination of properties including the emitted sonic signal and the size, hardness and form of the particles, some of which are passively drifting with the water, others, like the zooplankton, slipping thru the water. Figure 62a shows that *a weighted fraction* of the zooplankton which stays during daylight at 300 m, has *a weighted upward migration* of 80 m, while the same kind of fraction found at 100 m on daylight only migrates 20 m. In the deep, from 900 to 1100 m

depth, there is also depth-dependent amplitude of the migration cycle, varying between 20 and 40 m (Figure 62b).

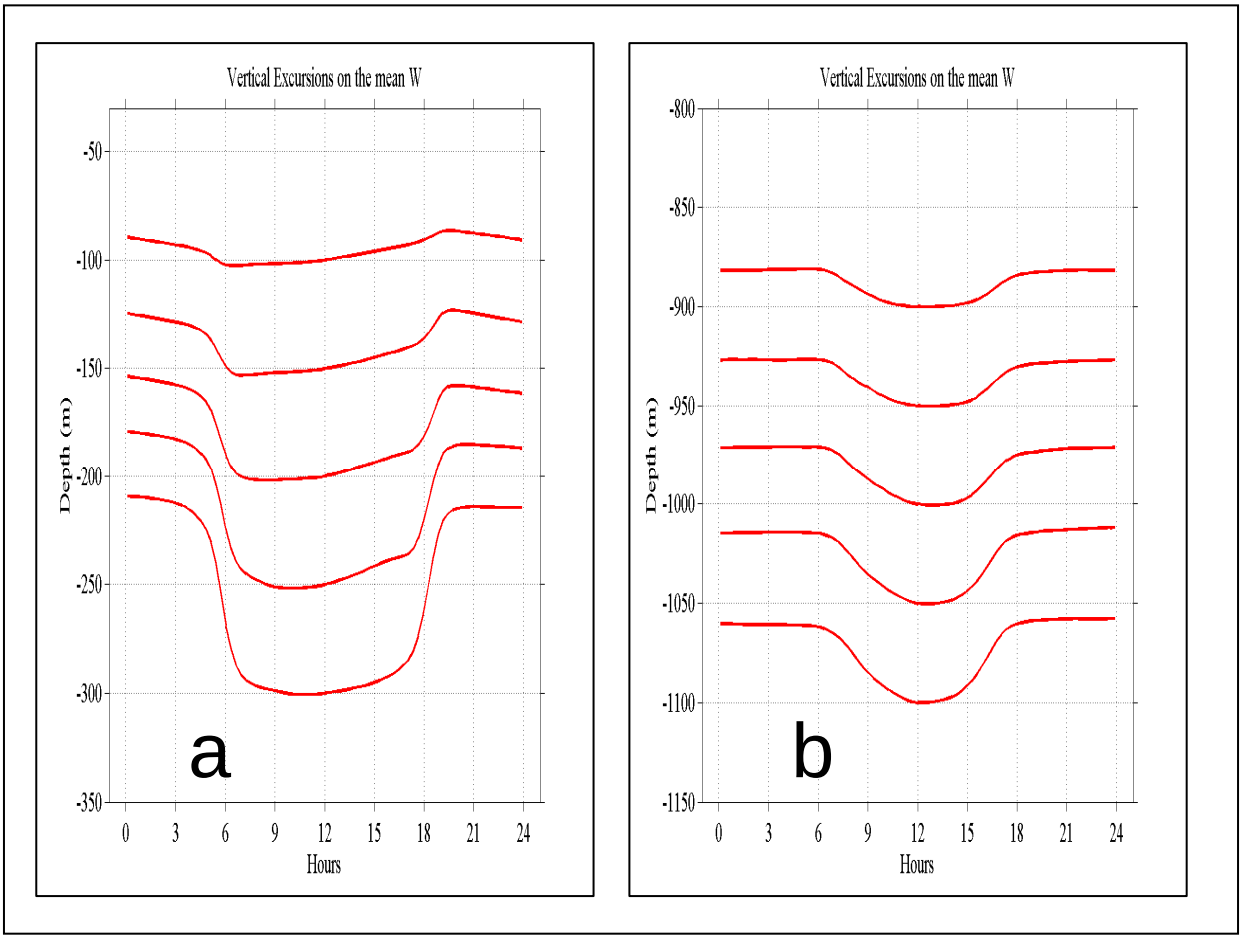

Figure 62. Mean vertical displacement as defined in the text, for the Canekito data. (a) the function for the near-surface region and (b) the function for the deep region.

7.4. DISCUSSION ON THE MEASURED DIEL MIGRATIONS FROM NEAR SURFACE TO 1,200 M DEPTH

The novel finding of these measurements is about the mean daily cycle in migrations as a function of depth, from the surface to 1200 m below. Before the advent of ADCPs, the vertical velocities in zooplankton migrating below 500 m were inferred, not measured. These include old conflicting inferences, for example: Angel *et al* (1982) argue that most of the species living at and below 1000 m show no diel migration, and Hu (1978) measured differences in stomach weight of euphausiids, as deep as 1100 m, inferring nocturnal (shallower) preferred feeding. In another examples, Andersen and Sardou (1992) and Andersen *et al* (1992) measured day to night concentrations differences in zooplankton catches by net tows, as deep as 1000 m, and inferred vertical excursions. Examples of recent measurements via ADCPs near or deeper than 1000 m are the studies of Van Haren (2007) and Kaltenberg *et al* (2007). The study of Van Haren (2007) showed the existence of daily, seasonal and monthly periodicities in ADCPs backscatter strength up to 1300 m deep. In the study of Kaltenberg *et al* (2007) the migration of deep scattering

layers (DSLs) in the Gulf of Mexico, for about 50 diel cycles, are analyzed. There is also theoretical studies that extend well-known hypothesis applicable in the euphotic zone; Putzeys and Hernández-León (2005) model the zooplankton migration cycle decaying in amplitude and without significant time delay up to a maximum depth of 1000 m. We find no single reference that specifies the mean diel migration below 600 m depth. The velocity measurements here presented show mean diel cycles up to 1200 m depth.

The deep diel cycle shows to be phase locked with the sunlight cycle, as is the better-studied migration at depths from 500 m to just below the surface. The measurements raise several questions, among them: 1) why does the downward/upward migration exists in the deep layers and starts delayed/earlier relative to the near surface layer? 2) Why does the echo intensity pattern in the deep layer shows so different behavior relative to the near surface layer? And 3) What signal is used for the circadian synchronization at depths near 1000 m? Table 2 summarizes some parameters of the mean diel cycle, in particular the timing of the peak migrations speed. It might be argued that the echo intensity difference (Figures 58 and 59) is due to turbulence caused by the swimming activity, which persists/declines for the deep/shallow fauna throughout the daylight phase of the cycle, rather than the concentration of the zooplankton.

Table 2

Listing of the Quadratic Fit of Time (with 06:00 Defining Sunrise and 18:00 Defining Sunset) at Maximum Migrating Speed Versus Depth for the Downward and Upward Phases of the Cycle.

Depth	Time at Maximum Downward Speed		Time at Maximum Upward Speed	
Meter	Hour	Min	Hour	Min
0	5	02	18	50
100	5	14	18	39
200	5	27	18	27
300	5	41	18	16
400	5	57	18	03
500	6	13	17	51
600	6	31	17	38
700	6	50	17	25
800	7	10	17	12
900	7	31	16	58
1000	7	54	16	44
1100	8	18	16	29
1200	8	42	16	14

In the euphotic zone, a main cue for circadian synchronization is known to be the sunlight cycle, but this cue is questionable at 1000 m depth. Bradner *et al* (1987) estimated a near noon downward radiation at 675 m depth of $1.4 \cdot 10^{-12}$ W/cm^2, and Young *et al* (1980) estimated that at 400 m depth the maximum sunlight radiation is $2.3 \cdot 10^{-8}$ W/cm^2, these values and the profiles of Young *et al* (1980) are consistent with an extinction coefficient (including absorption and scattering) of ~1/30 m and the measurements of Clarke and Kelly (1965). The radiation at depth is mostly composed by blue light (470±10 nm of wavelength in the vacuum, or $\sim 6.4 \cdot 10^{14}$ Hz in frequency) the color of less absorption in clear ocean waters. Assuming a greater water transparency with an extinction coefficient close to 1/50 m, which has been reported for deep sea

value (see among others Bolesta 1997; Capone *et al*. 2002; Riccobene *et al* 2007), these water properties imply that at noon in subtropical areas the daylight energy flux is close to 10^{-15} W/cm^2 at 1000 m. Even with a factor of 100 in error for such estimates, the daylight cycle amplitude is negligible small at 1000 m compared with anything above 500 meters. Fishes living deeper than 1000 m have eyes designed in relation to the surrounding bioluminescence not the sunlight (Land, 2000; Warrant, 2000). The general evidences favor that below 900-1000 m the daylight plays no role in the vision of fishes (Denton, 1990). Therefore, daylight is a questionable factor for the triggering or synchronization mechanism in the deep diel cycle.

The diel cycle, as defined by the measured velocity, has some slight asymmetries. For example, the maxima speed shows longer delays from shallow to deep levels in the downward migration than in the upward migration. In other words, the maxima speed when swimming upwards occurs with less time difference than when swimming downwards. In addition, during the downward phase, the shallower zooplankton starts earlier, and through the upward phase the deeper individuals start earlier, therefore there is a convergence of individuals in both phases. The black thin trace in Figure 63 is the cubic fit of the timing in maximum migration speed as a function of depth. Table 2 lists values of such times. Confidence intervals on the timing of maximum migration speed are ±9 and ±14 min at 80% and 95% levels. The extrapolations of such timings imply the collapse of migrations at ~2000 m, where the downward and upward migrations would occur at the same time; at ~13:00 hs.

The peak migration speed looked as a function of depth, shows two relative extremes, one at 250 m the other at 1100 m (Figure 64). This is a sign of an increased biological activity at such depths, the extreme at 1100 m probably related to deep scattering layers as described by Kaltenberg *et al* (2007).

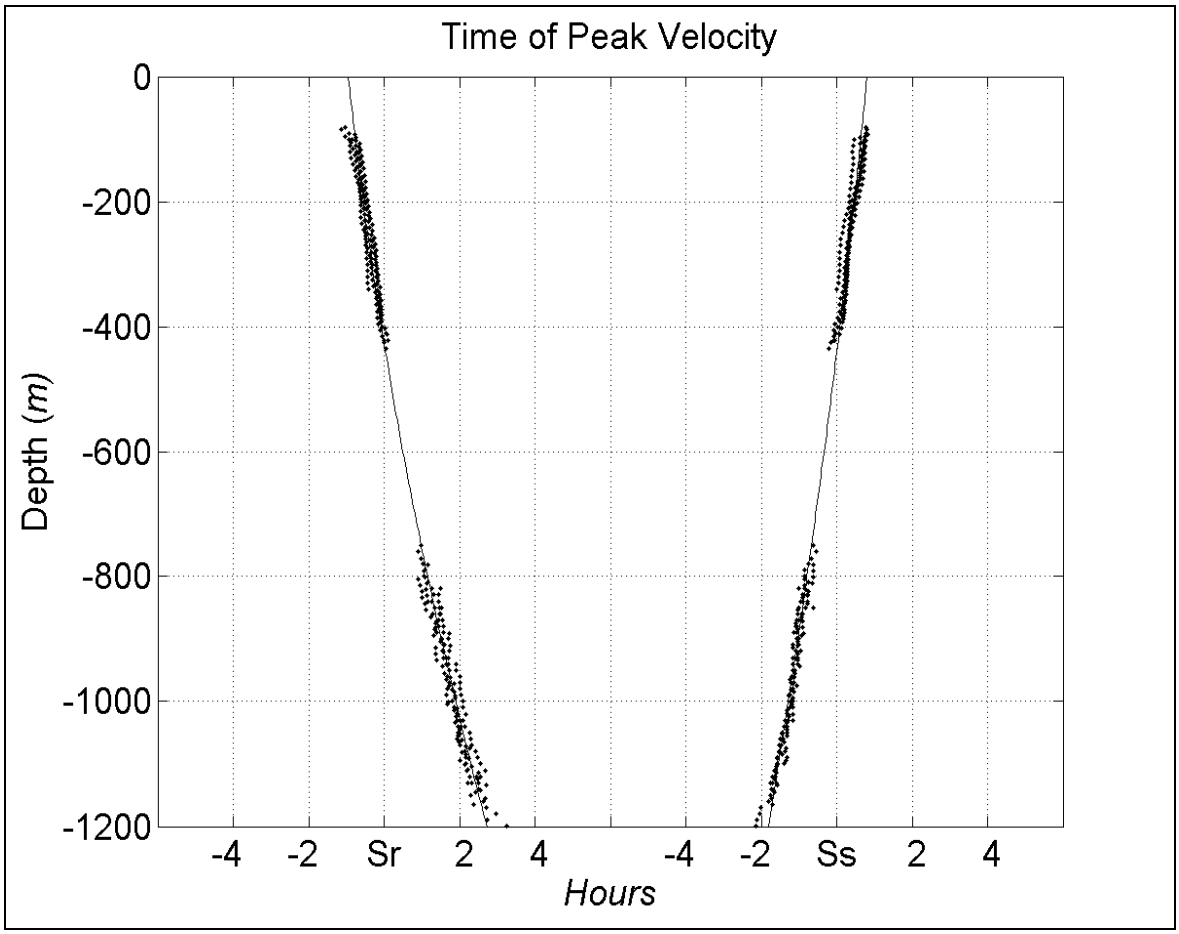

Figure 63. Plot shows, in the abscissa, the time in hours, relative to sunrise (Sr) and sunset (Ss) when the maxima in vertical migrating speed are reached at different depths in m, in the ordinate. The thin continuous trace is a fit of the form TM(z)=a0+a1z+a2z2 to the data shown as black dots.

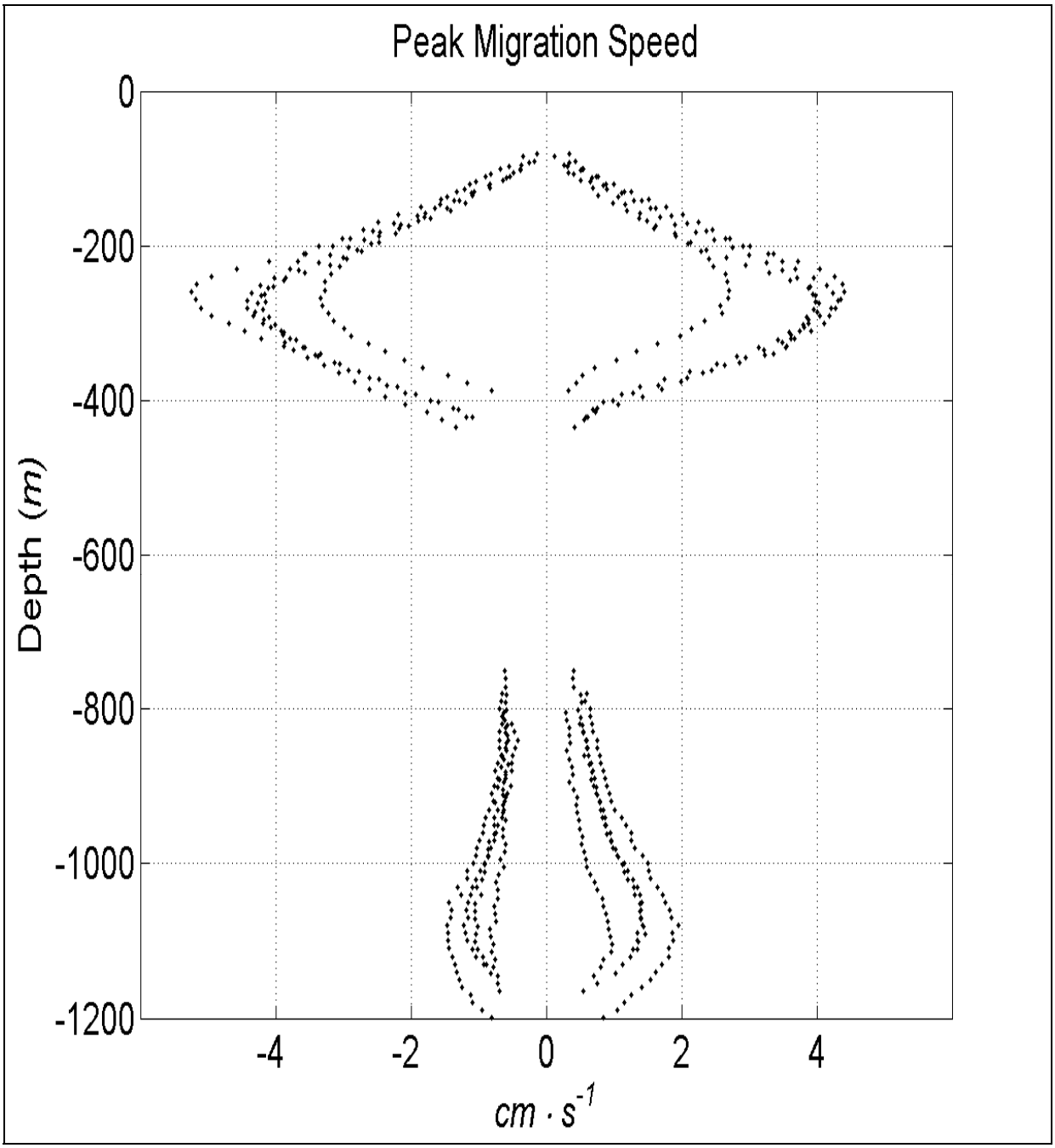

Figure 64. Peak velocities in the mean diel cycle, negative during the downward and positive during the upward. There are 4 deep and 5 near-surface ADCPs.

8. SUMMARY AND CONCLUSIONS

The high degree of consistency between the mooring observations and the altimetry data clearly indicate that flow variability in the study area is determined by the passage, formation, regeneration and dissipation of both cyclonic and anticyclonic eddies. Strong wind events do leave their signature (and may even be responsible for the formation of some of these eddies, see Donohue *et al*., 2008) but arrival of LC eddies, eddy-eddy and eddy-topography interactions appear to be the key features that explain many of the observations in the sense that every notable event can be traced to the presence of an eddy, cyclonic or anticyclonic.

Figure 65 provides a summary of the main eddy events detected at the moorings showing vector time series at 60 meters and around 800 m depth on the different moorings. LC eddies Titanic (T), Ulysses (U) and Vortex (V) impacted the mooring area at the beginning, middle part and end of the observational record (see Section 4). Cyclones C1 and C4 had very complicated histories since their generation, involving several intensification and merging events. They had a strong impact on the mooring observations. As discussed in Section 4, during September-October 2004, anticyclonic eddy Titanic affected the southern moorings 5 and 4 while cyclone C1 was over moorings 2 and 3. Late November marks the arrival of eddy Ulysses which was blocked by cyclone C1 and together with cyclone C5 (not shown in this Figure but see Section 4) split the eddy in two forming UlyssesS and UlyssesN eddies at the end of December 2004. Cyclonic circulation dominated the mooring area during January and February. In March eddy UlyssesS moves northward along the slope and UlyssesN stretches to the west so that by April the two branches merge again and for the following 7 months (until mid September) this "re-merged" eddy Ulysses defines the circulation over the array. Last three months of observations are marked by the presence of cyclone C4, the result of several merging events including cyclone C1, and the arrival of LC eddy Vortex.

Temperature time-series are highly coherent with altimetry data and therefore consistent with the eddy field (except for mooring 1) as discussed in Section 4. The most dramatic event captured by moorings 3, 4 and 5 is the warming associated with eddy Ulysses ("re-merged") which occurred during April 2005, as depicted in Figure 66 which shows temperature measurements from the different moorings at around 500 and 800 m depth. The warming signatures of LC Titanic and Ulysses at the end of 2004 and the cooling signal associated with cyclones can also be identified (see Section 4 for details).

Topography determines also the basic characteristics of the flow. Currents at mooring 1 on the shelf break are highly coherent on the top 300 m and also agree with eddy events when the altimetry suggests so. Below that depth, flow variability is different, and its basic dynamics not very clear. Mid-depth and near bottom intensified current events occur on this mooring (Section 4.2.1). Flow along the slope is sampled by moorings 2, 4 and 5. Currents are highly coherent in the top 1000-1200 m and show the signature of eddies. But the other feature seen in these 3 moorings is the southward bottom intensified mean along-slope flow (see Section 4). In contrast to other measurements however, there is no clear bottom intensification of the variability, which does not suggest the presence of strong topographic Rossby waves seen in other areas of the GoM along the slope (e.g. Hamilton, 2007, Oey and Lee, 2002, Rivas *et al*. 2008).

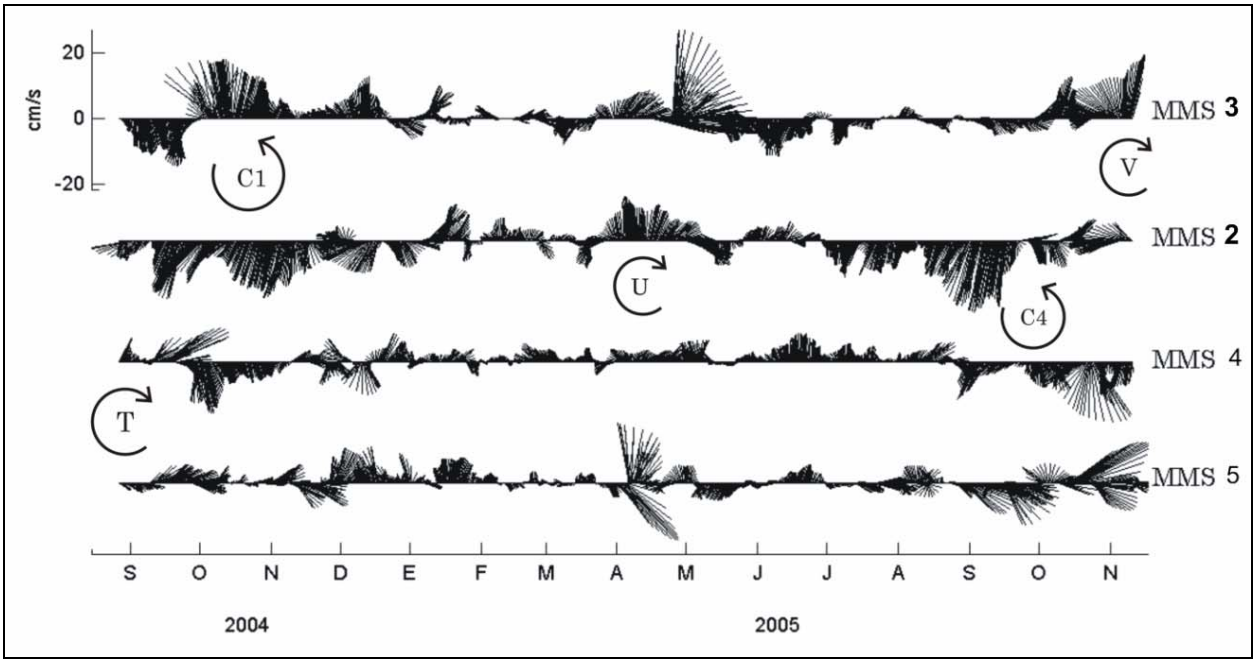

Figure 65. Vector time series for the abyssal (mooring 3) and along slope moorings (2, 4, and 5) showing LC eddies Titanic (T), Ulysses (U), and Vortex (V), and cyclones C1 and C4 (see Section 4).

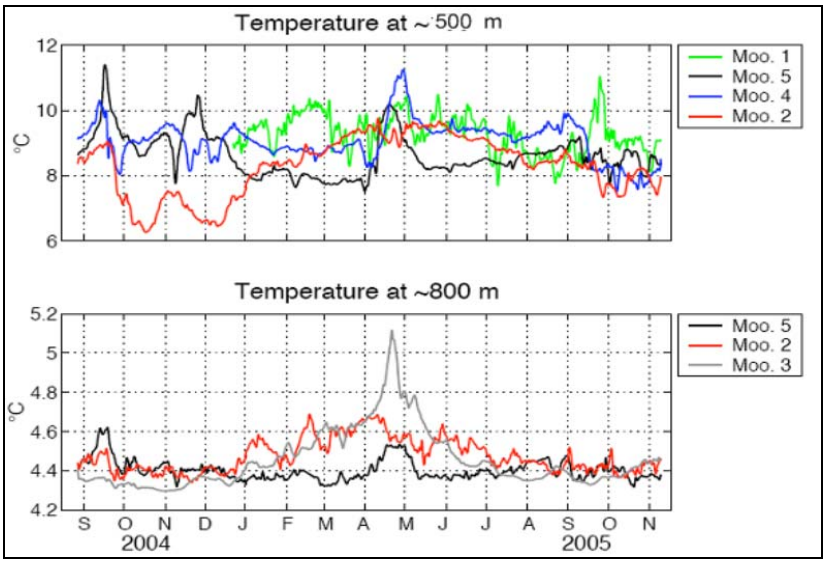

Figure 66. Temperature measurements at 500 and 800 m depth from all moorings with instruments at those depths. Observe the rapid warming event associated with eddy Ulysses in moorings 3, 4, and 5 during April 2005.

On the abyssal plane (mooring 3) the flow is very coherent from 800 m down to the bottom. The top ADCP on this mooring failed so there are no near surface observations. Comparison with surface geostrophic currents derived form altimetry, we found some eddy events reaching

all the way to the bottom and some others in which substantial veering of the current must occur between the surface and 800 m if one believes the surface geostrophic currents are correct. In contrast to along-slope moorings, no persistent southward flow is found on this mooring (Section 4, Figure 22).

High pass filtering the time series shows inertial and supra-inertial oscillations are present basically at all depths in the mooring observations. These high frequency motions are excited by strong wind events at the surface such as northern-winds or "Nortes" during winter and particularly by hurricane Emily which passed over the array on July 19-20 2005. However high frequency signals, particularly at depth, also seem highly correlated with eddy events. In some cases it may be argued the deep signals perhaps reflect vertical eddy-focusing (Kunze 1985) of wind generated inertial energy. But in other cases the high frequency variations just seem to be related to the eddies themselves. An interesting result is that all moorings show that the relative contribution of inertial and supra-inertial motions to total kinetic energy increases at depths between 1000 and 1500 m (see Sections 2 and 4). Whether this is related to eddy focusing of wind generated inertial energy or whether it is related to eddy interactions or instabilities remains to be found.

Rotary spectral analysis (Section 5) shows low frequency motions are the most energetic and also confirm the ubiquitous presence of inertial and higher frequency motions in all mooring sites. However, the analysis does not provide clear evidence of coherent signals among different moorings, except for a 20 day period signal between 800-1200 m depth along the slope (moorings 2 and 5), suggestive of a baroclinic Kelvin wave (Candela *et al* 2003); although much work still needs to be done to understand the character and details of this signal. There is also some coherence between moorings on the inertial frequency band though some times just above the significance level and with mixed results depending on the pair of moorings chosen for the analysis.

Strong vertical coherence is however found within each mooring consistent with the visual inspection of the vector time series (Section 4).

Complex Empirical Orthogonal Function analysis of the velocity anomalies carried out at each mooring (see Section 6) shows that the first two modes explain nearly 90-99% of the variance, with the first mode representing 79% to 90% of the variance and the second mode explaining between 5-13%. The vertical structure of the first mode is highly equivalent barotropic (i.e. surface intensified but unidirectional) and barotropic at mooring 3 which only accounts for currents below 800 m. Orthogonality constraints make the second mode look more baroclinic (i.e. with surface directions opposite to deeper ones). This is interesting considering that full vector time series at the moorings (Section 4, Figures 20-23) sometimes do show some veering of the current with depth. High amplitudes of the principal components associated with the vertical vector pattern are related, perhaps not surprisingly, to eddy events (e.g. eddy Ulysses, April 2005, just to highlight one the strong ones). In contrast, complex EOF analysis of the high-pass velocity fluctuations show that the first two modes explain less than 50% of the variance in the inertial-suprainertial band. Vertical structure as well as time dependence (see Section 6) is much noisier than more energetic EOFs just described, with substantial vertical veering and temporal fluctuations. These modes (their principal components) clearly highlight the periods when inertial energy is present and coincide with strong wind-forced events or .the presence of eddies.

The presence of eddies detected by altimetry data provides a clear framework to interpret the mooring observations and allows to explain the connection between observed currents at

different locations. However, such spatial and temporal coherence is very difficult to grasp with rotary spectra and horizontal EOF analysis (i.e. EOFs for all mooring data simultaneously): First, variability is event-driven and each event, even if it represents a similar feature such as a cyclone or anticyclone, varies from one another simply by the movement and orientation of such an eddy within the array. Second, this event-driven variability makes it difficult for global methods such as spectral analysis and horizontal EOFs, to identify similar eddy patterns in the whole time series, when we know each eddy will behave very differently during the record.

Finally, with regards to the vertical motion of zooplankton discussed in Section 7 the main conclusions are:

The deep diel cycle, near 1000 m below the surface, has slight differences with the better known migrations from the surface to 500 m below it. The mean cycle as a function of depth shows two relative maxima of vertical velocity: at 250 and 1100 m deep, a sign of localized biological control and vertical ecosystem structure. The downward phase of the migration is delayed in the deep, relative to the near surface, region. The peak downward velocity at 1100 m occurs 164 min after the same event at 250 m. The cycle is nearly symmetric to solar noon, with upward peak velocities happening earlier at depth, a pattern expected if the vertical migration was triggered by critical light level that reached the greater depth closer to noon. The peak upward velocity at 250 m occurs 33 min after sunset, but the same event at 1100 m happens earlier; 92 min before sunset. These delays imply that the shallower nightly stay is longer for the deep fauna than for the near surface. Although the migration velocities are about one fourth smaller at 1075 m relative to the ones at 475 m, the swimming time is during two short pulses in the upper layer compared with longer pulses in the deep. The higher echo intensity occurs during the swimming periods, regardless of depth or being upward or downward.

9. REFERENCES

Andersen, V. and J. Sardou. 1992. The diel migration and vertical distribution of zooplankton and micronekton in the Northwestern Mediterranean Sea. 1. Euphausiids, mysids, decapods and fishes. J. Plankton Res. 14:1129-1154.

Andersen, V., J. Sardou, and P. Nival. 1992. The diel migration and vertical distribution of zooplankton and micronekton in the Northwestern Mediterranean Sea. 2. Siphonophores, hydromedusae and pyrosomids. J. Plankton Res. 14:1155-1169.

Angel, M.V., P. Hargreaves, P. Kirkpatrick, and P. Domanski. 1982. Low variability in planktonic and micronektonic populations at 1,000 m depth in the vicinity of 42°N, 17°W; evidence against diel migratory behavior in the majority of species. Biol. Oceanogr. 1:287-319.

Bolesta, J.W. 1997. Upper limits to the diffuse neutrino emission from galactic nuclei. Ph.D. Thesis, University of Hawaii, Honolulu.

Bradner H., M. Bartlett, G. Blackinton, J. Clem, D. Karl, J. Learned, A. Lewitus, S. Matsuno, D. O'Connor, W. Peatman, M. Reichle, C. Roos, J. Waters, M. Webster, M. Yarbrough. 1987. Bioluminescence profile in the deep Pacific Ocean. Deep Sea Research. 34(11):1831-1840.

Candela, J., S. Tanahara, M. Crepon, B. Barnier, and J. Sheinbaum. 2003. Yucatán Channel flow: Observations versus CLIPPER ATL6 and MERCATOR PAM models. J. Geophys. Res. 108(C12):3385, doi:10.1029/2003JC001961.

Capone, A., T. Digaetano, A. Grimaldi, R. Habel, D. Lo Presti, E. Migneco, R. Masullo, F. Moro, M. Petruccetti, C. Petta, P. Piattelli, N.Randazzo, G. Riccobene, E. Salusti, P. Sapienza, M.Sedita, L. Trasatti, and L. Ursella. 2002. Measurements of light transmission in deep sea with the AC9 trasmissometer. Nuclear Instruments and Methods in Physical Research. A487:423-434.

Chassignet, E.P., H.E. Hurlburt, O.M. Smedstad, C.N. Barron, D.S. Ko, R.C. Rhodes, J.F. Shriver, A.J. Wallcraft, and R.A. Arnone. 2005. Assessment of data assimilative ocean models in the Gulf of Mexico using ocean color. In W. Sturges and A. Lugo-Fernández, eds. Circulation in the Gulf of Mexico: Observations and models. AGU Monograph No. 161. Pp. 87-100.

Clarke, G.L. and M.G. Kelly. 1965. Measurements of diurnal changes in bioluminescence from the sea surface to 2000 meters using a new photometric device. Limnology and Oceanology. 10:54-76.

Csanady, G.T. 1979. The birth and death of a warm core ring. J. Geophys. Res. 84:777-780.

Cushman-Roisin, B., B. Tang, and E.P. Chassignet. 1990. Westward Motion of Mesoscale Eddies. J. Phys. Oceanogr. 20:758–768.

DeHaan, C.J. and W. Sturges. 2005. Deep cyclonic circulation in the Gulf of Mexico. J. Phys. Oceanogr. 35(10):1801-1812.

Denton, E.J. 1990. Light and vision at depths greater than 200m. In Herring P.J., A.K. Campbell, M. Whitfield, and L. Maddock, eds. Light and life in the sea. Cambridge University Press, Cambridge, MA. Pp. 127-148.

DiMarco, S.F., R.O. Reid, W.D. Nowlin Jr. 2005. A statistical description of the near-surface velocity field from drifters in the Gulf of Mexico. In Sturges, W., and A. Lugo-Fernandez, eds. Circulation of the Gulf of Mexico: Observations and Models. Geophysical Monograph Series, Volume 161. American Geophysical Union. Pp. 101-110.

Donohue, K., P. Hamilton, R. Leben, R.Watts, and E. Waddell. 2008. Survey of deepwater currents in the northwestern Gulf of Mexico. Volume II: Technical report. U.S. Dept. of the Interior, Minerals Management Service, Gulf of Mexico OCS Region, New Orleans, LA. OCS Study MMS 2008-031. 375 pp.

Elliot, B.A. 1982. Anticyclonic rings in the Gulf of Mexico. J. Phys. Oceanogr. 12:1291-1309.

Flagg, C.N. and S.L. Smith. 1989. On the use of the acoustic Doppler current profiler to measure zooplankton abundance. Deep-Sea Res. 36:455-474.

Gonella, J. 1972. A rotary-component method for analyzing meteorological and oceanographic vector time series. Deep-Sea Res. 19:833–846.

Hamilton, P. 1990. Deep currents in the Gulf of Mexico. J. Phys. Oceanogr. 20:1087-1104.

Hamilton, P. 2007. Deep-current variability near the Sigsbee Escarpment in the Gulf of Mexico. J. Phys. Oceanogr. 37:708-726.

Hamilton, P. and A. Lugo-Fernández. 2001. Observations of high speed deep currents in the northern Gulf of Mexico. Geophys. Res. Letters. 28(14):2867-2870.

Hogg, N.G. 1991. Mooring motion corrections revisited. J. Atmos. Oceanic Technol. 8(2):289-295.

Hu, V.J.H. 1978. Relationships between vertical migration and diet in four species of Euphausiids. Limnology and Oceanography. 23(2):296-306.

Hurlburt, H. and J.D. Thompson. 1980. A numerical study of loop current intrusions and eddy shedding. J. Phys. Oceanogr. 10:1611–1651.

Hyun, K.H. and P.J. Hogan. 2008. Topographic effects on the path and evolution of loop current eddies. J. Geophys. Res., 113, C12026, doi:10.1029/2007JC004155.

Ichiye, T. 1962. Circulation and water mass distribution in the Gulf of Mexico. Geofis. lnt. 2: 47-76.

Itoh, S. and T. Sugimoto. 2001. Numerical experiments on the movement of a warm-core ring with the bottom slope of a western boundary. J. Geophys. Res. 106(C11):26,851-26,862.

Jiang, S., T.D. Dickey, D.K. Steinberg, and L.P. Madin. 2007. Temporal variability of zooplankton biomass from ADCP backscatter time series data at the Bermuda Testbed Mooring site. Deep-Sea Res. 54(4):608-636.

Kaltenberg, A.M., D.C. Biggs, and S.F. DiMarco. 2007. Deep scattering layers of the Northern Gulf of Mexico observed with a shipboard 38-kHz acoustic Doppler current profiler. Gulf Mex. Sci. 25(2):97-102.

Kunze, E. 1985. Near-inertial wave propagation in geostrophic shear. J. Phys. Oceanogr. 15:544-565.

Kunze, E. 1986. The mean and near-inertial velocity fields in a warm-core ring. J. Phys. Oceanogr. 16(8):1444-1461.

Land, M.F. 2000. On the functions of double eyes in midwater animals. Phil. Trans. R. Soc. Lond. B. 355:1147-1150.

Leben, R.R. 2005. Altimeter-derived loop current metrics. In: Sturges, W. and A. Lugo-Fernández, eds. Circulation in the Gulf of Mexico: Observations and models. AGU Monograph No. 161. Pp. 181-201.

Lewis, J.K., A.D. Kirwan, Jr., and G.Z. Forristall. 1989. Evolution of a warm-core ring in the Gulf of Mexico: Lagrangian observations. J. Geophys. Res. 94(C6):8163-8178.

Lohrmann, A., B. Hackett, and L.P. Røed. 1990. High resolution measurements of turbulence, velocity and stress using a Pulse-to-Pulse Coherent Sonar. J. Atmos. Oceanic Technol. 7:19-37.

Luo, J., P.B. Ortner, D. Forcucci, and S.R. Cummings. 2000. Diel vertical migration of zooplankton and mesopelagic fish in the Arabian Sea. Deep-Sea Res. II, 47:1451-1473.

Maximenko, N.A. and P.P. Niiler. 2004. Hybrid decade-mean global sea level with mesoscale resolution. In: N. Saxena, ed. Recent Advances in Marine Science and Technology. Honolulu: PACON International. Pp. 55-59.

Mooers, C.N.K. 1973. A technique for the cross spectrum analysis of pairs of complex-valued time series, with emphasis on properties of polarized components and rotational invariants. Deep-Sea Res. 20:1129–1141.

Morey, S.L., J. Zavala-Hidalgo, and J.J. O'Brien. 2005. The seasonal variability of continental shelf circulation in the northern and western Gulf of Mexico from a high-resolution numerical model. In Sturges, W. and A. Lugo-Fernandez, eds. New developments in the circulation of the Gulf of Mexico. Geophys. Mongr. Ser. 161. AGU, Washington, D. C. doi:10.1029/161GM16.

Nof, D. 1999. Strange encounters of eddies with walls. J. Mar. Res. 57:739–761.

Nowlin, W.D., Jr. and H. J. McLellan. 1967. A characterization of the Gulf of Mexico waters in winter. J. Mar. Res. 25:29-59.

Nowlin, W.D., Jr., D.F. Paskausky, and H.J. McLellan. 1969. Recent dissolved-oxygen measurements in the Gulf of Mexico deep waters. J. Mar. Res. 27:39-44.

Nowlin, W.D., A.E. Jochens, S.F. DiMarco, and R.O. Reid. 2000. Physical oceanography. In: Continental Shelf Associates, Inc., ed. Deepwater Gulf of Mexico environmental and socioeconomic data search and synthesis. Vol. 1: Narrative report. U.S. Department of the Interior, Minerals Management Service, Gulf of Mexico OCS Region, New Orleans, LA. OCS Study MMS 2000-049. 360 pp.

Oey, L.-Y. and H.-C. Lee. 2002. Deep eddy energy and topographic Rossby waves in the Gulf of Mexico. J. Phys. Oceanogr. 32:3499-3527.

Ott, M.W. 2005. The accuracy of acoustic vertical velocity measurements: Instrument biases and the Zooplankton migration. Cont. Shelf Res. 25(2):243-257.

Plueddemann, A.J. and R. Pinkel. 1989. Characterization of the pattern of diel migration using Doppler sonar. Deep-Sea Res. 36:509-530.

Pollard, R.T. 1970. On the generation by wind of inertial waves in the ocean. J. Mar. Res. 17:795-812.

Putzeys, S. and S. Hernández-León. 2005. A model of zooplankton diel vertical migration off the Canary Islands: Implication for active carbon flux. J. of Sea Res. 53:213-222.

RD Instruments. 1998. ADCP coordinate transformations. formulas and calculations. RDI Tech. Manual P/N 951-6079-00. 26 pp.

Record, N.R. and B. de Young. 2006. Patterns of diel vertical migration of zooplankton in acoustic Doppler velocity and backscatter data on the Newfoundland Shelf. Can. J. Fish. Aquat. Sci. 63:2708-2721.

Ricobenne, G., A. Capone, S. Aiello, M. Ambriola, F. Ameli, I. Amore, M. Anghinolfi, A. Anzalone, C. Avanzini, G. Barbarino, E. Barbarito, M. Battaglieri, R. Bellotti, N. Beverini, M. Bonori, B. Bouhadef, M. Brescia, G. Cacopardo, F. Cafagna, L. Caponetto, 2007. Deep seawater inherent optical properties in the Southern Ionian Sea. Astroparticle Physics. 27:1-9.

Rivas, D., A. Badan and J. Ochoa. 2005. The ventilation of the deep Gulf of Mexico. J. Phys. Oceanogr. 35:1763-1781.

Rivas, D., A. Badan, J. Sheinbaum, J. Ochoa, and J. Candela. 2008. Vertical velocity and vertical heat flux observed within loop current eddies in the Central Gulf of Mexico. J. Phys. Oceanogr. 38:2461-2481.

Roe, H.S.J., G. Griffiths, M. Hartman, and N. Crisp. 1996. Variability in biological distributions and hydrography from concurrent Acoustic Doppler Current Profiler and SeaSoar surveys. ICES J. of Mar. Sci. 53:131-138.

Schmitz, W. J., Jr. 2005. Cyclones and westward propagation in the shedding of anticyclonic rings from the Loop Current. In: W. Sturges and A. Lugo-Fernández, eds. Circulation in the Gulf of Mexico: Observations and models. AGU Monograph No. 161. Pp. 241-261.

Sturges, W. 1993. The annual cycle of the western boundary current in the Gulf of Mexico. J. Geophys. Res. 98(C10):18053-18068.

Sturges, W. 2005. Deep-water exchange between the Atlantic, Caribbean and Gulf of Mexico. In: W. Sturges and A. Lugo-Fernández, eds. Circulation in the Gulf of Mexico: Observations and models. AGU Monograph No. 161. Pp. 263-278.

Sturges, W. and J.P. Blaha. 1976. A western boundary current in the Gulf of Mexico. Science 192:367-369

Sturges, W. and R. Leben. 2000. Frequency of ring separations from the Loop Current in the Gulf of Mexico: A revised estimate. J. Phys. Oceanogr. 30(7):1814-1819.

Tarling, G.A., J.B.L. Matthews, P. David, O. Guerin and F. Buchholz, A.J., and R. Pinkel. 2001. The swarm dynamics of northern krill (Meganyctiphanes norvegica) and pteropods (Cavolinia inflexa) during vertical migration in the Ligurian Sea observed by an acoustic Doppler current profiler. Deep-Sea Res. 48:1671-1686.

Van Haren, H. 2007. Monthly periodicity in acoustic reflections and vertical motions in the deep ocean. Geophys. Res. Letters 34:L12603, doi:10.1029/2007GL029947.

Vidal, V.M.V., F.V. Vidal, A.F. Hernández, E.Meza, and J.M. Pérez-Molero. 1994. Baroclinic flows, transports, and kinematic properties in a cyclonic-anticyclonic-cyclonic ring triad in the Gulf of Mexico. J. Geophys. Res. 99(C4):7571-7597.

Vukovich, F.M. 1988. Loop Current Boundary Variations. J. Geophys. Res. 93(C12):15,585-15,591.

Vukovich, F.M. 1995. An updated evaluation of the Loop Current's eddy-shedding frequency. J. Geophys. Res. 100(C5):8655-8659.

Vukovich, F.M. 2007. Climatology of ocean features in the Gulf of Mexico using satellite remote sensing data. J. Phys. Oceanogr. 37(3):689, doi: 10.1175/JPO2989.1.

Vukovich, F.M., and B.W. Crissman. 1986. Aspects of warm rings in the Gulf of Mexico. J. Geophys. Res. 91(C2):2645-2660.

Vukovich, F.M. and E. Waddell. 1991. Interaction of a warm ring with the western slope in the Gulf of Mexico. J. Phys. Oceanogr. 21(7):1062-1074.

Warrant, E. 2000. The eyes of deep-sea fishes and the changing nature of visual scenes with depth. Phil. Trans. R. Soc. Lond. B. 355:1155-1159.

Weatherly, G.L., N. Wienders, and A. Romanou. 2005. Intermediate-depth circulation in the Gulf of Mexico estimated from direct measurements. In: Sturges, W. and A. Lugo-Fernández, eds. Circulation in the Gulf of Mexico: Observations and models. AGU Monograph No. 161. Pp. 315-324.

Weeks, A.R., G. Griffiths, H. Roe, G. Moore, I. S. Robinson, A. Atkinson, and R. Shreeved. 1995. The distribution of acoustic backscatter from zooplankton compared with physical structure, phytoplankton and radiance during the spring bloom in the Bellingshausen Sea. Deep-Sea Res. 42(4-5):997-1019.

Welsh, S. E. and M. Inoue. 2000. Loop Current rings and the deep circulation in the Gulf of Mexico. J. Geophys. Res. 105(C7):16951-16959.

Young, R.E., E.M. Kampa, S.D. Maynard, F.M. Mencher, and C.F.E. Roper. 1980. Counterillumination and the upper depth of midwater animals. Deep-Sea Res. 27:671-691.

Zavala-Sanson, L., F. Graef, and E. G. Pavía. 1998. Collision of anticyclonic, lens-like eddies with a meridional western boundary. J. Geophys. Res. 103(C11):24,881-24,890.

APPENDIX A. TABLES OF BASIC STATISTICS

Table A-1

Basic Statistics for Mooring 1.

Depth	mean u	std u	min u	max u	mean v	std v	min v	max v	MMS # of obs	**Sample interval**
55	6.8	15.7	-60.2	92.8	8.5	27.6	-72.3	130.9	14481	30
65	6.6	15.7	-54.3	87.5	8.2	27.3	-70.7	119.0	14481	30
75	6.4	15.3	-55.1	70.8	8.2	26.9	-66.8	90.2	14481	30
85	6.2	14.8	-47.2	74.3	8.5	26.5	-67.5	73.1	14481	30
95	6.1	14.4	-45.2	65.3	8.8	26.0	-64.9	74.4	14481	30
105	5.9	14.0	-48.9	68.2	8.7	25.6	-63.9	71.0	14481	30
115	5.6	13.5	-54.8	65.5	8.4	25.4	-71.0	77.7	14481	30
125	5.3	13.0	-49.8	73.9	8.0	25.0	-71.1	79.8	14481	30
135	5.0	5.0	5.0	5.0	5.0	24.6	-63.1	86.0	14481	30
145	4.8	11.9	-35.5	69.2	7.3	24.1	-62.3	70.4	14481	30
155	4.6	11.2	-31.3	62.8	7.3	23.8	-67.9	64.8	14481	30
165	4.5	10.8	-29.3	58.5	7.3	23.6	-75.2	60.6	14481	30
175	4.5	10.5	-28.7	49.4	7.2	23.3	-73.5	59.6	14481	30
185	4.1	10.2	-28.6	50.4	7.0	23.2	-74.9	58.4	14481	30
195	4.0	10.1	-31.5	44.5	6.7	23.1	-71.1	62.8	14481	30
205	3.8	9.8	-40.4	49.0	6.3	22.8	-68.8	57.5	14481	30
215	3.4	9.4	-33.1	42.9	6.1	22.6	-67.6	58.3	14481	30
225	3.1	8.9	-26.3	40.5	5.6	22.3	-62.7	56.9	14481	30
235	2.8	8.6	-26.0	42.3	5.1	22.0	-62.4	59.4	14481	30
245	2.5	8.2	-24.5	47.2	4.5	21.8	-63.0	59.2	14481	30
255	2.1	7.8	-27.0	39.6	4.0	21.4	-61.7	58.8	14481	30
265	1.9	7.4	-32.1	32.8	3.3	20.9	-60.1	55.5	14481	30
275	1.6	7.0	-28.8	28.4	2.7	20.5	-65.6	57.3	14481	30
285	1.4	6.6	-27.8	26.2	2.1	20.0	-63.1	55.7	14481	30
295	1.0	6.4	-25.0	25.5	1.4	19.5	-61.4	56.4	14481	30
305	0.9	6.1	-23.2	26.3	0.8	18.8	-61.7	55.3	14481	30
315	0.6	5.7	-21.4	26.7	0.1	18.1	-61.4	52.9	14481	30
325	0.4	5.5	-22.1	24.0	-0.5	17.4	-61.5	52.9	14481	30
335	0.2	5.2	-22.8	29.8	-1.0	16.7	-58.6	51.6	14481	30
345	0.0	5.0	-25.0	22.5	-1.5	16.0	-58.1	50.9	14481	30
355	-0.2	4.8	-20.2	19.8	-1.9	15.3	-58.0	50.3	14481	30
365	-0.3	4.6	-20.3	19.6	-2.2	14.5	-55.4	50.6	14481	30
375	-0.4	4.5	-19.3	17.8	-2.6	13.8	-52.1	43.1	14481	30
385	-0.6	4.3	-19.3	18.9	-2.8	12.9	-47.4	41.6	14481	30
395	-0.7	4.3	-18.9	17.0	-3.0	12.1	-43.0	39.5	14481	30
405	-0.7	4.1	-17.7	19.2	-3.1	11.1	-41.5	39.4	14481	30
415	-0.7	4.1	-17.6	20.0	-3.3	10.0	-37.8	37.1	14481	30
425	-0.6	4.0	-17.8	14.9	-3.1	8.7	-36.0	31.6	14481	30

Table A-2

Basic Statistics for Mooring 2**.**

Depth	Mean u	Std u	Min u	Max u	Mean v	Std v	Min v	Max v	MMS # of Obs	Sample Interval
45	6.0	26.2	-68.0	102.4	-2.4	33.1	-97.9	115.8	21126	30
55	6.0	25.9	-68.8	103.6	-2.1	32.6	-95.8	117.5	21126	30
65	6.0	25.5	-70.3	104.6	-1.6	32.0	-91.4	115.8	21126	30
75	5.9	25.1	-72.0	102.3	-1.3	31.1	-92.1	121.3	21126	30
85	5.6	24.5	-73.6	102.5	-1.1	30.2	-86.5	119.3	21126	30
95	5.3	23.8	-67.7	100.7	-1.0	29.2	-83.7	111.1	21126	30
105	4.9	23.0	-57.8	97.3	-1.2	28.1	-74.5	100.5	21126	30
115	4.5	22.2	-53.3	99.6	-1.3	26.8	-74.7	98.3	21126	30
125	4.1	21.3	-51.7	95.0	-1.5	25.8	-71.0	92.3	21126	30
135	3.8	20.6	-51.3	90.6	-1.7	24.8	-68.5	85.6	21126	30
145	3.5	19.8	-50.6	84.7	-2.0	23.8	-69.6	80.7	21126	30
155	3.2	19.1	-50.3	81.7	-2.4	22.9	-68.4	72.5	21126	30
165	2.8	18.5	-49.1	80.2	-2.6	22.2	-64.8	70.1	21126	30
175	2.6	18.0	-49.9	71.3	-2.8	21.5	-62.2	64.9	21126	30
185	2.4	17.5	-52.4	69.6	-2.9	20.9	-61.1	63.6	21126	30
195	2.2	16.9	-53.8	68.9	-3.1	20.3	-60.6	61.9	21126	30
205	1.9	16.5	-50.8	64.7	-3.1	19.7	-60.5	58.2	21126	30
215	1.7	16.0	-48.8	64.7	-3.1	19.1	-60.9	58.9	21126	30
225	1.6	15.7	-49.1	58.5	-3.2	18.6	-57.3	54.4	21126	30
235	1.4	15.3	-48.4	56.4	-3.3	18.1	-55.2	52.2	21126	30
245	1.3	15.0	-48.4	57.6	-3.4	17.8	-58.2	50.8	21126	30
255	1.2	14.6	-49.2	57.0	-3.4	17.4	-61.3	49.4	21126	30
265	1.1	14.4	-47.3	52.5	-3.5	17.1	-57.0	47.2	21126	30
275	1.1	14.1	-45.6	52.5	-3.5	16.7	-57.7	47.8	21126	30
285	1.0	13.8	-46.7	51.8	-3.7	16.4	-55.5	44.1	21126	30
295	0.8	13.5	-47.5	48.5	-3.7	16.1	-54.7	42.0	21126	30
305	0.7	13.2	-45.3	46.7	-3.6	15.9	-53.6	38.5	21126	30
315	0.7	13.0	-45.4	44.1	-3.6	15.6	-54.3	41.4	21126	30
325	0.6	12.7	-42.8	41.7	-3.5	15.3	-52.5	38.2	21126	30
335	0.6	12.5	-44.5	40.7	-3.4	15.1	-50.4	38.6	21126	30
345	0.5	12.4	-44.8	43.1	-3.5	14.8	-51.1	39.3	21126	30
355	0.5	12.2	-44.3	41.2	-3.5	14.6	-49.6	36.9	21126	30
365	0.5	11.9	-41.2	40.9	-3.5	14.4	-47.7	36.2	21126	30
375	0.4	11.7	-43.8	42.8	-3.5	14.1	-45.6	35.5	21126	30
385	0.3	11.5	-41.3	41.3	-3.5	13.8	-47.5	37.7	21126	30
395	0.3	11.3	-41.5	42.7	-3.5	13.5	-44.6	34.7	21126	30
405	0.2	11.0	-42.8	42.9	-3.5	13.3	-44.4	33.1	21126	30
415	0.2	10.8	-38.9	40.5	-3.4	13.0	-40.8	32.7	21126	30
425	0.1	10.6	-40.2	36.7	-3.4	12.8	-41.7	31.9	21126	30
435	0.1	10.3	-40.3	34.1	-3.4	12.5	-41.8	33.4	21126	30
445	0.1	10.2	-40.4	33.7	-3.4	12.3	-40.6	34.0	21126	30
455	0.1	10.0	-40.4	35.1	-3.3	12.1	-41.0	31.5	21126	30
465	0.0	9.7	-36.1	33.4	-3.4	11.8	-42.4	29.5	21126	30
475	0.0	9.4	-35.2	33.4	-3.3	11.6	-39.3	29.0	21126	30
485	-0.1	9.1	-33.4	32.7	-3.3	11.2	-37.9	28.8	21126	30
495	-0.1	8.6	-35.1	32.4	-3.2	10.6	-37.3	31.1	21126	30

Table A-2 Basic Statistics for Mooring 2 (continued).

Depth	Mean u	Std u	Min u	Max u	Mean v	Std v	Min v	Max v	MMS # of Obs	Sample Interval
732	-0.7	5.6	-24.3	15.8	-2.9	7.0	-30.6	16.1	10562	60
730	-0.8	6.4	-26.1	21.1	-3.2	7.7	-35.1	23.7	21125	30
740	-0.8	6.4	-30.0	20.4	-3.2	7.6	-30.3	23.6	21125	30
750	-0.9	6.2	-28.8	20.9	-3.2	7.5	-34.6	21.8	21125	30
760	-0.9	6.2	-25.9	20.4	-3.2	7.4	-30.8	20.1	21125	30
770	-1.0	6.1	-27.2	19.1	-3.2	7.3	-31.7	19.4	21125	30
780	-1.0	6.0	-26.9	19.5	-3.2	7.3	-31.3	20.3	21125	30
790	-1.1	6.0	-25.4	19.2	-3.1	7.2	-30.4	21.0	21125	30
800	-1.1	5.9	-25.3	22.0	-3.0	7.1	-33.5	21.2	21125	30
810	-1.1	5.9	-24.2	19.6	-3.0	7.1	-30.4	19.5	21125	30
820	-1.1	5.8	-24.9	19.6	-3.1	7.0	-34.3	21.8	21125	30
830	-1.2	5.8	-26.2	20.3	-3.1	7.0	-32.7	19.8	21125	30
840	-1.2	5.8	-27.7	20.1	-3.1	6.9	-32.3	19.0	21125	30
850	-1.2	5.7	-23.5	18.5	-3.1	6.9	-30.8	18.2	21125	30
860	-1.2	5.6	-22.9	20.4	-3.2	6.8	-30.9	19.2	21125	30
870	-1.3	5.6	-25.1	18.0	-3.2	6.8	-29.2	20.2	21125	30
880	-1.3	5.6	-23.8	18.1	-3.2	6.7	-31.2	18.4	21125	30
890	-1.3	5.5	-24.4	18.5	-3.3	6.7	-31.8	17.2	21125	30
900	-1.3	5.5	-23.3	17.8	-3.3	6.6	-32.3	16.7	21125	30
910	-1.4	5.5	-25.9	18.1	-3.3	6.7	-32.0	17.8	21125	30
920	-1.4	5.5	-23.9	17.4	-3.3	6.7	-34.5	17.8	21125	30
930	-1.4	5.4	-23.4	18.4	-3.4	6.7	-34.9	17.8	21125	30
940	-1.5	5.3	-25.4	19.1	-3.4	6.6	-34.4	20.2	21125	30
950	-1.4	5.2	-26.2	19.5	-3.4	6.5	-34.6	17.8	21125	30
960	-1.5	5.2	-27.1	18.8	-3.4	6.5	-33.7	16.0	21125	30
970	-1.5	5.2	-26.1	20.8	-3.4	6.4	-33.3	17.1	21125	30
980	-1.5	5.2	-26.5	17.9	-3.4	6.3	-31.3	16.8	21125	30
990	-1.5	5.2	-26.5	17.3	-3.3	6.3	-30.2	17.8	21125	30
1000	-1.5	5.1	-24.6	18.3	-3.3	6.2	-30.9	16.6	21125	30
1010	-1.6	5.1	-30.0	17.3	-3.3	6.2	-30.8	19.9	21125	30
1020	-1.6	5.1	-25.3	16.4	-3.4	6.1	-31.5	16.7	21125	30
1030	-1.6	5.0	-27.5	16.9	-3.3	6.1	-30.5	16.7	21125	30
1040	-1.6	5.0	-25.9	17.8	-3.3	6.0	-31.4	16.8	21125	30
1050	-1.6	5.0	-25.0	21.1	-3.3	6.0	-27.9	15.5	21125	30
1060	-1.6	4.9	-23.3	21.2	-3.3	5.9	-28.4	15.4	21125	30
1070	-1.6	4.9	-24.2	18.4	-3.3	6.0	-26.5	18.2	21125	30
1080	-1.6	4.8	-21.9	19.6	-3.3	5.8	-27.3	16.4	21125	30
1090	-1.6	4.9	-21.2	17.5	-3.3	5.8	-28.1	15.9	21125	30
1100	-1.7	4.8	-21.8	19.1	-3.3	5.8	-35.5	16.2	21125	30
1110	-1.7	4.8	-21.9	18.1	-3.2	5.7	-29.6	16.4	21125	30
1120	-1.7	4.8	-22.0	18.5	-3.2	5.7	-24.6	15.8	21125	30
1130	-1.7	4.7	-22.1	16.9	-3.2	5.6	-26.0	16.1	21125	30
1140	-1.6	4.6	-22.1	15.1	-3.2	5.6	-25.3	18.1	21125	30
1150	-1.6	4.5	-22.8	17.1	-3.1	5.3	-23.5	17.1	21125	30
1160	-1.7	4.4	-22.8	16.6	-3.0	5.1	-23.3	14.6	21125	30
1170	-1.5	4.4	-25.2	15.4	-3.0	5.1	-22.2	16.7	21125	30

Table A-2 Basic Statistics for Mooring 2 (continued).

depth	mean u	std u	min u	max u	mean v	std v	min v	max v	MMS # of obs	Sample interval
1544	-2.2	3.5	-16.3	9.2	-3.5	4.0	-24.9	6.2	10562	60
1957	-1.9	3.7	-23.2	22.7	-6.3	5.6	-24.8	16.8	21125	30
1965	-1.9	3.4	-22.5	23.1	-6.3	5.4	-25.1	12.4	21125	30
1973	-1.8	3.3	-22.2	23.7	-6.4	5.3	-26.1	12.5	21125	30
1981	-1.7	3.3	-21.6	23.6	-6.4	5.3	-25.1	11.3	21125	30
1989	-1.6	3.3	-23.0	24.4	-6.5	5.3	-25.4	10.7	21125	30
1997	-1.5	3.3	-23.0	25.7	-6.4	5.2	-25.8	10.0	21125	30
2005	-1.4	3.3	-22.4	25.5	-6.2	5.0	-26.5	9.9	21125	30
2013	-1.2	3.1	-22.5	24.7	-5.7	4.7	-26.6	9.2	21125	30
2021	-0.7	3.0	-20.9	24.2	-4.1	4.4	-24.8	9.5	21125	30

Table A-3

Basic Statistics Mooring for 3.

Depth	Mean u	Std u	Min u	Max u	Mean v	Std v	Min v	Max v	Mms # of Obs	Sample Interval
820	1.1	5.5	-21.9	31.6	0.1	6.3	-18.2	26.9	8862	60
767	1.6	6.8	-28.8	40.8	0.5	8.0	-28.5	32.7	21142	30
777	1.6	6.8	-30.2	41.4	0.5	7.8	-27.6	36.4	21142	30
787	1.5	6.8	-29.3	39.7	0.5	7.8	-27.5	33.6	21142	30
797	1.5	6.7	-27.2	36.9	0.5	7.7	-23.0	32.9	21142	30
807	1.5	6.7	-28.9	35.9	0.5	7.5	-24.0	31.5	21142	30
817	1.4	6.6	-25.3	35.7	0.6	7.5	-22.3	31.5	21142	30
827	1.3	6.6	-27.8	40.1	0.7	7.4	-22.6	32.3	21142	30
837	1.3	6.6	-30.1	36.2	0.7	7.4	-22.0	35.2	21142	30
847	1.2	6.6	-27.4	37.7	0.7	7.3	-23.3	31.6	21142	30
857	1.2	6.6	-26.9	36.9	0.7	7.2	-23.6	32.3	21142	30
867	1.1	6.6	-26.8	39.2	0.7	7.2	-24.7	31.6	21142	30
877	1.0	6.6	-23.9	39.3	0.7	7.1	-23.8	32.7	21142	30
887	1.0	6.5	-24.1	37.3	0.7	7.1	-22.0	34.6	21142	30
897	0.9	6.5	-23.6	36.0	0.8	7.0	-21.2	35.0	21142	30
907	0.9	6.5	-21.3	35.5	0.8	7.0	-21.3	35.7	21142	30
917	0.8	6.4	-20.8	37.8	0.8	6.9	-23.8	33.5	21142	30
927	0.8	6.3	-19.8	36.5	0.8	6.8	-21.0	35.2	21142	30
937	0.8	6.3	-20.4	39.8	0.8	6.7	-20.4	34.3	21142	30
947	0.7	6.3	-21.3	37.8	0.8	6.7	-22.0	34.4	21142	30
957	0.7	6.3	-20.5	38.3	0.8	6.6	-20.9	37.2	21142	30
967	0.6	6.3	-20.3	37.2	0.9	6.5	-20.8	32.9	21142	30
977	0.6	6.3	-21.7	37.2	0.9	6.5	-20.5	32.2	21142	30
987	0.5	6.2	-21.4	36.1	0.9	6.4	-18.8	31.4	21142	30
997	0.4	6.2	-20.6	35.0	0.9	6.5	-20.2	33.0	21142	30
1007	0.4	6.1	-20.2	36.4	0.9	6.5	-18.7	33.0	21142	30
1017	0.4	6.1	-21.0	38.8	0.9	6.4	-20.9	32.7	21142	30
1027	0.4	6.1	-19.0	39.2	0.9	6.4	-23.2	33.3	21142	30
1047	0.3	6.0	-20.4	33.4	0.9	6.2	-19.5	34.6	21142	30

Table A-3 Basic Statistics Mooring for 3.

Depth	Mean u	Std u	Min u	Max u	Mean v	Std v	Min v	Max v	MMS # of Obs	Sample Interval
1057	0.3	6.0	-20.1	33.8	0.9	6.1	-20.6	31.2	21142	30
1067	0.2	5.9	-19.1	35.7	0.9	6.2	-21.6	27.2	21142	30
1077	0.2	5.9	-20.8	33.2	0.9	6.1	-21.7	28.4	21142	30
1087	0.2	5.9	-21.0	34.1	0.9	6.0	-23.3	29.9	21142	30
1097	0.2	5.9	-19.6	36.6	0.9	6.0	-22.6	32.2	21142	30
1107	0.1	5.9	-21.8	33.4	0.9	6.1	-21.9	30.5	21142	30
1117	0.1	5.8	-20.6	35.5	0.9	6.0	-22.1	32.1	21142	30
1127	0.0	5.8	-20.9	28.3	0.9	6.0	-20.3	27.8	21142	30
1137	0.0	5.8	-20.1	30.3	0.8	6.0	-23.6	25.8	21142	30
1147	-0.1	5.8	-20.4	31.0	0.8	6.0	-23.3	27.4	21142	30
1157	-0.1	5.8	-21.2	30.8	0.8	5.9	-23.2	26.1	21142	30
1167	-0.1	5.7	-20.5	32.0	0.8	5.9	-21.3	22.6	21142	30
1177	-0.2	5.7	-23.4	29.7	0.8	5.9	-22.4	24.3	21142	30
1187	-0.2	5.7	-20.4	32.4	0.8	5.8	-21.2	25.1	21142	30
1197	-0.2	5.6	-24.3	31.6	0.7	5.8	-20.8	30.8	21142	30
1207	-0.2	5.5	-21.6	31.2	0.8	5.6	-24.7	26.0	21142	30
1217	-0.2	5.4	-19.2	30.5	0.7	5.5	-20.3	30.7	21142	30
1541	-0.8	4.3	-18.0	15.3	0.7	4.3	-18.5	16.7	10561	60
2048	-0.9	4.7	-19.0	14.9	0.7	4.6	-21.1	16.6	10561	60
2556	-0.6	3.2	-12.2	11.2	0.4	4.1	-10.4	12.8	4640	60
3038	-1.0	5.0	-17.8	16.3	0.8	5.2	-21.0	19.6	10561	60
3510	-1.1	5.5	-19.8	17.0	0.9	5.7	-21.1	20.5	21142	30
3518	-1.1	5.4	-19.4	16.6	0.9	5.6	-22.1	20.1	21142	30
3526	-1.1	5.3	-19.4	16.2	0.9	5.5	-21.1	19.7	21142	30
3534	-1.1	5.2	-18.7	15.9	0.9	5.5	-20.4	19.9	21142	30
3542	-1.0	4.9	-17.7	16.1	0.8	5.2	-19.5	19.8	21142	30
3550	-0.9	4.5	-17.5	15.3	0.7	4.8	-19.9	19.9	21142	30
3558	-0.1	4.5	-18.9	15.5	2.2	4.9	-19.8	20.7	21142	30

Table A-4

Basic Statistics for Mooring 4.

Depth	Mean u	Std u	Min u	Max u	Mean v	Std v	Min v	Max v	MMS# of Obs	Sample Interval
50	12.3	27.7	-109.0	154.0	6.4	20.8	-78.8	104.1	21199	30
60	12.0	27.1	-102.6	158.5	6.1	20.3	-79.4	94.6	21199	30
70	11.7	26.4	-97.8	148.4	6.0	19.7	-73.5	77.8	21199	30
80	11.4	25.6	-91.3	140.8	5.9	19.0	-64.4	74.8	21199	30
90	11.0	24.6	-77.3	144.2	5.7	18.4	-62.9	71.6	21199	30
100	10.6	23.6	-56.6	132.8	5.5	17.7	-63.7	67.0	21199	30
110	10.2	22.5	-48.9	120.8	5.1	17.0	-65.2	62.9	21199	30
120	9.8	21.3	-49.7	111.4	4.9	16.2	-62.8	56.5	21199	30
130	9.2	20.1	-50.9	105.6	4.6	15.6	-55.1	59.3	21199	30
140	8.7	19.1	-42.1	104.5	4.3	14.9	-49.2	50.6	21199	30
150	8.2	18.2	-39.1	98.7	4.0	14.3	-47.7	47.1	21199	30
160	7.6	17.3	-35.1	92.5	3.8	13.7	-45.8	48.0	21199	30
170	7.1	16.3	-35.8	93.7	3.5	13.1	-40.9	46.2	21199	30
180	6.7	15.5	-32.5	90.7	3.2	12.7	-41.3	44.4	21199	30
190	6.3	14.7	-36.0	81.0	2.9	12.2	-40.2	41.4	21199	30
200	5.9	14.0	-33.8	73.6	2.7	11.8	-38.8	41.4	21199	30
210	5.6	13.4	-32.6	67.1	2.5	11.5	-40.1	37.4	21199	30
220	5.4	12.9	-30.9	65.2	2.2	11.2	-38.5	36.5	21199	30
230	5.1	12.5	-30.9	59.0	2.0	10.9	-38.4	34.4	21199	30
240	4.9	12.1	-28.0	56.4	1.9	10.6	-40.9	37.1	21199	30
250	4.7	11.7	-28.2	56.2	1.7	10.5	-40.2	42.7	21199	30
260	4.5	11.3	-30.1	54.0	1.6	10.4	-38.5	45.4	21199	30
270	4.3	11.0	-28.2	50.1	1.5	10.2	-36.3	44.9	21199	30
280	4.2	10.7	-26.5	54.9	1.4	10.1	-37.5	43.6	21199	30
290	4.1	10.4	-26.5	48.3	1.4	9.8	-33.4	39.3	21199	30
300	3.9	10.2	-30.4	46.3	1.3	9.7	-34.0	43.5	21199	30
310	3.8	9.8	-27.4	47.4	1.3	9.5	-36.9	45.1	21199	30
320	3.7	9.6	-24.7	43.7	1.2	9.4	-31.2	47.2	21199	30
330	3.6	9.4	-23.5	44.7	1.1	9.3	-33.4	46.1	21199	30
340	3.4	9.2	-27.0	43.3	1.2	9.2	-33.0	47.2	21199	30
350	3.2	9.1	-25.0	39.6	1.1	9.1	-32.1	48.7	21199	30
360	3.1	8.8	-23.8	39.2	1.1	9.0	-33.9	47.4	21199	30
370	3.0	8.6	-23.5	41.7	1.0	9.0	-31.7	47.1	21199	30
380	2.9	8.4	-24.8	39.2	1.0	8.9	-34.4	44.3	21199	30
390	2.8	8.3	-24.8	38.4	0.9	8.8	-31.5	44.8	21199	30
400	2.8	8.1	-21.9	36.8	0.9	8.8	-31.5	46.6	21199	30
410	2.8	8.0	-22.3	34.1	0.9	8.6	-30.7	38.3	21199	30
420	2.7	8.0	-21.8	34.9	0.8	8.5	-31.3	37.3	21199	30
430	2.7	7.8	-23.9	35.6	0.7	8.5	-31.0	37.4	21199	30
440	2.6	7.8	-24.9	35.6	0.7	8.4	-31.3	33.6	21199	30
450	2.5	7.6	-22.9	34.8	0.6	8.3	-31.6	34.0	21199	30
460	2.4	7.5	-22.7	36.7	0.5	8.2	-30.2	31.5	21199	30
470	2.3	7.3	-22.0	33.8	0.5	8.0	-29.2	30.2	21199	30
480	2.2	7.0	-23.3	31.7	0.3	7.7	-29.2	31.7	21199	30
708	0.5	4.8	-17.3	21.3	-0.4	5.6	-22.5	16.0	10599	60

Table A-4 Basic Statistics for Mooring 4 (continued)

Depth	Mean u	Std u	Min u	Max u	Mean v	Std v	Min v	Max v	MMS# of Obs	Sample Interval
1572	-2.1	2.8	-16.1	7.3	-2.3	3.3	-17.6	11.2	10599	60
1941	-0.7	3.1	-13.2	13.7	-1.3	3.0	-12.7	15.9	21199	30
1949	-0.6	3.1	-12.5	14.5	-1.3	2.9	-13.0	15.1	21199	30
1957	-0.5	3.1	-12.5	14.4	-1.2	2.9	-12.3	15.1	21199	30
1965	-0.4	3.2	-12.3	14.4	-1.2	2.9	-12.6	14.9	21199	30
1973	-0.3	3.1	-12.1	13.5	-1.1	2.8	-12.2	14.5	21199	30
1981	-0.1	3.0	-12.3	13.8	-1.0	2.7	-13.4	15.2	21199	30
1989	0.2	2.8	-12.1	11.6	-0.9	2.4	-12.1	14.2	21199	30

Table A-5 Basic Statistics for Mooring 5.

Depth	Mean u	Std u	Min u	Max u	Mean v	Std v	Min v	Max v	MMS# of Obs	Sample Interval
45	18.1	25.5	-53.9	113.9	10.3	14.6	-48.4	110.2	21239	30
55	18.7	26.0	-43.6	117.2	10.3	14.6	-52.1	108.3	21239	30
65	19.2	26.3	-51.7	108.8	10.3	14.6	-53.3	104.9	21239	30
75	19.3	26.4	-48.1	115.3	10.2	14.6	-60.3	101.5	21239	30
85	19.2	26.2	-38.9	117.2	10.0	14.5	-54.8	89.2	21239	30
95	18.8	25.7	-36.3	111.5	9.6	14.3	-56.1	82.3	21239	30
105	18.3	25.1	-34.4	110.1	9.3	14.0	-53.7	74.7	21239	30
115	17.7	24.2	-32.5	102.5	9.1	13.6	-54.5	68.1	21239	30
125	17.0	23.3	-33.8	95.4	8.8	13.2	-52.6	65.6	21239	30
135	16.4	22.2	-30.6	90.1	8.3	12.7	-53.1	61.5	21239	30
145	15.6	21.2	-30.5	81.6	7.9	12.1	-49.0	57.3	21239	30
155	14.9	20.4	-28.4	82.5	7.4	11.6	-44.6	53.4	21239	30
165	14.3	19.7	-28.0	80.6	7.0	11.2	-40.9	52.4	21239	30
175	13.8	19.1	-28.5	80.9	6.6	11.0	-38.5	52.7	21239	30
185	13.3	18.6	-27.9	78.8	6.2	10.8	-36.2	53.6	21239	30
195	12.8	18.0	-33.5	78.9	6.0	10.6	-33.7	59.4	21239	30
205	12.3	17.6	-26.6	72.3	5.7	10.4	-36.8	60.8	21239	30
215	11.9	17.1	-31.5	72.5	5.4	10.3	-37.2	57.9	21239	30
225	11.6	16.7	-30.8	68.1	5.2	10.3	-36.5	59.5	21239	30
235	11.2	16.3	-32.6	69.6	5.0	10.2	-31.5	58.7	21239	30
245	10.9	15.8	-29.5	65.8	4.7	10.0	-31.1	59.7	21239	30
255	10.6	15.4	-32.0	67.5	4.5	9.8	-32.2	57.0	21239	30
265	10.3	15.1	-33.6	63.7	4.3	9.7	-30.5	59.5	21239	30
275	10.1	14.7	-33.9	69.0	4.1	9.6	-29.9	54.1	21239	30
285	9.8	14.3	-32.2	67.8	4.0	9.4	-27.2	55.6	21239	30
295	9.7	13.9	-30.9	67.4	3.8	9.3	-29.6	49.6	21239	30
305	9.3	13.7	-24.7	61.8	3.7	9.1	-29.2	48.4	21239	30
315	9.1	13.3	-25.6	60.7	3.6	9.0	-27.3	47.9	21239	30
325	8.9	13.0	-26.7	57.1	3.5	8.8	-27.7	49.0	21239	30
335	8.7	12.8	-28.1	52.0	3.4	8.8	-28.9	49.3	21239	30
345	8.5	12.5	-33.3	50.0	3.3	8.6	-33.6	46.2	21239	30
355	8.3	12.2	-31.7	51.7	3.3	8.5	-35.6	45.7	21239	30
365	8.1	12.0	-40.0	53.3	3.2	8.4	-36.5	46.6	21239	30
375	8.0	11.9	-39.7	50.4	3.1	8.4	-38.3	46.8	21239	30
385	7.8	11.7	-38.5	50.2	3.0	8.3	-33.1	45.7	21239	30
395	7.7	11.6	-33.3	50.5	3.0	8.2	-32.0	46.6	21239	30
405	7.5	11.3	-35.1	47.6	2.9	8.2	-31.6	46.0	21239	30
415	7.4	11.1	-28.6	50.2	2.8	8.0	-30.2	46.5	21239	30
425	7.2	10.9	-26.3	46.5	2.7	7.8	-27.3	45.2	21239	30
435	7.1	10.6	-27.5	52.4	2.7	7.6	-23.4	44.8	21239	30
445	6.9	10.4	-26.3	47.0	2.5	7.5	-21.4	42.1	21239	30
455	6.7	10.1	-22.4	47.2	2.4	7.4	-21.4	39.5	21239	30
465	6.6	9.8	-24.4	44.0	2.3	7.3	-23.2	40.4	21239	30
475	6.4	9.6	-21.6	40.8	2.3	7.2	-21.4	38.7	21239	30
485	6.2	9.4	-23.0	41.8	2.1	7.0	-21.3	37.1	21239	30
495	6.1	9.2	-22.4	43.8	2.0	6.9	-25.5	33.9	21239	30
505	5.8	8.9	-19.7	39.8	1.9	6.8	-21.6	33.2	21239	30

Table A-5 Basic Statistics for Mooring 5 (continued).

Depth	Mean u	Std u	Min u	Max u	Mean v	Std v	Min v	Max v	MMS# of Obs	Sample Interval
515	5.6	8.7	-22.7	39.2	1.8	6.6	-21.5	31.8	21239	30
525	5.3	8.3	-21.1	37.2	1.6	6.4	-20.8	30.5	21239	30
763	1.6	4.6	-25.8	21.0	0.6	4.5	-20.4	25.6	8613	60
755	2.7	6.5	-32.1	36.0	0.1	5.9	-27.7	31.5	21244	30
765	2.5	6.3	-31.0	27.1	0.0	5.8	-25.6	33.2	21244	30
775	2.5	6.2	-30.6	28.6	0.0	5.7	-26.7	33.6	21244	30
785	2.3	6.2	-29.7	28.0	-0.1	5.7	-26.4	32.8	21244	30
795	2.2	6.2	-27.0	30.8	0.0	5.8	-26.4	30.8	21244	30
805	2.1	6.2	-26.8	29.4	-0.1	5.8	-26.4	26.4	21244	30
815	2.1	6.2	-25.1	30.1	-0.1	5.8	-24.2	26.6	21244	30
825	2.1	6.1	-23.4	28.1	-0.1	5.8	-26.3	24.7	21244	30
835	2.0	6.0	-24.7	27.3	-0.2	5.7	-26.9	26.0	21244	30
845	1.9	6.0	-21.6	25.8	-0.3	5.7	-25.4	26.4	21244	30
855	1.9	5.9	-24.1	25.4	-0.2	5.6	-24.0	27.1	21244	30
865	1.8	5.8	-20.5	30.5	-0.2	5.5	-25.1	28.7	21244	30
875	1.7	5.7	-20.7	29.4	-0.3	5.5	-21.4	26.4	21244	30
885	1.7	5.6	-21.5	25.9	-0.4	5.4	-24.1	26.2	21244	30
895	1.5	5.5	-21.4	24.8	-0.5	5.3	-20.1	25.3	21244	30
905	1.5	5.4	-21.8	22.9	-0.5	5.3	-19.0	27.9	21244	30
915	1.4	5.3	-23.1	22.5	-0.6	5.2	-19.7	26.1	21244	30
925	1.3	5.3	-23.6	21.4	-0.6	5.1	-18.8	22.4	21244	30
935	1.2	5.2	-25.1	21.6	-0.7	5.1	-20.4	21.5	21244	30
945	1.1	5.0	-22.1	20.5	-0.7	5.0	-20.4	21.0	21244	30
955	1.0	4.9	-24.5	20.7	-0.8	4.9	-19.7	21.6	21244	30
965	0.9	4.8	-20.2	19.0	-0.9	4.9	-21.7	24.2	21244	30
975	0.8	4.8	-17.9	19.2	-0.9	4.9	-21.6	20.4	21244	30
985	0.7	4.7	-20.2	19.2	-1.0	4.8	-21.6	20.0	21244	30
995	0.7	4.6	-20.3	18.8	-1.0	4.8	-22.7	20.7	21244	30
1005	0.6	4.5	-18.2	16.2	-1.1	4.7	-22.2	17.8	21244	30
1015	0.5	4.5	-21.1	18.3	-1.1	4.7	-20.0	21.5	21244	30
1025	0.5	4.5	-25.3	18.7	-1.1	4.7	-23.6	17.3	21244	30
1035	0.4	4.4	-18.9	18.2	-1.2	4.7	-23.2	17.4	21244	30
1045	0.4	4.4	-18.8	18.5	-1.3	4.6	-24.2	17.3	21244	30
1055	0.4	4.3	-16.4	18.4	-1.2	4.6	-22.2	19.2	21244	30
1065	0.3	4.3	-16.7	16.0	-1.2	4.6	-22.6	20.8	21244	30
1075	0.3	4.2	-17.3	17.8	-1.2	4.6	-22.0	18.7	21244	30
1085	0.2	4.2	-17.6	19.6	-1.2	4.6	-21.2	20.7	21244	30
1095	0.2	4.3	-18.2	17.8	-1.3	4.6	-21.2	22.7	21244	30
1105	0.1	4.2	-18.3	16.8	-1.3	4.6	-19.3	23.8	21244	30
1115	0.1	4.2	-19.3	17.5	-1.3	4.5	-22.2	20.1	21244	30
1125	0.0	4.2	-17.0	16.8	-1.3	4.5	-19.9	22.6	21244	30
1135	0.0	4.2	-18.4	18.0	-1.3	4.4	-19.2	19.2	21244	30
1145	0.0	4.2	-17.8	15.9	-1.3	4.4	-20.5	18.9	21244	30
1155	-0.1	4.2	-16.7	16.3	-1.3	4.4	-19.6	19.5	21244	30
1165	-0.1	4.2	-18.1	16.8	-1.4	4.4	-19.5	17.7	21244	30
1175	-0.1	4.2	-19.7	18.9	-1.4	4.3	-19.2	17.7	21244	30
1185	-0.1	4.1	-18.9	20.1	-1.4	4.2	-22.2	20.2	21244	30

Table A-5 Basic Statistics for Mooring 5 (continued).

Depth	Mean u	Std u	Min u	Max u	Mean v	Std v	Min v	Max v	MMS# of Obs	Sample Interval
1195	0.0	4.0	-21.0	17.2	-1.4	4.2	-19.8	16.7	21244	30
1205	-0.1	3.9	-20.9	16.6	-1.4	4.1	-19.8	16.3	21244	30
1215	-0.3	3.8	-22.2	15.3	-1.3	3.9	-21.7	15.3	21244	30
1572	-0.4	2.6	-11.4	13.9	-1.5	2.8	-12.5	12.2	10622	60
1998	-0.3	1.8	-9.0	11.2	-2.5	3.1	-18.5	10.6	21244	30
2006	-0.3	1.7	-9.2	12.1	-2.6	3.1	-18.5	10.0	21244	30
2014	-0.2	1.7	-8.9	11.6	-2.6	3.1	-18.5	9.5	21244	30
2022	-0.2	1.6	-8.3	11.7	-2.6	3.1	-18.2	9.0	21244	30
2030	-0.1	1.6	-7.7	11.8	-2.5	3.0	-17.5	8.1	21244	30
2038	0.0	1.5	-7.7	10.3	-2.4	2.9	-17.7	8.1	21244	30
2046	-0.4	1.5	-7.6	10.7	-1.4	2.8	-16.5	7.8	21244	30